

**3D full-wave modelling of microwave  
interactions with plasma density  
fluctuations**

Matthew Bryn Thomas

Doctor of Philosophy

University of York

Physics

November 2017

---

*“If we knew what it was we were doing, it would not be called research, would it?”*

Albert Einstein

*“Those who educate children well are more to be honoured than they who produce them; for these only gave them life, those the art of living well.”*

Aristotle

*“The measure of intelligence is the ability to change one’s mind.”*

Stephen Hawking

*“The greatest deception people suffer is from their own opinions.”*

Leonardo da Vinci

# Abstract

The scattering of microwaves by density fluctuations in magnetised plasmas where the inhomogeneity scale length is comparable to the wavelength is not fully understood. Yet microwaves are used extensively in magnetically confined fusion plasmas not only to provide a wealth of information through diagnostics but for heating and current drive. To this end a 3D full-wave finite difference time domain code (EMIT-3D) has been designed to model the quasi-3D Doppler reflectometry data from a novel synthetic aperture microwave imaging diagnostic (SAMI) and to understand the scattering effects of turbulence on heating and current drive beams. SAMI captures a 2D view of the plasma in a  $\pm 40^\circ$  illumination from the mid-plane. A vast spatial grid is required to capture the inhomogeneous, curved plasma and magnetic geometry whilst considerable acquisition time is required for Doppler resolution. For this reason EMIT-3D has been parallelised in 3D which is shown to scale well to large machines. EMIT-3D is shown to agree with the extensive benchmarking tests and demonstrates stability to large time iterations. EMIT-3D has been applied to electron cyclotron resonance heating (ECRH) deposition broadening in the DIII-D tokamak. Significant ECRH deposition broadening was measured in three different operating scenarios: L-mode, H-mode and negative triangularity. Each scenario corresponds to distinct turbulence characteristics in the edge region through which the beam must propagate. The turbulence is generated through the Hermes model in the BOUT++ framework which takes as input the measured time averaged electron density, temperature and magnetic field profiles for the specific shot in question. The simulated turbulence is constrained to match the experimentally measured correlation length and normalised fluctuation levels. The predictions of the beam broadening from the simulations are found to agree very well with the experimentally-observed broadening in all cases.



# Contents

<b>Abstract</b>	<b>iii</b>
<b>List of Tables</b>	<b>ix</b>
<b>List of Figures</b>	<b>xi</b>
<b>Acknowledgements</b>	<b>xv</b>
<b>Declaration</b>	<b>xvii</b>
<b>1 Background and motivation</b>	<b>1</b>
1.1 Motivation of fusion research . . . . .	1
1.2 A brief review of fusion research . . . . .	4
1.3 Turbulence and stability . . . . .	8
1.4 EM waves in fusion plasmas . . . . .	10
1.5 The SAMI diagnostic . . . . .	12
1.5.1 Capabilities and motivation for this thesis . . . . .	13
<b>2 Formalism of the wave mechanics</b>	<b>17</b>
2.1 Theoretical formalism . . . . .	17
2.1.1 Wave definitions and plasma parameters . . . . .	17
2.1.2 Derivation of dispersion relation . . . . .	19
2.1.3 Analysis of dispersion relation . . . . .	23
2.1.4 Mode conversion . . . . .	29
2.1.5 Magnetised 2D plasma slab . . . . .	31
2.2 Computational formalism . . . . .	33

2.2.1	Numerical methods . . . . .	33
2.2.2	FDTD for EMIT-3D . . . . .	36
<b>3</b>	<b>EMIT-3D</b>	<b>45</b>
3.1	Code development . . . . .	45
3.1.1	3D Parallelisation . . . . .	45
3.1.2	Boundary conditions . . . . .	47
3.1.3	Antenna array . . . . .	49
3.1.4	NetCDF I/O and 3D visualisation routine . . . . .	51
3.1.5	Benchmarking - dispersion relation . . . . .	52
3.1.6	Scalability . . . . .	53
3.2	Development for reflectometry and SAMI modelling . . . . .	54
3.2.1	Density profile functions . . . . .	54
3.2.2	Interpolation for moving density . . . . .	56
3.2.3	Benchmarking - reflectometry . . . . .	57
3.2.4	Broad beam Doppler reflectometry in turbulence slab . . . . .	64
3.2.5	Modelling the SAMI diagnostic on MAST-U and NSTX-U in 3D curved tokamak geometries . . . . .	69
<b>4</b>	<b>Scattering parameter scan</b>	<b>77</b>
4.1	Motivation . . . . .	77
4.2	Turbulence model . . . . .	78
4.3	The simulation set-up . . . . .	79
4.4	Interpreting the data . . . . .	82
4.5	Results . . . . .	86
4.5.1	Variation of the correlation length . . . . .	86
4.5.2	Variation of the RMS fluctuation level . . . . .	89
4.5.3	Variation of the turbulence layer thickness . . . . .	90
4.5.4	Variation of the injected beam waist . . . . .	91
4.5.5	Variation of the background density . . . . .	93
4.5.6	Oblique propagation to the filamentary structures . . . . .	93

4.5.7	Considerations for the experimentalist . . . . .	94
4.6	Summary . . . . .	96
<b>5</b>	<b>ECRH Beam broadening on DIII-D</b>	<b>97</b>
5.1	Motivation . . . . .	98
5.2	Experimental Measurements . . . . .	99
5.3	Theory Modelling . . . . .	101
5.3.1	The simulation domain and beam initialisation . . . . .	101
5.3.2	Generation of the turbulence . . . . .	102
5.3.3	Using experimental diagnostics to constrain the simulated tur- bulence characteristics . . . . .	103
5.4	Results . . . . .	106
5.4.1	The ensemble . . . . .	106
5.4.2	Projection to the absorption surface . . . . .	108
5.4.3	Beam broadening in each scenario . . . . .	109
5.4.4	Sensitivity of the modelled broadening to resolution of diagnostics	112
5.5	Discussion . . . . .	114
<b>6</b>	<b>Plasma thrusters</b>	<b>117</b>
6.1	Introduction . . . . .	117
6.2	Experimental set-up . . . . .	120
6.2.1	Probe design . . . . .	123
6.3	Results . . . . .	124
6.3.1	Argon . . . . .	125
6.3.2	Ar-SF <sub>6</sub> . . . . .	126
6.4	Conclusions . . . . .	132
<b>7</b>	<b>Conclusions and future work</b>	<b>135</b>
7.1	Summary . . . . .	135
7.2	Conclusions . . . . .	137
7.3	Future work . . . . .	139

---

7.3.1	Project 1: Prediction of ECCD beam broadening and cross polarisation scattering in ITER . . . . .	139
7.3.2	Project 2: 3D Doppler reflectometry simulations for SAMI . . .	140
7.3.3	Project 3: Inclusion of an option to turn on background current density and magnetic shear . . . . .	140
<b>Appendix 1 - Derivation of current density evolution equation with the inclusion of magnetic shear</b>		<b>143</b>
<b>Bibliography</b>		<b>147</b>

# List of Tables

1.1	Deaths per petawatt hour (PW <sub>hr</sub> ) due to different fuel sources . . . . .	3
2.1	Trial plasma fixed parameters . . . . .	31
3.1	Double corrugation back scatter angles . . . . .	66
5.1	Experimental measurements of edge fluctuation level and beam broadening	101
5.2	Beam broadening results for all three scenarios: comparison with exper- iment . . . . .	111
5.3	Variation in beam broadening with diagnostic uncertainty . . . . .	113



# List of Figures

1.1	Population of the world and energy forecast . . . . .	2
1.2	Conventional and spherical tokamak designs . . . . .	6
1.3	A cartoon illustration of the SAMI diagnostic. . . . .	15
2.1	Illustration of wave vector and background magnetic field . . . . .	28
2.2	Wave velocity behaviour at cut-off and resonance . . . . .	29
2.3	Analytic dispersion relation . . . . .	32
2.4	Characteristic frequencies vs plasma density . . . . .	33
2.5	Yee cell . . . . .	36
3.1	Ghost cell method for 3D parallelisation . . . . .	47
3.2	Damper field functional form and contour plot . . . . .	48
3.3	3D output of O-mode wave in homogeneous background . . . . .	50
3.4	Benchmarking - dispersion relation . . . . .	53
3.5	Scaling of EMIT-3D on the Marconi super computer . . . . .	54
3.6	Analytic density function . . . . .	55
3.7	Corrugated density profiles in EMIT-3D . . . . .	61
3.8	Bragg benchmarking 3D visualisation . . . . .	61
3.9	Bragg benchmarking results . . . . .	62
3.10	Benchmarking of Bragg reflection from a turbulence slab . . . . .	64
3.11	Broad beam Doppler reflectometry in turbulence slab . . . . .	65
3.12	Double corrugation density profile . . . . .	67
3.13	Bragg reflection from two corrugated surfaces . . . . .	68
3.14	Output of turbulence Doppler shifted power across the antenna . . . . .	69

3.15	View of SAMI on MAST . . . . .	70
3.16	Paralleisation in a cone domain for SAMI . . . . .	73
3.17	Damping profile in the SAMI cone shape domain . . . . .	75
4.1	Turbulence profile generated in BOUT++ . . . . .	80
4.2	Hasegawa-Wakatani turbulence within EMIT-3D simulation domain . . . . .	81
4.3	Receiving antenna RMS electric field . . . . .	82
4.4	Ensemble statistical relevance . . . . .	83
4.5	Scatter parameter log-normal distribution . . . . .	85
4.6	Images of the parameter scan in correlation length . . . . .	86
4.7	Scattering vs correlation length . . . . .	87
4.8	Scattering as a function of correlation length . . . . .	88
4.9	Images of the parameter scan in fluctuation level . . . . .	89
4.10	Scattering as a function of the RMS fluctuation level . . . . .	90
4.11	Scattering as a function of layer thickness . . . . .	91
4.12	Scattering as a function of beam waist . . . . .	92
4.13	Scattering of microwave at oblique angle to filaments . . . . .	94
5.1	Experimental set up in DIII-D . . . . .	100
5.2	3D visualisation of scattering through the edge in DIII-D . . . . .	102
5.3	Plasma edge characteristic analysis . . . . .	105
5.4	Scattering convergence with ensemble size . . . . .	107
5.5	Reference beam vs ensemble beam . . . . .	108
5.6	Beam broadening results for all three scenarios . . . . .	109
5.7	Diagnostic uncertainty parameter scan . . . . .	113
6.1	PEGASES thruster particle drifts diagram . . . . .	121
6.2	PEGASES probe array diagram . . . . .	123
6.3	PEGASES langmuir probe diagram . . . . .	123
6.4	PEGASES probe magnetic field map . . . . .	124
6.5	Argon floating potential variation . . . . .	125
6.6	ArSF6 floating potential variation . . . . .	126

---

6.7	I-V plots from individual probes . . . . .	127
6.8	ArSF6 electron flux . . . . .	129
6.9	ArSF6 electron flux reversed polarity . . . . .	129
6.10	ArSF6 electron drift vs pressure . . . . .	130



# Acknowledgements

Firstly I would like to thank Roddy Vann for giving me the opportunity to be involved in the area of research in which I am so fascinated, and for fuelling my enthusiasm further with his great dedication to my studies and his knowledge and passion for the subject matter. I would like to thank Jarrod Leddy and Alf Köhn for vastly speeding up the learning process, particularly at the beginning of my Ph.D..

I would like to thank my parents Christine and Bryn who always fought for me and supported me heavily during the troublesome school years, for providing an amazing home environment to grow up in and without whom I could not have even come close to beginning a Ph.D.. I would also like to thank Rebecca Marshall, the provider of copious amounts of M&M's, for her love, kindness and for putting up with me over these years at York. Lastly to my brother Ryan for countless comical escapades.

The author acknowledges access to the EUROfusion High Performance Computer (Marconi-Fusion) through EUROfusion. The author also acknowledges access to the HELIOS supercomputer system at Computational Simulation Centre of International Fusion Energy Research Centre (IFERC-CSC), Aomori, Japan, under the Broader Approach collaboration between Euratom and Japan, implemented by Fusion for Energy and JAEA. This research was funded by the EPSRC Centre for Doctoral Training in Science and Technology of Fusion Energy grant EP/L01663X.



# Declaration

I declare that the work presented in this thesis, except where it is otherwise stated, is based on my own research and has not been submitted previously for a degree in this or any other university. All sources are acknowledged as References. Parts of the work presented in this thesis have been published in:

**I.** “*Influence of plasma turbulence on microwave propagation*”:

A. Köhn, E. Holzhauer, J. Leddy, M.B. Thomas and R.G.L. Vann: *Plasma Phys. Control. Fusion* **58** 105008 (2016)

**II.** “*Experimental investigation of electron transport across a magnetic field barrier in electropositive and electronegative plasmas*”:

M.B. Thomas, D. Rafalskyi, T. Lafleur and A. Aanesland: *Plasma Sources Sci. Technol.* **25** 045018 (2016)

**III.** “*Perturbing microwave beams by plasma density fluctuations*”:

A. Köhn, E. Holzhauer, J. Leddy, M.B. Thomas and R.G.L. Vann: *EPJ web of Conferences* **147** 01001 (2017)

**IV.** “*Broadening of microwave heating beams in the DIII-D tokamak by edge turbulence*”:

M.B. Thomas, M.W. Brookman, M.E. Austin, K. Barada, M. Cenghar, R.J. La Haye, J.B. Leddy, T.C. Luce, C.C. Petty, T. Rhodes, Z. Yan, A. Köhn and R.G.L. Vann: Submitted to *Phys. Rev. Lett.* Mar 2018.

**V.** “*Resolving ECRH deposition broadening due to edge turbulence in DIII-D by the heat flux measurements*”:

M.W. Brookman, M.B. Thomas, M.E. Austin, K. Barada, M. Cenghar, R.J. La

Haye, J.B. Leddy, T.C. Luce, C.C. Petty, T. Rhodes and R.G.L. Vann: Submitted to *Nucl. Fusion* Apr 2018.

Uploaded to ArXiv: 1710.03503 10/10/2017

**VI.** “*Resolving ECRH deposition broadening due to edge turbulence in DIII-D by 3D full-wave simulations*”:

M.B. Thomas, M.W. Brookman, M.E. Austin, A. Köhn, R.J. La Haye, J.B. Leddy, R.G.L Vann and Z. Yan: Submitted to *Nucl. Fusion* Apr 2018.

Uploaded to ArXiv: 1710.03028 09/10/2017

# Chapter 1

## Background and motivation

### 1.1 Motivation of fusion research

There are three main reasons why the philosophical mind would hold a keen interest in developing a high energy density, clean, sustainable source of electricity. These are political, economical or most ideally ethical. Firstly, in a politician's mind, the ideal energy policy for their country is one which does not rely on any other country to provide energy to their own population. In this case the only option is to utilise a sustainable source of energy which has sufficiently high energy density that their own territory can provide the power demand of the population.

Secondly, from an economic viewpoint, huge growth in industrial investment for clean, sustainable energy sources is occurring across the globe. At the time of writing fossil fuels provide  $\sim 50\%$  of the European energy supply [1] and  $\sim 80\%$  of the world energy supply [2]. The percentage of the world energy supplied by fossil fuels has not notably decreased since 1973, driven by the huge increase in fossil fuel use by China and India, though in Europe it has decreased by  $\sim 30\%$ . Furthermore, China has recently outlined a plan to cut fossil fuel use to  $< 50\%$  by 2050. Though it is difficult to assign one particular motive for this global change in direction, it is an unavoidable fact that the fossil fuel reserves are finite. One particular study has shown reserves of 40, 70 and 200 years for oil, gas and coal respectively [3] which are upper estimates compared with other reserve calculations. Nonetheless, the key factor is not the total reserves but the production rates of the fuel. Previous studies have shown that in the

best case scenario, fossil fuel production will continue the current rate of growth until 2025 before stagnating for 50 years and declining thereafter. The middle and worst case scenarios are much sooner [4, 5]. It is clear that the current evidence points towards a global increase in the percentage of the market provided by clean, sustainable energy. Combine this with the increase in energy demand year on year (see figure 1.1) and the result is an ever increasing portion of the energy market value of  $> \text{€}5$  trillion which will be claimed by clean, sustainable fuels.

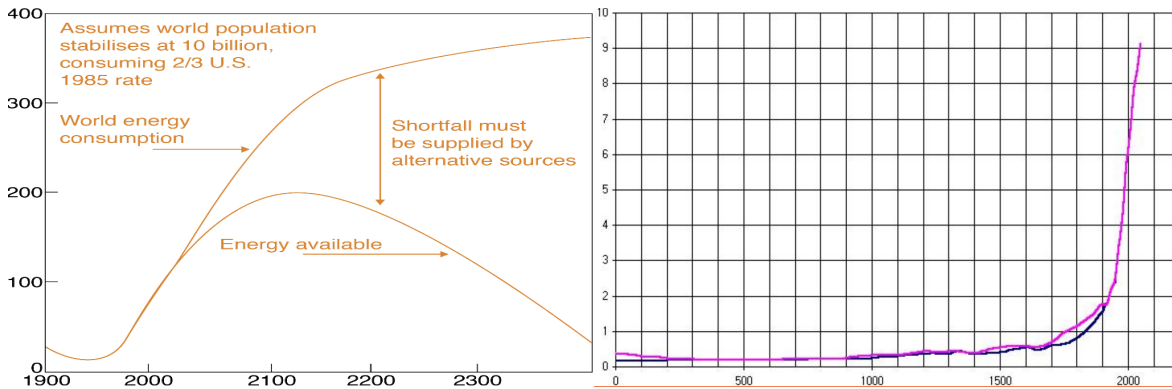


**Figure 1.1:** Left: The world energy demand in billion Barrels of Oil Equivalent (BOE) projected in to the future assuming a population stabilisation of 10 billion people (source: Graph taken from The World Energy Council). The energy available decline curve is based on the production projection of fossil fuels and not considering any further increase in clean, sustainable energy. Right: The population of the world plotted with a lower estimate (blue) and upper estimate (pink) through time. Figure taken from U.S Census Bureau.

Thirdly, from an ethical point of view there are three considerations. Based on humanity’s historical record for conflict over resources, the depletion of the overwhelmingly dominant source of energy to zero can only result in significant conflict over the remaining fossil fuels, unless substantial advancement in international cooperation is reached. Even with the most sceptical thought towards dwindling resource estimates, the booming population causing rapidly increasing energy demand combined with the desire of human beings to maintain high energy lavish lifestyles, would ensure conflict is inevitable. The only discussion is the time line over which it would happen, which unfortunately is the largest barrier to change if the public or their politicians cannot envisage the catastrophe affecting them within their lifetime. More immediately however, fossil fuel burning is currently directly responsible for between 4 to 7 million premature deaths per year depending on the study conducted [6, 7]. However, as these are so called “silent” deaths with no single physical object with which to see and lay

blame it is difficult to convince the public to be concerned about them. On the other hand the 38 deaths attributed directly to Chernobyl and the 34 deaths to Fukushima (0 from radiation exposure and 34 from evacuation procedure) needed no convincing to be seen as “unacceptable nuclear disasters”. The fact that statistically these nuclear power stations would have contributed to extending the lives of tens of thousands of people by not burning fossil fuels seems to be irrelevant in public opinion (see table 1.1).

	Coal (average)	Oil	Gas	Biofuel/ Biomass	Solar (roof)	Wind	Nuclear Fission
Deaths/PWhr	100 000	36 000	4 000	24 000	440	150	0.1

**Table 1.1:** Approximate deaths per petawatt hour (PWhr) due to different fuel sources. Source: World Health Organisation. For reference, in 2015 the world consumption of coal, oil and gas was approximately 45, 50 and 35 PWhr resulting in the WHO estimate of  $4.5 + 1.8 + 0.14 = 6.44$  million. This number increases to 7 million when considering the extra use of coal in China resulting in a local value of 170 000/PWhr.

However, the most important ethical consideration transcends the effects limited to human society. Global warming is one of the biggest threats to the survival of our species that must be addressed this century. Yet, it is the threat of extinction for countless other species that share this world that must be considered. The Intergovernmental Panel on Climate Change (IPCC) concludes that global warming is a direct result of human beings burning fossil fuels. This stance arises from a consensus reached by 97-98% of the actively publishing scientists in experimental and theoretical research. A recent review attempted to replicate the results of a large portion of the 3% that do not agree with the consensus, which revealed a pattern of common mistakes and methodological flaws in the data analysis, which had led to the incorrect conclusions [8]. The current goal for limiting the effect of climate change is to ensure global average temperatures do not rise by more than  $1.5^{\circ}\text{C}$  above pre-industrial levels [9]. This goal is deliberately below the more catastrophic effects predicted by reaching  $2^{\circ}\text{C}$ . Continued rise in average global temperatures by more than  $2^{\circ}\text{C}$  would ensure that an increasing majority of coral reef species are completely wiped out before 2100, which could cause an ecological crash across the oceans [10, 11]. One quarter of the annual total fish

catch in Asia is sustained by coral reefs which feed over a billion people [12]. Moreover, for a large range of major world crops such as corn, wheat, soy and maize, the increase above  $2^{\circ}\text{C}$  would push local temperature fluctuations above the thermal limit of the crop, preventing the crop from producing seed and significantly reducing the crop yield [13]. The projected sea level rise (median case) is  $\sim 1$  metre by 2100 [14], putting coastal cities at risk, whilst the available fresh water in the Mediterranean would drop by almost 20%. Most of these effects would result in hundreds of millions of climate refugees. These effects are magnified dramatically for small increases in warming above  $2^{\circ}\text{C}$  degrees. Currently the average temperature increase is  $+1^{\circ}\text{C}$  [15].

## 1.2 A brief review: From the beginnings to the state of the art of fusion research

From a very early date the magnitude of energy density contained within fusion reactions was known to the scientific community. Following the discovery of quantum tunnelling at the turn of the 20th century, calculations of fusion reactions began to take place which pointed towards fusion as the mechanism for the creation of energy in the core of stars [16]. Following this work, fusion reactions of light nuclei in the lab led to the discovery of tritium and helium-3 in the 1930's [17]. The energy density of these reactions became apparent immediately, calculated as producing ten times more energy per kilogram than fission reactions and 10 million times more than fossil fuels. Furthermore, it was clear that a fuel source of hydrogen isotopes had the potential to provide a near limitless source of energy. Though not the original motivation, it is worth noting that currently a large advantage of fusion energy is that the reaction does not produce any pollutants and does not create any radioactive daughter particles. However, deuterium-tritium fusion reactors would produce a small amount of short lived ( $\approx 100$  years) radioactive waste through secondary collisions by neutrons in the wall of the reactor.

To produce a fusion reaction one must provide two nuclei with enough kinetic energy to overcome their electrostatic repulsion. At these energies the reactants will be

completely ionised. This state of matter is known as a plasma. The most useful reaction is one that has the largest reaction rate for the lowest input heating power. By plotting the reaction rate *vs* temperature for a number of reactions one finds the deuterium ( $^2\text{H}$ ) - tritium ( $^3\text{H}$ ) reaction is the most promising. Even though this reaction requires the lowest input power, achieving peak reaction rate still requires temperatures in the core which exceed 10 keV (116 million $^\circ\text{C}$ ). One must therefore confine this plasma without it touching any materials. Two experimental methods exist for confining a fusion plasma, Inertial Confinement Fusion (ICF) and Magnetic Confinement Fusion (MCF). This thesis focusses exclusively on MCF devices and so ICF will not be discussed. To achieve net power output, the fusion reaction must generate more power than is used for both confining and heating the plasma. The D-T reaction produces a high energy neutron which is not confined and also a lower energy  $\alpha$ -particle which may be confined. By requiring that fusion reactions occur at a sufficient rate, such that the energy from the  $\alpha$ -particles that remain in the plasma replace the energy lost from particle and radiative losses, one assures that the reaction is self sustaining. The criterion for this balance is defined by the Lawson criterion (1.1). Here  $n$  is the particle density,  $T$  is the temperature and  $\tau$  is the energy confinement time. Though this is a rough estimate, this criterion is often used to define the ignition point where the external heating can be switched off and the fusion plasma is self sustaining.

$$nT\tau > 3 \times 10^{21} \text{ m}^{-3}\text{keVs} \quad (1.1)$$

In the 1950's pioneering research had already moved from a basic magnetic mirror concept to a continuous toroidal field thus removing the end losses of the magnetic mirror. However, the design suffered from instabilities and poor confinement due to classical guiding centre drifts of the particle orbits. The gradient and curvature of the magnetic field caused electrons and ions to drift in opposite directions to the top and bottom of the tokamak. This gave rise to a vertical electric field which caused both sets of particles to experience an  $\mathbf{E} \times \mathbf{B}$  drift radially outwards. The unique solution was to drive a current in the plasma which in turn results in a poloidal magnetic field which

effectively short circuits the electric field by connecting the top and the bottom of the plasma. The basic concept has remained largely unchanged to date and has resulted in two unique MCF tokamak designs, the conventional tokamak and spherical tokamak. A separate route to magnetically confined fusion is the stellarator which works in a different way to the tokamak. Though almost all of the physics discussed in this thesis can be applied to the stellarator it has not been directly addressed and shall not be discussed further.

**Conventional tokamak:** The conventional design confines the plasma through a series of D shaped magnetic field coils which stack together forming a torus shape (the design can be seen in figure 1.2). These coils provide a magnetic field toroidally which keeps the plasma confined. As discussed above the breakthrough in design came from applying a current in the plasma which creates a poloidal magnetic field resulting in a twisted magnetic field configuration. This plasma current is initially provided and maintained by the central solenoid. The central solenoid also provides the ohmic heating to start the plasma in the same way that a current heats up a filament in a light bulb.

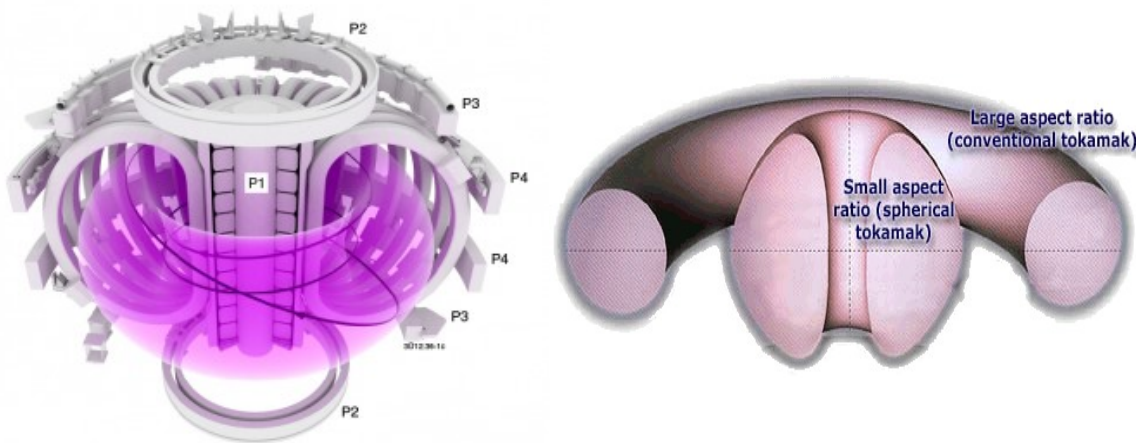


**Figure 1.2:** Left: The conventional aspect ratio tokamak with a plasma illustrated in the middle. The purple line represents one field line which moves helically due to the poloidal contribution to the magnetic field. The poloidal field coils (not to be confused with the poloidal field provided by the plasma current) are labelled P2-P4. P1 is the central solenoid which provides the plasma current to give the helical field. The D coils provide the toroidal field and are stacked toroidally. Image taken from Euro-fusion. Right: The difference in plasma shape for a spherical tokamak and a conventional tokamak. Image taken from UKAEA.

It was identified that plasma stability can be increased by moving from a circular cross section to a D shaped plasma where the high shear helps to break up the turbulent

eddies. This shaping is provided by external poloidal field coils that sit in rings from the top to the bottom around the outside of the tokamak. These poloidal field coils are for shaping and positioning and not to be confused with the poloidal field that is generated from the plasma current which provides the helical field. The latest major design modification was the divertor concept which allows the removal of spent fuel and impurities to be flushed out at the top and the bottom on open field lines.

**Spherical tokamak (ST):** This design works in the same way as the conventional tokamak and maintains the same D shaped plasma except the magnets hold the plasma in a much tighter configuration. The tighter configuration is achieved by combining the components of the toroidal field coils on the inboard side in to one conducting column instead of passing individual D coils [18] and by removing much of the shielding. With the magnets so much closer to the plasma, ST's require significantly less energy to produce the same confining magnetic field within the plasma. This means that the efficiency of the confining fields ( $\beta = \text{Plasma Pressure/Magnetic Pressure}$ ) is much higher, measured as up to 12% for conventional tokamaks and up to 40% for STs. At a tighter aspect ratio, the plasma is able to access a higher plasma beta before magnetohydrodynamic instabilities such as the kink and higher order ballooning modes cause the plasma to become unstable. Furthermore, the magnetic field configuration in an ST means that a particle spends much more time on the inboard side than the outboard side unlike in a conventional tokamak. The plasma on the inboard side is inherently more stable than the outboard side because the pressure gradient vector and the curvature vector point in the opposite direction, whereas on the outboard side they point in the same direction. The latter is known as bad curvature and the former is known as good curvature, where the good curvature results in a stabilising effect of the local  $\mathbf{E} \times \mathbf{B}$  drift on turbulence seeding. This increased time spent by particles on the inboard side increases the ST's plasma stability even further.

The ST has two major disadvantages thought to prevent its use as a reactor, though recent promising breakthroughs may mean these are soon overcome. Due to the reduced space in the central column of the ST the magnetic field is limited compared with conventional tokamaks. This cannot be improved by using superconducting

magnets because there is only a limited amount of space for shielding and so they cannot reach the low temperatures required to operate. There is therefore a limit on the toroidal magnetic field  $B_t$  achievable. Recently however, significant progress has been made in high temperature superconducting magnet design which could provide very large fields in the space required at temperatures achievable with the available shielding. The fusion power yield scales as  $P_{\text{fus}} \sim \text{Volume} \times \beta^2 B_t^4$  which means that a high magnetic field combined with the already high beta of a spherical tokamak would be highly desirable as a reactor. Another major disadvantage is the central solenoid as not only does it take up space but the high energy fusion neutrons would degrade the insulator very quickly in a reactor. However, recently alternative start up methods such as the use of electron Bernstein waves or through merging compression have shown great success. Moreover, the plasma current may be maintained through injection of microwave beams. Success in these two areas would remove the need for a central solenoid and would provide space for shielding of the toroidal field coils and for a blanket layer with which to breed tritium. Microwave systems combined with computational modelling will be pivotal in this endeavour.

### 1.3 Turbulence and stability

Early on in fusion development it was widely assumed that confinement of energy and particles was limited only by collisions which cause particles to diffuse out of the confining magnetic field. In this scenario, net energy gain would be achieved quickly and the notion that fusion power would be 30 years away was born. Unfortunately, it was later discovered that particle transport was thousands of times greater than predicted which is arguably the main reason that fusion power is not currently providing the national grid with electricity. This “anomalous transport” was discovered to arise from different forms of gyroradius scale micro-instabilities. Collectively these micro-instabilities are more generally described as turbulence.

A typical tokamak confines a plasma with a density of  $\sim 10^{20} \text{ m}^{-3}$  and temperatures of the order of 100 million kelvin, suspended in a vacuum chamber next to a solid wall which must have temperatures less than a few thousand kelvin. The temper-

ature gradients at this edge region are therefore amongst the largest in the universe. It is this temperature gradient which is a common driving force for many turbulence modes. Such modes include the electron temperature gradient (ETG), ion temperature gradient (ITG) and drift waves.

**ETG and ITG:** ETG and ITG modes are driven by the same mechanism, though the ETG has smaller spatial scales and larger linear growth rates than ITG due to the much smaller mass of the species [19, 20]. These modes are driven by a gradient in both temperature and magnetic field which in a tokamak plasma both point radially inwards towards the core from the edge. The radial magnetic field gradient which is perpendicular to the mostly toroidal magnetic field vector, results in a binormal particle drift. The binormal direction is that perpendicular to the magnetic field lines, but in the flux surface. If one assumes there is a small temperature perturbation radially then the hotter particles will drift faster than the cooler particles resulting in temperature and density perturbations both binormally and radially. These perturbations in turn give rise to local  $\mathbf{E} \times \mathbf{B}$  drifts which amplify the initial perturbation causing the mode to grow.

**Electron drift waves:** This mode is driven by the orthogonal magnetic field vector and radial density gradient. If one assumes a small density perturbation perpendicular to the density gradient and magnetic field vector, then periodic differences in electrostatic potential arise next to each other. The electrons respond first due to their small inertia by streaming along the magnetic field line until the induced electric field is balanced. This periodic potential gives rise to an electric field that alternates from positive to negative. The resulting  $\mathbf{E} \times \mathbf{B}$  drift is then  $\pi/2$  radians out of phase with the density perturbation. If this phase difference remains then the drift wave is stable and simply propagates. However if resistivity is included through collisions or Landau damping such that there is a delay on the electrons in compensating the periodic electric potential, then there is a phase lag which causes the drift wave to become unstable. The unstable drift wave forms rotating turbulent eddies which allow significant particle and energy transport by connecting with eddies across closed magnetic

field lines further out.

**Neoclassical Tearing Modes (NTM):** One particular large scale instability which can drastically affect confinement or worse the stability of the entire plasma is the formation of a neoclassical tearing mode. These magneto-hydrodynamic (MHD) instabilities are magnetic islands that develop on rational  $q$  surfaces with a flattened pressure gradient across the NTM, resulting in radially increased particle and energy transport [21].  $q$  is the ratio of toroidal to poloidal magnetic field line turns known as the safety factor. NTM's are seeded by small perturbations in the plasma bootstrap current which lead to small pockets of embedded closed flux surfaces known as magnetic islands. At small sizes an island is suppressed, however in the presence of other large scale MHD instabilities an island above a critical size may form which is driven unstable [22]. As the island grows it generates eddy currents in the wall of the vessel causing the plasma rotation to slow and eventually lock, resulting in a disruption where the stored energy of the plasma is dumped to the vessel wall [23, 24]. This instability is therefore dangerous in particular for the next generation of tokamaks such as ITER due to the large increase in stored energy of the plasma as compared with current devices.

## 1.4 Electromagnetic waves in fusion plasmas

The realisation of a thermonuclear fusion reactor has alluded the scientific community for decades. As discussed in the previous section, sufficient confinement and stability for a burning plasma is difficult to achieve in the presence of turbulence and micro-instabilities. One of the main challenges is understanding and predicting the nature of the turbulent plasma edge, its evolution through various operating scenarios and the implications to overall performance. Diagnostics that can probe the plasma and magnetic field properties in the edge with high spacial and temporal resolution are therefore fundamental in this endeavour.

Microwave diagnostics naturally have good spatial and temporal resolution ( $< 5$  mm,  $< 20 \mu\text{s}$ ) [25] and can probe the plasma passively, by receiving the spectrum of microwave radiation from the plasma or actively by launching milliwatt power to

ensure the plasma is not perturbed. Furthermore, as space close to the plasma is both valuable and hostile, waveguides can be used to direct the signal to a remote location. This results in better quality signal analysis and a system that can be scaled to reactor relevant devices that would require more space for tritium breeding and radiation shielding and would be too hostile for many other diagnostics.

Passive probing utilises the frequency of radiation emitted by the plasma at the electron cyclotron range and harmonics thereof. The electron cyclotron frequency changes depending on the distance into the plasma due to the inhomogeneity of the confining magnetic field. It is therefore possible to observe different regions in the plasma. Depending on whether the plasma is over or under dense the mechanism for the radiation to escape the plasma is different. In an over dense plasma the cyclotron frequency is below the plasma frequency at the location of emission and it must convert through different polarisation modes before reaching the diagnostic. In an under dense plasma the emitted photon is free to exit the plasma without mode conversion. Knowledge of the type of plasma is key to understanding the received data in these instances.

Active probing generally takes the form of reflectometry as the radiation sent to the plasma must be received back for comparison and analysis. Microwave reflectometry launches O-mode or X-mode beam polarisations which then reflect back from the plasma at the location of their respective cut off layers whilst stepping in frequency allows one to probe deeper into the plasma. The technique can generally be split between density profile measurements and density fluctuation measurements. The former has been successful in measuring the density profile in Tore Supra [25], DIII-D [26] and more recently EAST [27] and ASDEX-U (AUG) [28, 29]. Meanwhile the latter has been demonstrated on KSTAR [30], EAST [27] and AUG [29]. Further techniques to obtain these measurements such as microwave imaging reflectometry [31] and correlation reflectometry [32] have also been demonstrated. Another diversification in the reflectometry technique is Doppler reflectometry, where the beam is now aligned to have a component parallel to the plasma rotation vector at the reflection point. In this way more information can be extracted from the plasma. Extensive discussions of the

evolution and use of microwave reflectometry can be found in [33,34] and for Doppler reflectometry in [35].

Microwave systems are currently employed at much larger power to provide heating (either globally through large antennas or locally through collimated beams), current drive and as a method for start up. Non-inductive start up through the use of microwaves has been demonstrated experimentally in QUEST [36], NSTX [37], TST-2 [38] and through the use of Bernstein waves on MAST [39]. This method is important in spherical tokamaks where the spatial configuration does not allow for sufficient shielding of the central solenoid from neutrons in a burning plasma. The microwaves are used for pre-ionisation plasma heating, following which a plasma current is generated through the preferential acceleration and confinement of electrons, created by the open magnetic field line configuration during start-up [40].

Current drive is achieved in tokamaks usually in the electron cyclotron range (ECCD) [41]. However, less commonly lower hybrid waves are used to drive current at much lower frequencies [42,43]. Current drive would be crucial in starting and maintaining plasma current in a spherical tokamak without a central solenoid as discussed in section 1.2. Moreover, localised current drive is necessary for stabilising the NTM's discussed in section 1.3. The stabilising beam is only effective within the O-point of the NTM requiring collimated beams with accurate targeting. Experimental success has been found in mitigating and suppressing NTMs by use of ECCD in AUG [44,45], DIII-D [46,47] and JT-60U [48]. Accurate targeting of the NTM can be achieved through active control diagnostics such as the 1 cm accuracy displayed by the DIII-D Plasma Control System (for reference a saturated  $3/2$  island width in DIII-D is 4 – 7 cm) [47,49].

## 1.5 The Synthetic Aperture Microwave Imaging diagnostic (SAMI)

The Synthetic Aperture Microwave Imaging diagnostic (SAMI) [50–52] operates in both a passive and active mode. In the active probing mode SAMI uses a single

antenna to launch a beam with an almost spherical wave-front of high divergence, to illuminate the full poloidal and toroidal view of the tokamak plasma, in a  $\pm 40^\circ$  angular spread. In either mode the diagnostic must receive a signal from the plasma which it does through its 8 receiving antennas. The antennas are positioned to allow the diagnostic to reconstruct a post-shot ‘beam’, whose constructed beam diameter decreases as number of antennas increases. The targeted location of the synthetic beam is dictated by phasing each antenna to “steer” the beam within the limits of the viewing angle.

### 1.5.1 Capabilities and motivation for this thesis

As discussed, one of the main challenges of fusion research is understanding and predicting the nature of the turbulent plasma edge. Fusion plasmas have an inherent rotation of the turbulent structures perpendicular to the magnetic field and radial electric field due to the  $\mathbf{E} \times \mathbf{B}$  drift. Further contributions from the phase velocity of the turbulence structures and toroidal spin of the bulk plasma combine to give a total velocity  $v_{\text{total}} = v_{\mathbf{E} \times \mathbf{B}} + v_{\text{phase}} + v_{\text{bulk}}$ . A Doppler reflectometer works in the same way as a normal reflectometer except the beam is now tilted away from the normal to the cut off surface. The beam interacts at an injected angle  $\theta$  with the corrugated cut off surface, composed of a spectrum of length scales  $k_{\text{turb}}$ , which are perpendicular to the magnetic field vector. According to the Bragg condition (1.2) a  $-1$  order reflection will be returned back down the beam line when the beam interacts with a specific  $k_{\text{turb}}$ .

$$k_{\text{turb}} = -2k_{\text{probe}} \sin \theta \quad (1.2)$$

According to the radar Doppler technique the returned beam has a Doppler shift associated with it according to (1.3).

$$f_{\text{D}} \approx 2 \frac{v}{c} f_{\text{probe}} \sin \theta \quad (1.3)$$

Using the assumption that  $v_{\text{phase}}$  and  $v_{\text{bulk}}$  are negligible compared with the  $\mathbf{E} \times \mathbf{B}$  velocity it is possible to extract a velocity of the turbulence ( $v_{\perp} \approx v_{\mathbf{E} \times \mathbf{B}}$ ). The phase velocity of the turbulence is the eddy turnover frequency which is typically in the kHz range multiplied by the fluctuation wavelength of the order 1 cm [53, 54]. So for 10 kHz one eddy turnover will occur in 0.1 ms. The  $\mathbf{E} \times \mathbf{B}$  velocity is expected to be in the 10  $\text{kms}^{-1}$  range [35], meaning for the same acquisition time of 0.1 ms, the turbulence will have moved by 1 metre. Considering that the probing beam used by both the single horn 1D Doppler reflectometry and by SAMI's phased array is a collimated beam of diameter  $\ll 1$  metre, the turbulence can be assumed to be frozen in, resulting in negligible phase velocity. The bulk plasma rotation which is toroidal is not in the same direction as the  $\mathbf{E} \times \mathbf{B}$  velocity which is binormal to the magnetic field and radial electric field. Therefore, only a small component will be present along the  $\mathbf{E} \times \mathbf{B}$  velocity vector and can be considered negligible. By extracting  $v_{\mathbf{E} \times \mathbf{B}}$  and thence given the known magnetic field strength, a radial electric field  $E_r = -v_{\mathbf{E} \times \mathbf{B}} B$  can be measured. Many measurements of this type have already been conducted with great success in 1D on a range of tokamaks [55, 56]. Similar techniques have been used to measure propagating density perturbations [35]. It has also been shown to measure fluctuation spectra in Tore Supra [57], zonal and sheared flows in the stellarator TJ-II [58], zonal flows to study the L-H transition in JET [59] and to measure the geodesic acoustic mode oscillations (GAM's) in AUG [60].

All current DBS systems use a single horn antenna which is steered to the desired angle (figure 1.3). SAMI has the unique capabilities of illuminating the plasma in a 2D  $\pm 40^\circ$  view and post processing can simultaneously focus anywhere on this plane [51, 52]. This has allowed the first measurement of a magnetic pitch angle via Doppler reflectometry to be taken by aligning the magnetic field perpendicular to the peak red and blue shifted signal [61]. Simultaneous measurements of the  $\mathbf{E} \times \mathbf{B}$  flow velocity of the turbulent structures is also possible through the detected Doppler shift. Though the extraction of an accurate velocity from the 2D DBS data has proved challenging. One of the main long term goals for the development of EMIT-3D in this thesis is to model SAMI in a fully 3D MAST geometry. The modelling will improve the understanding

of the Doppler shift profiles, improving the localisation technique of the Doppler peaks which in turn improves the pitch angle measurement. Furthermore, this understanding will provide the ability to extract a flow velocity from the 2D DBS data. The simulation through EMIT-3D will allow SAMI in future shots on NSTX-U and MAST-U, using a range of frequencies, to construct a magnetic pitch angle profile and velocity profile through the edge. It follows that it may be possible to extract the current density  $\mathbf{J}(r)$  and electric field  $\mathbf{E}(r)$  profiles through the edge from this data with high spatial and temporal resolution. Though this long term goal would require further development, it is the first time these measurements could be conducted simultaneously using a single diagnostic. Zonal flows (ZFs) and geodesic acoustic modes (GAMs), which manifest as a radial electric field fluctuation  $\mathbf{E}(r)$ , are important for understanding energy and particle transport barrier formation in the H-mode plasma edge [59,60,62,63] for which we currently have no consistent explanation. Moreover, the edge current density profile  $\mathbf{J}(r)$  plays an important roll in MHD stability and thus overall performance of the plasma which is crucial to building a stable steady state reactor [63–66].

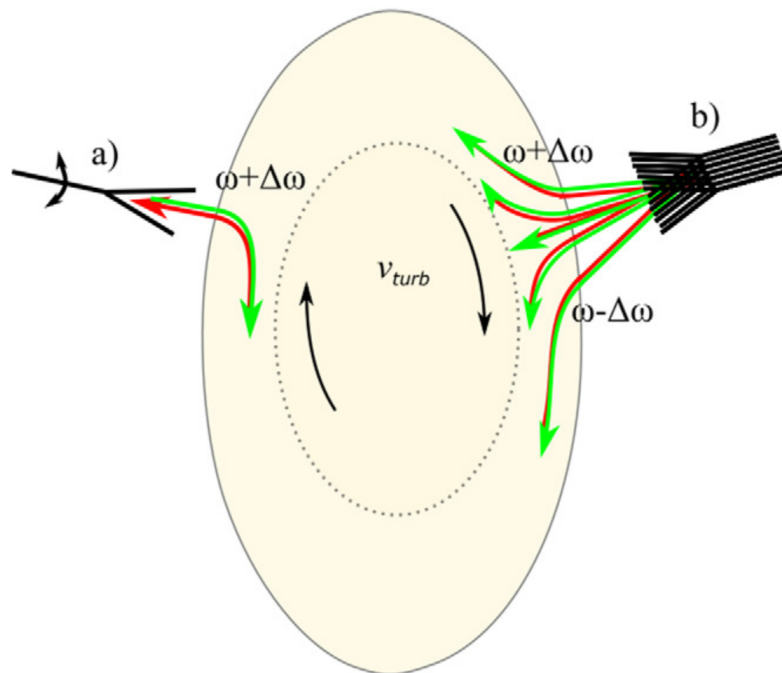


**Figure 1.3:** A cartoon illustration of the SAMI diagnostic. On the left the conventional single horn antenna is seen to launch a collimated microwave beam that reflects from a specific targeted location at a specific steering angle. On the right the SAMI method can be seen to illuminate the plasma at all angles. The ‘Beam’ is reconstructed post shot with a beam width and spatial accuracy defined by the number of receiving antennas. Reproduced with kind permission of Dr. D. Thomas.

This thesis is laid out in the following way. Chapter 2 will discuss the mathematical basis for modelling electromagnetic waves in magnetised plasmas from first principles and include a detailed discussion of the classification of the different wave modes. Building from this, the numerical formalism used in EMIT-3D is defined. Chapter 3 discusses the extensive code development that was ongoing throughout the Ph.D., beginning with the initial algorithm and resulting in the code as it is at the end of the Ph.D.. Chapter 4 details the use of EMIT-3D in collaboration with IPF-FDMC - a 2D full wave code developed at Stuttgart - to perform a parameter scan of microwave beam scattering by density fluctuations. Chapter 5 extends the scattering parameter scan of chapter 4 to a systematic study to resolve the cause of ECRH deposition profile broadening on the DIII-D tokamak. Chapter 6 is an aside to the core Ph.D. project and details the experimental investigation of asymmetric thrust from a plasma thruster with a view to optimisation. The thesis is concluded in chapter 7 which outlines future projects.

# Chapter 2

## Formalism of the wave mechanics

### 2.1 Theoretical formalism

#### 2.1.1 Wave definitions and plasma parameters

What follows are explanations of quantities that will be discussed in detail throughout this section along with some important plasma physics concepts.

**Polarisation:** The polarisation of the electromagnetic wave relates to the phase and magnitude of the orthogonal components of the electric field of the wave (for a fully transverse wave propagating in the  $z$  direction). If the two components (lets call these  $E_x$  and  $E_y$ ) are in phase then the wave is plane-polarised and the magnitude of the two components would represent a line between the peaks drawn in the  $x - y$  plane. If the two components are out of phase by exactly  $\pm 90$  degrees and the amplitude is the same then the magnitude of the two components will trace out a circle in a stationary  $x - y$  plane as the wave propagates through. This is a special case of the more general elliptical polarisation in which case the amplitudes are different, the phase difference is arbitrary or both. In mathematical form the polarisation is described by the Jones vector [67]. For a wave propagating along the  $z$  axis:

$$\begin{pmatrix} E_x(t) \\ E_y(t) \\ E_z(t) \end{pmatrix} = \begin{pmatrix} E_{0x}e^{i(kz-wt+\phi_x)} \\ E_{0y}e^{i(kz-wt+\phi_y)} \\ E_{0z}e^{i(kz-wt+\phi_z)} \end{pmatrix} + \text{c.c.} = \begin{pmatrix} E_{0x}e^{i\phi_x} \\ E_{0y}e^{i\phi_y} \\ E_{0z}e^{i\phi_z} \end{pmatrix} e^{i(kz-wt)} = \mathbf{a}_J e^{i(kz-wt)}$$

where  $\mathbf{a}_J$  is the Jones vector and represents relative amplitude and relative phase of the electric field in 3D. The sum of the squares of the electric field components is proportional to the intensity of light. The Jones vectors are then normalised by this. Therefore for a fully transverse wave (no  $z$  component) a Jones vector of  $(1, 0, 0)$  or  $(0, 1, 0)$  would represent horizontal and vertical linear polarisation respectively. By convention this is in relation to the  $x$ -axis.  $1/\sqrt{2} (1, 1, 0)$  would be at  $45^\circ$  in the  $x - y$  plane.  $1/\sqrt{2} (1, i, 0)$  and  $1/\sqrt{2} (1, -i, 0)$  are right and left handed circularly polarised waves. An elliptical polarisation in this formalism would have different associated amplitudes for  $x$  and  $y$ .

**Transverse vs longitudinal:** The magnitude of the wave's E-field as well as having a polarisation as discussed above can also be oriented at an angle to the wave vector  $\hat{\mathbf{k}}$ ; the E-field does not have to be at 90 degrees to the direction of propagation as in the purely transverse case. As the angle between  $\mathbf{E}$  and  $\hat{\mathbf{k}}$  becomes more acute,  $\mathbf{E}$  points towards the direction of propagation, exhibiting a longitudinal component. This causes more longitudinal acceleration of the medium particles and can be interpreted as conversion to an electrostatic mode from electromagnetic.

**Plasma and cyclotron frequency:** The two fundamental frequencies that play a large role in how a plasma reacts to perturbations are the plasma frequency and cyclotron frequency. The plasma frequency describes the electrostatic oscillation frequency at which a species responds to a small charge separation. The cyclotron frequency is the frequency at which a species undergoes circular motion around the magnetic field. Common normalisations to the propagating wave frequency are also

defined.

$$\omega_{p,s} = \sqrt{\frac{Z_s n e^2}{\epsilon_0 m_s}} \quad \omega_{c,s} = \frac{q_s B}{m_s} \quad Y = \frac{\omega_{c,s}}{\omega} \quad X = \left(\frac{\omega_{p,s}}{\omega}\right)^2 \quad (2.1)$$

Both frequencies have a dependency on mass of the species,  $s$ , therefore the electron frequency has the faster response time to perturbations than ions. Both the ion and electron cyclotron frequencies are important for heating the plasma.

### 2.1.2 Derivation of dispersion relation

In order to evaluate the behaviour of a wave through a plasma one must analyse the plane wave solutions and input these into Maxwell's equations (2.2) to find the dispersion relations of the form  $\omega = \Omega(\mathbf{r}, \mathbf{k})$ .

$$\nabla \times \mathbf{E} = -\frac{\partial \mathbf{B}}{\partial t}; \quad \nabla \times \mathbf{B} = \mu_0 \mathbf{J} + \frac{1}{c^2} \frac{\partial \mathbf{E}}{\partial t} \quad (2.2)$$

Maxwell's equations are linear, non linearity arises due to the equation for current density in the plasma. The equation for current density can be expanded to higher order terms as shown below:

$$\mathbf{J}_1 = \alpha \mathbf{E}_1 + \beta \mathbf{B}_1 + \gamma \mathbf{E}_1^2 + \delta \mathbf{E}_1 \mathbf{B}_1 n + \dots$$

By assuming small amplitude waves such that  $\mathbf{E}_0^2 \ll \mathbf{E}_0$  then this reduces to a linear equation in  $\mathbf{J}$ . With the implementation of this approximation one can find internally consistent plane wave solutions,  $\mathbf{E} = \mathbf{E}_0 e^{i(\mathbf{k} \cdot \mathbf{r} - \omega t)} + \text{c.c.}$ , where the frequency doesn't change throughout propagation. One other way to think of this approximation is through the energy exchanged with the plasma. By assuming small amplitude, one can say that the energy density of the wave ( $\epsilon E^2/2 + B^2/(2\mu_0)$ ) is much smaller than that of the plasma ( $nkT$ ). Here  $\epsilon = \epsilon_0 \epsilon_r$ . Thus proportionally the wave does not heat the plasma and so energy is conserved. It should be noted that although using the cold plasma regime, the plasma can not be so cold that it violates the assumption of

no energy exchange and thus the linearisation of the current density  $\mathbf{J}$ . By assuming a plane wave solutions  $\nabla \mapsto ik$  and by also assuming a monochromatic wave  $\frac{\partial}{\partial t} \mapsto -i\omega$  the two Maxwell equations (2.2) become:

$$\mathbf{k} \times \mathbf{E} = \omega \mathbf{B}; \quad i\mathbf{k} \times \mathbf{B} = \mu_0 \mathbf{J} - \frac{i\omega}{c^2} \mathbf{E}$$

which implies.

$$\mathbf{k} \times (\mathbf{k} \times \mathbf{E}) \frac{i}{\omega} = \mu_0 \mathbf{J} - \frac{i\omega \mathbf{E}}{c^2}$$

$$\mathbf{J} = \frac{i}{\mu_0 \omega} [\mathbf{k} \times (\mathbf{k} \times \mathbf{E})] + \frac{i\omega^2}{c^2} \frac{\mathbf{E}}{\omega \mu_0} \quad (2.3)$$

Following this a matrix equation can be obtained relating current density, conductivity tensor and electric field,  $\mathbf{J} = \underline{\underline{\sigma}} \cdot \mathbf{E}$ . One can then develop a matrix equation of the form  $\underline{\underline{\mathbf{M}}} \cdot \mathbf{E} = 0$ . The matrix  $\underline{\underline{\mathbf{M}}}$  contains the information of the dispersion relation [68]. Following on from equation (2.3), the matrix  $\underline{\underline{\mathbf{M}}}$  is found:

$$\mathbf{J} = \frac{i}{\mu_0 \omega} [\mathbf{k}(\mathbf{k} \cdot \mathbf{E}) - \mathbf{E}(\mathbf{k} \cdot \mathbf{k})] + \frac{i\omega^2}{\mu_0 \omega c^2} \mathbf{E}$$

$$\mathbf{J} = \frac{i}{\mu_0 \omega} \left[ \mathbf{k}\mathbf{k} - k^2 \underline{\underline{\mathbf{I}}} + \frac{\omega^2}{c^2} \underline{\underline{\mathbf{I}}} \right] \cdot \mathbf{E} \quad (2.4)$$

$$0 = \left[ \mathbf{k}\mathbf{k} - k^2 \underline{\underline{\mathbf{I}}} + \frac{\omega^2}{c^2} \underline{\underline{\mathbf{I}}} \right] \cdot \mathbf{E} + i\mu_0 \omega \underline{\underline{\sigma}} \cdot \mathbf{E} = \underline{\underline{\mathbf{M}}} \cdot \mathbf{E}$$

where  $\underline{\underline{\mathbf{I}}}$  is the identity matrix.

$$\underline{\underline{\mathbf{M}}} = \mathbf{k}\mathbf{k} - k^2 \underline{\underline{\mathbf{I}}} + \frac{\omega^2}{c^2} \left( \underline{\underline{\mathbf{I}}} + \frac{i\underline{\underline{\sigma}}}{\epsilon_0 \omega} \right) \quad (2.5)$$

The dielectric permittivity tensor  $\underline{\underline{\epsilon}}$  is defined as:

$$\underline{\underline{\epsilon}} = \underline{\underline{\mathbf{I}}} + \frac{i\sigma}{\epsilon_0\omega} \quad (2.6)$$

Without loss of generality one can deduce that all  $k_y = 0$  and  $k_x = k_\perp, k_z = k_\parallel$ .

$$\underline{\underline{\mathbf{M}}} = \begin{pmatrix} (\frac{\omega^2}{c^2}\epsilon_{1,1}) - k_\parallel^2 & 0 + (\frac{\omega^2}{c^2}\epsilon_{1,2}) & (\frac{\omega^2}{c^2}\epsilon_{1,3}) + k_\parallel k_\perp \\ 0 + (\frac{\omega^2}{c^2}\epsilon_{2,1}) & (\frac{\omega^2}{c^2}\epsilon_{2,2}) - k_\parallel^2 - k_\perp^2 & 0 + (\frac{\omega^2}{c^2}\epsilon_{2,3}) \\ (\frac{\omega^2}{c^2}\epsilon_{3,1}) + k_\parallel k_\perp & 0 + (\frac{\omega^2}{c^2}\epsilon_{3,2}) & (\frac{\omega^2}{c^2}\epsilon_{3,3}) - k_\perp^2 \end{pmatrix}$$

The level of complexity of the physics model necessary to describe the material the wave is propagating through is identified at this stage and applied to the matrix through the conductivity tensor. The following describes the force balance equation without the inclusion of a background current density or temperature terms. The model is known as the cold plasma model.

$$\begin{aligned} m \frac{dv_x}{dt} &= q(E_x + v_y B_0) \\ m \frac{dv_y}{dt} &= q(E_y - v_x B_0) \\ m \frac{dv_z}{dt} &= qE_x \end{aligned}$$

Using  $\partial/\partial t = -i\omega$ , and substituting  $v_x$  into  $v_y$  and vice-versa one arrives at the following equations for velocity.

$$\begin{aligned} v_x &= \frac{iq}{m\omega} \frac{(E_x + i\frac{\omega_c}{\omega} E_y)}{(1 - (\frac{\omega_c}{\omega})^2)} \\ v_y &= \frac{iq}{m\omega} \frac{(E_x - i\frac{\omega_c}{\omega} E_y)}{(1 - (\frac{\omega_c}{\omega})^2)} \\ v_z &= \frac{iq}{m\omega} E_z \end{aligned}$$

These definitions for velocity are used in the equation  $J = en_{0,i}v_i - en_{0,e}v_e$  and produce a matrix equation for the conductivity  $\underline{\underline{\sigma}}$ . The substitutions for Y and X defined in

(2.1) have been used.

$$\begin{aligned}\frac{i}{\epsilon_0\omega}J_x &= -X_i\frac{E_x + iY_iE_y}{1 - Y_i^2} - X_e\frac{E_x + iY_eE_y}{1 - Y_e^2} \\ \frac{i}{\epsilon_0\omega}J_y &= -X_i\frac{E_y - iY_iE_x}{1 - Y_i^2} - X_e\frac{E_y - iY_eE_x}{1 - Y_e^2} \\ \frac{i}{\epsilon_0\omega}J_z &= -X_iE_z - X_eE_z\end{aligned}$$

These expressions can be simplified further by noting that  $m_i \gg m_e$  which means that  $\omega_{p,i} \ll \omega_{p,e}$ . Therefore the ion contribution is negligible compared to that of the electrons. As the work in this thesis focuses on waves in the electron cyclotron range ( $\omega_{c,e} \approx \omega \gg \omega_{c,i}$ ), this is a reasonable approximation. The conductivity tensor becomes:

$$\begin{pmatrix} J_x \\ J_y \\ J_z \end{pmatrix} = \begin{pmatrix} -\frac{X}{1-Y^2} & -\frac{XY}{1-Y^2} & 0 \\ \frac{XY}{1-Y^2} & -\frac{X}{1-Y^2} & 0 \\ 0 & 0 & -X \end{pmatrix} \frac{\epsilon_0\omega}{i} \cdot \begin{pmatrix} E_x \\ E_y \\ E_z \end{pmatrix}$$

Substituting this matrix for  $\underline{\underline{\sigma}}$  into  $\underline{\underline{\epsilon}}$ .

$$\underline{\underline{\epsilon}} = \begin{pmatrix} 1 - \frac{X}{1-Y^2} & -\frac{iXY}{1-Y^2} & 0 \\ \frac{iXY}{1-Y^2} & 1 - \frac{X}{1-Y^2} & 0 \\ 0 & 0 & 1 - X \end{pmatrix} = \begin{pmatrix} S & -iD & 0 \\ iD & S & 0 \\ 0 & 0 & P \end{pmatrix}$$

The following definitions have been used:

$$R = 1 - \frac{X}{1+Y}, \quad L = 1 - \frac{X}{1-Y}, \quad P = 1 - X \quad (2.7)$$

$$\begin{aligned}S &= \frac{R+L}{2} = 1 - \frac{X}{1-Y^2} \\ D &= \frac{R-L}{2} = \frac{XY}{1-Y^2}\end{aligned}$$

where R, L and P are expressions for the right and left hand polarised EM waves and the electrostatic plasma wave. These will be discussed later in section 2.1.4. This

matrix for  $\underline{\underline{\epsilon}}$  can now be put back in  $\underline{\underline{\mathbf{M}}}$ .

$$\underline{\underline{\mathbf{M}}} = \begin{pmatrix} \frac{\omega^2}{c^2}S - k_{\parallel}^2 & -i\frac{\omega^2}{c^2}D & k_{\parallel}k_{\perp} \\ i\frac{\omega^2}{c^2}D & \frac{\omega^2}{c^2}S - k_{\parallel}^2 - k_{\perp}^2 & 0 \\ k_{\parallel}k_{\perp} & 0 & \frac{\omega^2}{c^2}P - k_{\perp}^2 \end{pmatrix} \quad (2.8)$$

One can multiply through by  $\frac{c^2}{\omega^2}$  and use  $N = \frac{kc}{\omega}$  to work in terms of the refractive index. By also identifying  $\theta$  as the angle between  $\hat{k}$  and  $\hat{z}$  then,  $N_x = N \sin(\theta)$ ,  $N_y = 0$ ,  $N_z = N \cos(\theta)$ , The following matrix is obtained.

$$\underline{\underline{\mathbf{M}}} = \begin{pmatrix} S - N^2 \cos^2(\theta) & -iD & N^2 \sin(\theta) \cos(\theta) \\ iD & S - N^2 & 0 \\ N^2 \sin(\theta) \cos(\theta) & 0 & P - N^2 \sin^2(\theta) \end{pmatrix} \quad (2.9)$$

By the Cayley-Hamilton theorem [68] solutions exist for the equation  $\underline{\underline{\mathbf{M}}} \cdot \mathbf{E} = 0$  where  $\text{Det}(\underline{\underline{\mathbf{M}}}) = 0$ . Following some algebraic manipulations the cold plasma dispersion relation can be obtained [69].

$$\tan^2(\theta) = \frac{-P(N^2 - R)(N^2 - L)}{(SN^2 - RL)(N^2 - P)} \quad (2.10)$$

### 2.1.3 Analysis of dispersion relation

By looking at the dispersion relation (2.10) found from the cold plasma approximation one can analyse the form of the wave propagating both parallel ( $\theta = 0$ ) and perpendicular ( $\theta = \pi/2$ ) to the magnetic field.

#### 2.1.3.1 Propagation parallel to the magnetic field

For  $\theta = 0 \Rightarrow \tan^2(\theta) = 0$  there are three wave solutions of the form:

$$N_{\parallel}^2 = L = 1 - \frac{X}{1 - Y}; \quad N_{\parallel}^2 = R = 1 - \frac{X}{1 + Y}; \quad P = 0 = 1 - X \quad (2.11)$$

Two of these modes are the right and left handed circularly polarised electromagnetic waves (R-mode and L-mode). This can be seen more clearly through the eigenvectors

which can be identified by considering the middle row of the matrix equation (2.9) with  $\theta = 0$ ,  $iDE_x + (S - N^2)E_y = 0$ . Thus by substituting  $N^2 = R$  and  $N^2 = L$

$$\frac{iE_x}{E_y} = -\frac{(S - R)}{D} = 1 \quad \frac{iE_x}{E_y} = -\frac{(S - L)}{D} = -1$$

Therefore the eigenvectors for the right and left handed polarisation are  $(E_x, iE_x, 0)$  and  $(E_x, -iE_x, 0)$  respectively. The third is the electrostatic wave (eigenvector  $(0, 0, E_z)$ ) with frequency equal to the plasma frequency ( $\omega = \omega_{p,e}$ ). As this oscillates parallel to the magnetic field there is no magnetic contribution to the Lorentz force so the background magnetic field has no effect on the mode dynamics [70]. The distinct modes have different phase velocities and so propagate at different speeds giving rise to independent waves all of which come from the same initial excitation. The R-mode electric field rotates in the same direction as the cyclotron oscillation of the electrons. Therefore if the field rotates at the same velocity there is strong absorption of the R-mode by electrons as they are continuously accelerated [70]. This resonance happens as  $N^2 \rightarrow \pm\infty$  corresponding to  $R \rightarrow \pm\infty$  meaning that  $Y \rightarrow -1$ . It is noted that we are looking at the higher frequency electron cyclotron range for which  $\omega_{c,e}$  has a negative sign and so Y is negative. Therefore, this happens as  $\omega \rightarrow \omega_{c,e}$ . At lower frequencies there will be interaction with the ion cyclotron frequency as  $L \rightarrow \pm\infty$  and  $Y \rightarrow 1$ . Here we only consider the lower ion frequencies as Y is positive because  $\omega_{c,i}$  is positive and  $\omega \rightarrow \omega_{c,i}$ . It is therefore evident that the same physics occurs for both modes resulting in two different resonant frequencies. Furthermore for frequencies just above the cyclotron frequency  $N^2$  becomes negative suggesting that the wave experiences a cut-off and exists in a region of evanescence where N is imaginary [70]. Evanescence in this sense describes the spatial attenuation of a wave that is a result of kinematic or electromagnetic reasons. Increasing the frequency further, one finds that  $N^2$  becomes positive again allowing the wave to propagate. Consequently there must exist a frequency for both the L- and R-mode above which the wave can propagate again. By substituting  $N^2 = 0$  into the equation for R-mode in (2.11) one obtains the

following:

$$1 + Y = X \quad \mapsto \quad \omega^2 + \omega\omega_c - \omega_p^2 \simeq 0$$

Note the approximation made earlier neglecting ion contribution is still valid where the  $\simeq$  has been used to acknowledge the neglected  $\omega_{c,i}$  terms. The above equation has one positive root resulting in a cut-off frequency above which the wave can propagate again. Similarly by considering the L-mode one can find a second cut-off frequency above the ion cyclotron frequency:

$$\omega_R \simeq \frac{|\omega_{c,e}|}{2} + \sqrt{\frac{\omega_{c,e}^2}{4} + \omega_{p,e}^2}; \quad \omega_L \simeq -\frac{|\omega_{c,e}|}{2} + \sqrt{\frac{\omega_{c,e}^2}{4} + \omega_{p,e}^2} \quad (2.12)$$

Each mode has one resonance (R at  $\omega_{c,e}$  and L at  $\omega_{c,i}$ ) and two cut-off points (R at  $\omega_R$ , L at  $\omega_L$ ).

### 2.1.3.2 Propagation perpendicular to the magnetic field

For  $\theta \rightarrow \pi/2$ ,  $\tan^2(\theta) \rightarrow \infty$  one finds two propagating wave solutions (for the cold plasma approximation) which are purely a result of the background magnetic field interacting with the wave. They take the form:

$$N_{\perp}^2 = P = 1 - X; \quad N_{\perp}^2 = \frac{RL}{S} = \frac{(1 - X - Y)(1 - X + Y)}{1 - X - Y^2} \quad (2.13)$$

The first solution has the simplest dispersion relation and is labelled the ordinary mode (O-mode). It can be seen from the matrix equation (2.9) with  $\theta = \pi/2$  that this solution has eigenvector  $(0, -iE_x/Y, 0)$ . Subsequently the wave is a linearly polarised purely electromagnetic wave with its electric field aligned parallel to the background magnetic field ( $\mathbf{B}_0$ ). The second solution has a rather complicated dispersion relation with both longitudinal and transverse E-field components. Consequently, the propagation of this mode depends on the strength of  $\mathbf{B}_0$ . Hence this is labelled as the extraordinary mode (X-mode) with associated eigenvector  $(E_x, iE_x S/D, 0)$ . Again the distinct modes have different phase velocities and so propagate at different speeds giving rise to independent waves all of which come from the same initial excitation. It is noted that as  $N^2 = 0$

then  $R, L, P \rightarrow 0$  as for parallel propagation [70]. Hence, the cut-off frequencies are independent of the angle of propagation and are fully described by the treatment in section 2.1.3.1. The cut off points at  $\omega_R$  and  $\omega_L$  apply to the X-mode only and the cut-off at  $\omega_{p,e}$  applies to the O-mode only. In addition for X-mode, a new resonant frequency occurs where  $N^2 \rightarrow \pm\infty$  which arises at the zeros of  $S$ .

$$S = 0 = 1 - \frac{X}{1 - Y^2} \quad \rightarrow \quad \omega_{UH} = \sqrt{\omega_{p,e}^2 + \omega_{c,e}^2} \quad (2.14)$$

This resonant frequency is a mixture of both the electron cyclotron frequency and the electron plasma frequency and is called a hybrid frequency. Moreover, it is important to note that this frequency specifically relates to the electron frequencies only and is called an upper hybrid resonance (UHR) as it is greater than both  $\omega_{c,e}$  and  $\omega_{p,e}$ . Another hybrid frequency can be found by relaxing the stationary ion approximation which involves the ion frequencies (lower hybrid frequency). The following equation for the lower hybrid frequency has the form as given in [70].

$$\omega_{LH} = \sqrt{\frac{\omega_{c,e}^2 \omega_{c,i}^2 + \omega_{p,i}^2 \omega_{c,e}^2}{\omega_{p,e}^2 + \omega_{c,e}^2}} \quad (2.15)$$

The lower hybrid frequency lies between the ion cyclotron frequency and electron cyclotron frequency. It is noted that if more ion species were introduced one would find more hybrid frequencies, for each new species, lying between the two ion species. The cold plasma model does not reproduce the resonant frequencies at the cyclotron frequency. This is because in the cold plasma model the temperature is zero and the Larmour orbit is zero. Therefore, as viewed from a perpendicular direction there is no orbital frequency with which to interact. However, I will note here that O-mode and X-mode both have resonances at  $\omega_{c,e}$  and  $\omega_{c,i}$ . As the mathematics is not present a qualitative explanation is given. For O-mode because  $\mathbf{E}_1 \parallel \mathbf{B}_0$  then when  $\omega = \omega_{c,s}$ , the particle is periodically accelerated in the direction of the magnetic field when the particle periodically returns to the same point in its Larmor orbit. Similarly for X-mode, the particle is accelerated periodically, perpendicular to the magnetic field when the wave electric field periodically aligns with the velocity vector of the particle. To

conclude, in this model the X-mode has two cut-off points at  $\omega_R$  and  $\omega_L$  and one resonance at  $\omega_{UH}$ . O-mode has one cut off at  $\omega_{p,e}$ .

### 2.1.3.3 Propagation at arbitrary angle

In the following I have tried to be as careful and logical with the wave mode labelling as I can. Much of the literature drop specifications and describe wave modes interchangeably which can cause confusion. From the above treatment it is evident that the propagating wave modes can be labelled thoroughly through the following parameters:

- Fast or slow depending on its phase velocity.
- X-mode and O-mode polarisations according to the dispersion relation at  $\theta = \pi/2$ .
- R-mode, L-mode, P-mode polarisations according to the dispersion relation at  $\theta = 0$ .

It is noted that the waves may also be labelled according to the shape of the wave normal surfaces although this will not be discussed here [69]. Due to the principle of superposition the wave modes at arbitrary angle are some superposition of the pure mode polarisations found above. The equation to describe cold plasma EM electron modes at arbitrary angle was developed independently by three scientists H.K Lassen, E.V. Appleton and D. Hartree and so shall be referred to as the Lassen-Appleton-Hartree equation. The derivation of the equation is extensive so shall not be included here and instead quoted as it is written in [69].

$$N^2 = 1 - \frac{2X(1-X)}{2(1-X) - Y^2 \sin^2(\theta) \pm \Delta} \quad (2.16)$$

$$\Delta = [Y^4 \sin^4(\theta) + 4(1-X)^2 Y^2 \cos^2(\theta)]^{1/2}$$

The equation reveals that the solutions to the dispersion relation at  $\theta = 0$  are related to the solutions at  $\theta = \pi/2$  and are not different entities. In fact as the angle is varied from  $0 \rightarrow \pi/2$ , the L-mode 'morphs' into the slow O-mode and the R-mode into the X-mode. Therefore at an arbitrary angle one cannot simply define the mode to be

distinctly O or L or distinctly X or R. The mode has the dispersion relation properties of the O-mode and is left handed circularly polarised [69]. The  $\pm$  in the above equation corresponds to the quasi-transverse propagating L/O-mode (+) and quasi-transverse propagating R/X-mode (-). As the wave begins to propagate at some angle into the plasma the solutions split into their respective modes due to different phase velocities as the slow L/O-mode and fast R/X-mode and slow L/X-mode. I will denote the slow X-mode as L/X perhaps unusually because this X-mode is reflected at the left hand cut-off  $\omega_L$ , whereas the fast R/X-mode is reflected at the right hand cut-off  $\omega_R$  (figure 2.2). Because these modes are formed from the principle of superposition the individual frequencies identified as the cut-off and resonance apply at arbitrary angle for the ‘mixed’ modes. Taking the frequencies derived above one can see the hierarchy of resonant frequencies is as follows for a constant magnetic field and density in an under dense plasma. The positions of  $\omega_L$  and  $\omega_R$  are different for over dense plasmas.

$$\omega_{c,i} < \omega_{LH} < \omega_L < \omega_{c,e} < \omega_{UH} < \omega_R$$

The cut-off at the plasma frequency is not listed in this hierarchy because its location depends whether the plasma is under ( $\omega_{c,e} > \omega_{p,e}$ ) or over ( $\omega_{c,e} < \omega_{p,e}$ ) dense as described in chapter 1, section 1.3.

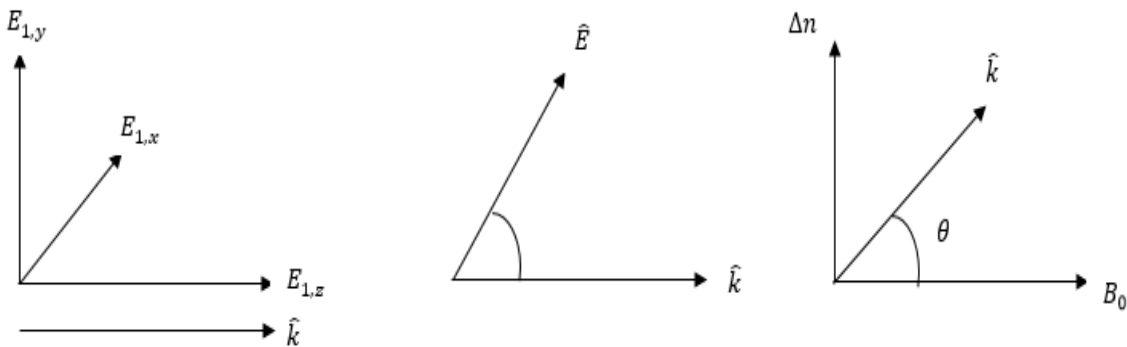


**Figure 2.1:** Illustration of the orientation of the wave vector and background magnetic field and density gradient. The middle figure illustrates that the wave can have longitudinal components in a plasma with  $\hat{\mathbf{E}}$  being the total electric field.

Before tackling more complex problems it is useful to have an understanding of the physical changes that the wave undergoes during resonance and cut-off. Figure 2.2

plots the solutions to the dispersion relation at perpendicular propagation for O-mode and X-mode at a fixed background magnetic field and wave frequency ( $Y = 0.5$ ). The plotted solution is in terms of phase and group velocity normalised to the vacuum velocity as a function of  $X$ . The horizontal axis is a function of the plasma density through  $\omega_{p,e}^2$  as  $\omega$  is fixed.

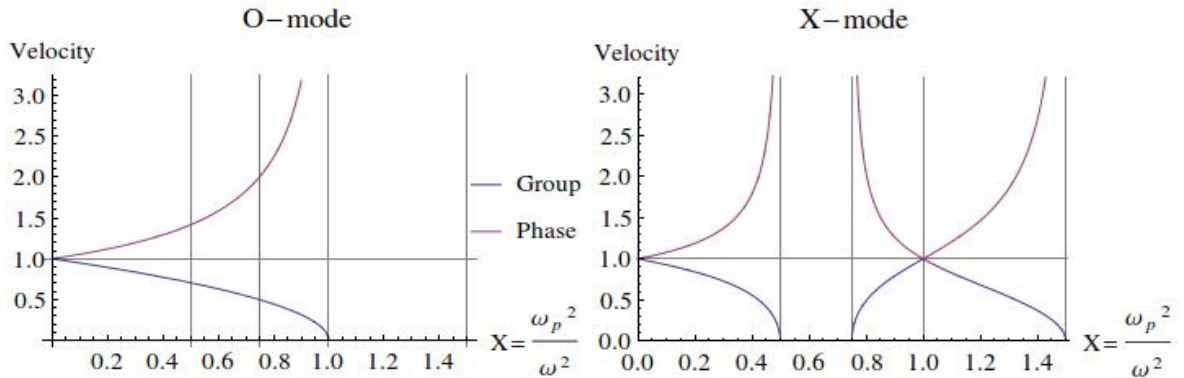


**Figure 2.2:** The group and phase velocity as a function of  $X$  for the O-mode (left) and X-mode (right) for a fixed wave frequency and background magnetic field ( $Y = 0.5$ ). The velocity is normalised to the speed of light in a vacuum. The vertical lines denote the cut-off and resonance locations. From left to right they are:  $\omega_R$ ,  $\omega_{UH}$ ,  $\omega_{p,e}$ ,  $\omega_L$

One can see that the fast X-mode is reflected from the right hand cut off at  $X = 0.5$ . The slow X-mode solution arises between the UHR at  $X = 0.75$  and the left hand cut-off at  $X = 1.5$ . The slow O-mode experiences its cut off at  $X = 1$ . At a cut off the group velocity goes to zero and the phase velocity goes to infinity (conservation of energy). As the group velocity carries the information it is logical for this to decrease to zero and become negative in reflection. At a resonance the same occurs as the energy is transferred to the resonating species through the phase velocity rendering the wave's group velocity zero. It can also be visualised that the wavelength becomes shorter and asymptotes to zero as it is absorbed. By inputting  $Y = 0.5$  and  $X = 1$  into equation 2.13 for the X-mode dispersion relation, one can see that the phase velocity and therefore the group velocity equals the speed of light at  $X = 1$ .

#### 2.1.4 Mode conversion

From the determinant of the matrix in equation (2.8) a quadratic in  $k_{\perp}^2$  (a bi-quadratic) is obtained for arbitrary propagation angle and thus there are two solutions for  $k_{\perp}^2$ . This is the same as the Lassen-Appleton-Hartree solutions discussed above. These

solutions describe two, real, distinctly separate modes which behave differently from one another. Mode conversion refers to a region where the dispersion relation of the wave becomes degenerate so that the two solutions are coincident. Within this region the wave may convert to behaving as the other mode with an efficiency of  $\leq 100\%$ . In the high density limit where  $X = 1$  (density equals the critical density) and for  $\hat{\mathbf{k}} \parallel \mathbf{B}_0$  then  $\Delta = 0$  and the Lassen-Appleton-Hartree dispersion relation in equation (2.16) is identical for the two modes. That is to say that in the case of the slow L/O-mode in a changing background density,  $\nabla n$ , the solution to the dispersion relation changes smoothly becoming degenerate such that a second mode arises, the slow L/X-mode. One can find a nominal refractive index at which this can occur.

$$N_{\parallel, \text{opt}}^2 = \frac{Y|_{X=1}}{Y|_{X=1} + 1} \sin^2 \theta$$

At optimum propagation refractive index then there is 100% mode conversion from O-X and no evanescent region occurs. However if sub optimal, through a change in propagation angle or plasma parameters then there exists an evanescent region through which the wave would tunnel. This tunnelling is described by the WKB approximation and results in a probability of conversion which defines a window of parameter values for which O-X mode conversion will happen. As the parameter values deviate from the ideal conversion values the intensity of the produced X-mode reduces and the intensity of reflected O-mode increases. If no X-mode is produced then there is simply reflection of the O-mode at the critical density such as when O-mode is incident normal to the density cut-off surface and reflected back. Previous work by Hansen *et. al.* [71] showed that a specific solution to Mjølhus' formula [72] was the best description for the coupling efficiency of O-X mode conversion:

$$T = \exp\left[-\pi \frac{\omega}{c} L_n \sqrt{\frac{Y}{2}} [2(1+Y)(N_{\parallel, \text{opt}} - N_{\parallel})^2 + N_{\parallel}^2]\right] \quad (2.17)$$

When the assumptions used so far are relaxed and temperature terms are introduced another solution to the dispersion relation at perpendicular propagation arises. This is the electron Bernstein wave (EBW) and is fully electrostatic. Similar to the

plasma oscillation (P-mode) found in parallel propagation the EBW can only be accessed within the plasma and so must couple to the electromagnetic modes to be detected outside of the plasma or be excited by an external antenna. The EBW couples to the X-mode (either fast or slow) at the UHR when the wavelength becomes shorter and the phase velocity becomes comparable to the electron thermal velocity. The EBW is formed by collective electron gyromotion which appears as oscillations in charge density and propagates from the upper hybrid resonance to higher densities within the plasma. EBW's are outside of the scope of this thesis and so a detailed analysis is not presented.

### 2.1.5 Magnetised 2D plasma slab

The cold plasma model was applied to a 2D slab of magnetised plasma to visualise how these modes behave in a rudimentary tokamak-like plasma. The  $y$ -axis points perpendicular to the magnetic field (analogous to pointing from the outer wall to the inner wall of the tokamak) and the  $z$ -axis is parallel to the magnetic field as in figure 2.1. The fixed parameters are shown in the table below (the initial  $\theta$  has been fixed by fixing  $k_{\parallel}$ ).

Parameter	Value
$\omega$	$6.283 \times 10^{10} \text{ rad s}^{-1}$
$n_e$	$(10^{19} \text{ m}^{-3})y$
$k_{\parallel}$	$0.34 \text{ cm}^{-1}$
$v_{th}$	$0.05c$
$B_0$	$0.3\hat{e}_z \text{ T}$

**Table 2.1:** The fixed parameters of the plasma slab.

*Mathematica* was used to analyse the matrix in equation (2.10), section 2.1.2. Firstly the determinant of the matrix (2.9) is taken resulting in the bi-quadratic in  $k_{\perp}^2$  and solved to find the four values of  $k_{\perp}$ . The dispersion relations found in section 2.1.2 determine the evolution of the wave as it enters the plasma. From these one can plot a graph of  $k_{\perp}^2$  vs  $X(= \omega_p^2/\omega^2)$  to visualise the behaviour of the different modes.

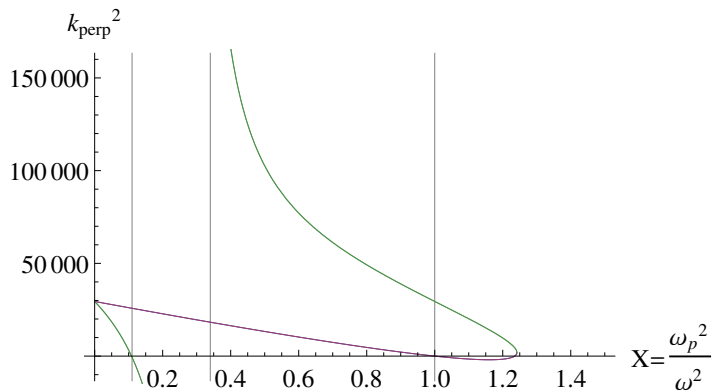


**Figure 2.3:** The behaviour of the wave in terms of the square of its wave vector (right) perpendicular to the background magnetic field as it propagates through the plasma. The vertical lines from right to left are the right hand cut-off, the upper hybrid resonance and the O-mode cut-off. The purple line denotes 2 solutions forward and backward.

The horizontal axis of figure 2.3 is a linear function of the distance into the plasma as  $\omega_{p,e}^2$  depends on the density profile which is linear in this model. The vertical axis shows the orientation of the wave relative to the magnetic field vector as it moves through the plasma. The solutions to the dispersion relation determine the behaviour of the waves and thus the path taken. There are two locations where the solution becomes imaginary,  $N^2 \leq 0$ , and one point where the solution diverges,  $N^2 \rightarrow \pm\infty$ . These are the cut-off/evanescence points where the wave is either reflected or may tunnel through with a probability as described by the WKB approximation and resonance where the wave is absorbed.

By plotting the different dispersion relations one finds that the four solutions of the bi-quadratic in  $k_{\perp}^2$  result in the following waves. The lower line originating from  $X = 0$ , which I will call the first solution, is the fast R/X-mode which splits off immediately and propagates to the right hand cut-off ( $\omega = \omega_R$ ). The upper line originating from  $X = 0$  describes the L/O-mode and contains the second and third solutions. The second solution is the forward going wave which propagates up to its cut-off at  $\omega = \omega_{p,e}$ . The third solution is the reflection from that cut-off surface returning back out of the plasma towards low density. From this figure more information is revealed about the wave propagation than was revealed by the mathematical analysis alone.  $k_{\perp}^2$  reduces from its initial value to zero which means that the angle between the wave-vector and the magnetic field vector is reducing to zero such that it propagates parallel to the magnetic field at the cut-off.

At this point the wave enters the region of evanescence ( $N_{\perp}^2 \leq 0$ ) and the solution to the dispersion relation becomes degenerate such the wave is described equally by the X- and O-modes. There is therefore the possibility for the L/O-mode to convert to the L/X-mode in this region. In this model the wave continues to propagate, described by the WKB approximation, in the positive  $x$  direction for a small distance. During which it is converted to the slow L/X-mode with an efficiency given in (2.1.4) which then reverses direction and propagates towards low density where it is absorbed at the UHR.

The fundamental resonance and cut-off frequencies change as a function of distance in to the plasma. Figure 2.4 displays a plot of the frequencies as a function of  $X$  showing the points of intersection with cut-off and resonance and can be compared directly to figure 2.3. Note the lower hybrid resonance and ion frequencies are too low to be displayed (of order  $10^7$ ) and do not affect the dynamics of the wave.

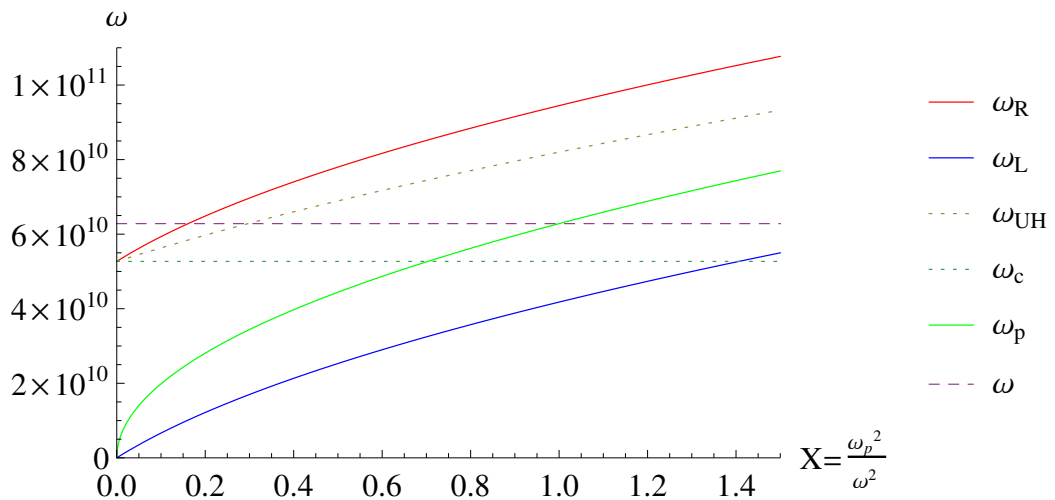


**Figure 2.4:** The change in the fundamental resonance and cut-off frequencies as a function of distance into the plasma. The horizontal axis is a proxy for distance as it is a function of the density through  $\omega_{p,e}$ . Dotted lines denote resonance, solid denote cut-off.

## 2.2 Computational formalism

### 2.2.1 Numerical methods

What follows is a brief description of the computational methods that may be employed to solve Maxwell's equations and conduct electromagnetic wave analysis in fusion rel-

evant plasmas.

### 2.2.1.1 Ray tracing

The most common treatment of wave propagation is through the use of ray and beam tracing codes. Ray tracing uses geometrical optics to track the path of a single ray through a plasma with slowly varying refractive index, useful for predicting the beam path through a tokamak plasma. The ray equations in terms of the determinant of the dispersion relation matrix  $D \equiv \text{Det}(\underline{\mathbf{M}})$  are:

$$\frac{d\mathbf{r}}{dt} = -\frac{\partial D/\partial \mathbf{k}}{\partial D/\partial \omega}; \quad \frac{d\mathbf{k}}{dt} = \frac{\partial D/\partial \mathbf{r}}{\partial D/\partial \omega}; \quad \frac{d\omega}{dt} = \frac{\partial D/\partial t}{\partial D/\partial \omega} \quad (2.18)$$

Beam tracing takes this approach a step further by launching many rays and by keeping track of the phase of each ray, can account for the interference between the rays to reconstruct a beam profile at any desired location. An extensive comparison of a selection of widely used codes is presented in Ref. [73]. These codes do not incorporate the scattering effects of turbulence on the beam propagation. However, due to the necessity to predict beam broadening in ITER for considering the power required to stabilise NTMs, attempts to include statistical models of turbulence have been undertaken. A number of different methods exist which have been able to demonstrate some scattering effects which have resulted in predictions of significant broadening of the ECRH beam on ITER in some scenarios of up to 100% [74–78].

However, the ray formulation is valid only when either the structure size is not the same order as the wavelength or the fluctuation level is not so large that the density gradient changes on the same length scale as the wave [69, 70]. Therefore no one analytic method includes the scattering effect of the full continuous  $k$  spectrum (from small to large structures) of the turbulence nor the full spread in fluctuation amplitudes observed in a tokamak plasma edge. Though the assumptions above are always partially valid for some parts of the turbulence spectrum in the edge, it is certainly not the entire description and could lead to significant underestimates of the beam broadening they are designed to solve. The issue of beam broadening due to scattering is addressed in chapter 5.

### 2.2.1.2 Finite element and finite volume methods

The finite element and finite volume methods are very similar in that the two methods split the domain in to local approximations of the global equations. The local approximations are taken to be either a linear or a polynomial expansion of the global equation where the smaller the element, the more accurate the final solution is likely to be. The big advantage for these methods is the ability to define unstructured numerical meshes where the resolution can be increased and decreased where necessary thus reducing the overall computational cost. This is very good where the domain consists of complicated geometries.

### 2.2.1.3 Finite Difference methods

For the analysis of wave mechanics finite difference methods are not limited in the ways ray tracing codes are. Because this method directly solves Maxwell's equations it is referred to as full-wave and includes both the effects of multi scale turbulence and cross polarisation scattering within the formulation of the wave mechanics (see section 2.1.2). Furthermore full-wave methods are able to use a more complete description of the turbulence, generated by specific fusion plasma turbulence codes. The output from gyrokinetic, gyrofluid or fluid models of a tokamak edge can be used as direct input (see section 5.3.2). Full wave simulations are generally computationally expensive compared to the ray tracing methods described above and in the past have been used to look at specific problems which require a treatment using the full description of the wave mechanics. The results from these full-wave codes are often used to benchmark the ray codes with the inclusion of statistical turbulence. Two common methods are the time domain and the frequency domain methods. The frequency domain method has no time steps for which to iterate and is run as a steady state simulation usually involving a sparse matrix with tens of thousands of elements in each dimension. The method is limited to a single frequency and so is not useful for Doppler reflectometry methods needed here. The time domain method must iterate over many time steps in order to reach a steady state but can incorporate a spectrum of frequencies within a single simulation domain. Furthermore the visualisation of data in the time domain is

a more intuitive way to understand the physics making it easier to present and discuss new results.

### 2.2.2 FDTD for EMIT-3D

The algorithm for solving Maxwell's equations in EMIT-3D along with the plasma response was the work of a previous Ph.D. student and so an in depth discussion of the choice of algorithm and its stability is not included here. For more information on this the reader is directed to T. R. N. Williams "*Full-Wave Simulation of High-Frequency Electromagnetic Propagation Through Inhomogeneous Plasma*": Ph.D. thesis, University of York (2014) [79]. What follows is an overview of the method.

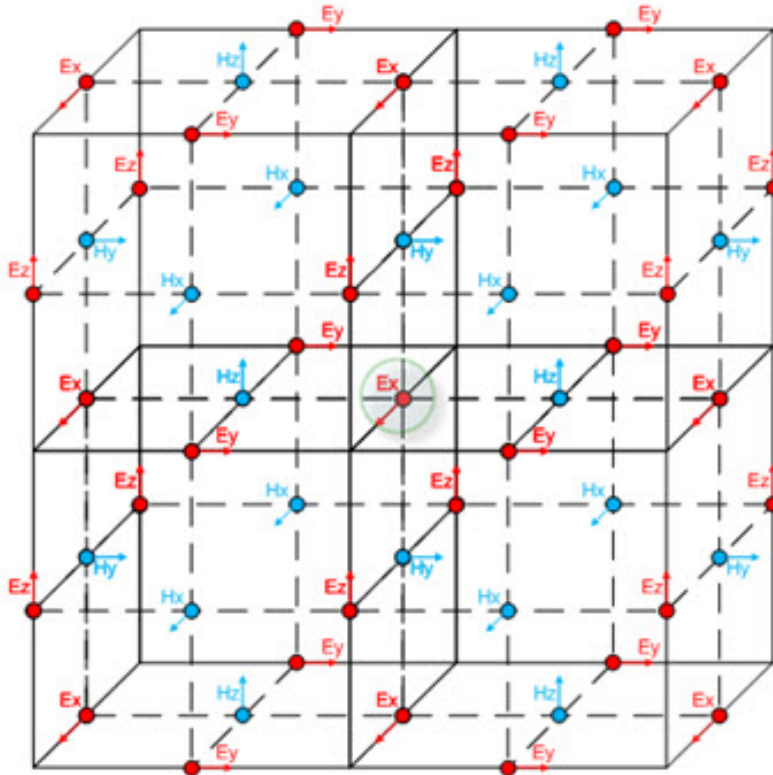


**Figure 2.5:** The Yee cell showing a single unit cell of the algorithm. The magnetic and electric field components are staggered with their locations determined by the curl operator for their individual equations. The coordinate axis is as follows:  $z$ -axis is vertical,  $y$ -axis is horizontal and  $x$ -axis is in to/out of the page. Figure taken from <https://fdtd.wikispaces.com/Indexes>.

EMIT-3D utilises the finite difference time domain (FDTD) approach to solve Maxwell's equations along with a plasma response. The algorithm for applying centred differencing to Maxwell's equations was first described in 1966 by Yee [80] and

is sometimes referred to as the Yee algorithm. The Yee algorithm has since been applied many times to a wide range of electromagnetic wave problems and has become a standard method. For this reason the finer details will not be discussed and for a more comprehensive review the reader is directed to the textbook by Taflov and Hagness [81].

The Yee algorithm is best visualised in Cartesian coordinates as a unit cell shown in figure 2.5, where the components of the waves electric and magnetic fields are staggered. The staggering of the fields is a natural consequence of the curl operators. To illustrate this statement and to aid the diagram of the Yee cell, the set of equations (2.19) and (2.20) are given which display Maxwell's equations in component form. The equation for  $E_x$  depends on the spatial derivative of  $B_z$  in the  $y$  direction and the spatial derivative of  $B_y$  in the  $x$  direction. The highlighted  $E_x$  component in figure 2.5 is shown to be surrounded by the relevant magnetic field components on the relevant axes. This can be shown to be true for all components of both Maxwell equations used in this thesis

$$\begin{aligned}\frac{\partial E_x}{\partial t} &= \frac{1}{\mu_0 \epsilon_0} \left( \frac{\partial B_z}{\partial y} - \frac{\partial B_y}{\partial z} \right) - \frac{1}{\epsilon_0} J_x \\ \frac{\partial E_y}{\partial t} &= \frac{1}{\mu_0 \epsilon_0} \left( \frac{\partial B_x}{\partial z} - \frac{\partial B_z}{\partial x} \right) - \frac{1}{\epsilon_0} J_y \\ \frac{\partial E_z}{\partial t} &= \frac{1}{\mu_0 \epsilon_0} \left( \frac{\partial B_y}{\partial x} - \frac{\partial B_x}{\partial y} \right) - \frac{1}{\epsilon_0} J_z\end{aligned}\tag{2.19}$$

$$\begin{aligned}\frac{\partial B_x}{\partial t} &= - \left( \frac{\partial E_z}{\partial y} - \frac{\partial E_y}{\partial z} \right) \\ \frac{\partial B_y}{\partial t} &= - \left( \frac{\partial E_x}{\partial z} - \frac{\partial E_z}{\partial x} \right) \\ \frac{\partial B_z}{\partial t} &= - \left( \frac{\partial E_y}{\partial x} - \frac{\partial E_x}{\partial y} \right)\end{aligned}\tag{2.20}$$

$$\begin{aligned}\frac{\partial}{\partial x} u_{i,j,k}^n &= \frac{1}{\Delta x} \left( u_{i+1/2,j,k}^n - u_{i-1/2,j,k}^n \right) + \mathcal{O} [\Delta x^2] \\ \frac{\partial}{\partial t} u_{i,j,k}^n &= \frac{1}{\Delta t} \left( u_{i,j,k}^{n+1/2} - u_{i,j,k}^{n-1/2} \right) + \mathcal{O} [\Delta x^2]\end{aligned}\tag{2.21}$$

The notation for a scalar field component at a given grid location and time will be  $u(i\Delta x, j\Delta x, k\Delta x, n\Delta t) = u|_{i,j,k}^n$  which is used in the equations for calculating centred differences shown in (2.21). The combination of the two centred difference equations for time and space results globally in a second order accurate approach.

$$\begin{aligned}
E_x|_{i+1/2,j,k}^{n+1} &= E_x|_{i+1/2,j,k}^n \\
&+ \frac{c^2\Delta t}{\Delta x} \left[ B_z|_{i+1/2,j+1/2,k}^{n+1/2} - B_z|_{i+1/2,j-1/2,k}^{n+1/2} - B_y|_{i+1/2,j,k+1/2}^{n+1/2} + B_y|_{i+1/2,j,k-1/2}^{n+1/2} \right] \\
&- \frac{\Delta t}{\epsilon_0} J_x|_{i+1/2,j,k}^{n+1} \\
E_y|_{i,j+1/2,k}^{n+1} &= E_y|_{i,j+1/2,k}^n \\
&+ \frac{c^2\Delta t}{\Delta x} \left[ B_x|_{i,j+1/2,k+1/2}^{n+1/2} - B_x|_{i,j+1/2,k-1/2}^{n+1/2} - B_z|_{i+1/2,j+1/2,k}^{n+1/2} + B_z|_{i-1/2,j+1/2,k}^{n+1/2} \right] \\
&- \frac{\Delta t}{\epsilon_0} J_y|_{i,j+1/2,k}^{n+1} \\
E_z|_{i,j,k+1/2}^{n+1} &= E_z|_{i,j,k+1/2}^n \\
&+ \frac{c^2\Delta t}{\Delta x} \left[ B_y|_{i+1/2,j,k+1/2}^{n+1/2} - B_y|_{i-1/2,j,k+1/2}^{n+1/2} - B_x|_{i,j+1/2,k+1/2}^{n+1/2} + B_x|_{i,j-1/2,k+1/2}^{n+1/2} \right] \\
&- \frac{\Delta t}{\epsilon_0} J_z|_{i,j,k+1/2}^{n+1}
\end{aligned} \tag{2.22}$$

$$\begin{aligned}
B_x|_{i,j+1/2,k+1/2}^{n+1/2} &= B_x|_{i,j+1/2,k+1/2}^{n-1/2} \\
&- \frac{\Delta t}{\Delta x} \left[ E_z|_{i,j+1,k+1/2}^n - E_z|_{i,j,k+1/2}^n - E_y|_{i,j+1/2,k+1}^n + E_y|_{i,j+1/2,k}^n \right] \\
B_y|_{i+1/2,j,k+1/2}^{n+1/2} &= B_y|_{i+1/2,j,k+1/2}^{n-1/2} \\
&- \frac{\Delta t}{\Delta x} \left[ E_x|_{i+1/2,j,k+1}^n - E_x|_{i+1/2,j,k}^n - E_z|_{i+1/2,j,k+1/2}^n + E_z|_{i,j,k+1/2}^n \right] \\
B_z|_{i+1/2,j+1/2,k}^{n+1/2} &= B_z|_{i+1/2,j+1/2,k}^{n-1/2} \\
&- \frac{\Delta t}{\Delta x} \left[ E_y|_{i+1,j+1/2,k}^n - E_y|_{i,j+1/2,k}^n - E_x|_{i+1/2,j+1,k}^n + E_x|_{i+1/2,j,k}^n \right]
\end{aligned} \tag{2.23}$$

By rearranging the time evolution equation to be in terms of the next time step we see that the next time step relies on the previous value (held in memory) and the current calculation. This has the advantage of reducing memory requirements because

one need only store a single array for the current time step in memory and then simply overwrite that array on each update. The equations for the E and B components are coupled, so in order to calculate the update on a single time step the update equations must be staggered in time, known as the leapfrog method. The update in time for B will rely on the current value of B held in memory minus the curl of E using the E values stored in memory from 1/2 time step earlier. The same method is then applied to E and is a fully explicit approach to time integration. The set of equations (2.22) and (2.23) display the computational form of Maxwells equations used in EMIT-3D. The substitution  $c^2 = 1/\mu_0\epsilon_0$  has been used and the negative signs have been multiplied through the brackets within the difference equations. Within EMIT-3D the definition of the Courant-Friedrichs-Lewy (CFL) number  $= c\Delta t/\Delta x$  is used to define the ratio of the temporal and spatial steps. The CFL condition, which will be discussed in the next chapter, defines the stability of the code and is kept at a constant value for the optimum stability of the simulation in question, in 3D  $CFL = \sqrt{3}c\Delta t/\Delta x$ .

The above equations describe an electromagnetic wave propagating through vacuum space if  $\mathbf{J}$  is set to zero. Within a dielectric medium such as a plasma there exists current sources and sinks, which manifest through the current density term  $\mathbf{J}$  in Maxwell's equations and cannot be neglected. Maxwell's equations are currently the most complete description of electromagnetism, it is therefore through the current density term that the physics model of the medium is included and assumptions begin to be made. This is discussed in the following section.

### 2.2.2.1 Inclusion of a plasma response

The momentum equation describes the physics of interest to the wave. This is given in its full form in equation (2.24) where the left hand side is the convective derivative ( $D/Dt = \partial/\partial t + (\mathbf{v} \cdot \nabla)$ ) of the fluid velocity  $\mathbf{v}$  within a fluid flow velocity  $\mathbf{v}$ . The second term on the right hand side involving  $\nu_{e,i}$  is the momentum exchange between electrons and ions (like particle collisions do not exchange the total momentum as it is averaged out over all particles of that species),  $\nabla p$  the plasma pressure gradient which exchanges momentum across a volume element by particle thermal motion. All other

terms have their usual meanings.

$$m \left( \frac{\partial \mathbf{v}}{\partial t} + (\mathbf{v} \cdot \nabla) \mathbf{v} \right) = q(\mathbf{E} + \mathbf{v} \times \mathbf{B}) - \nu_{e,i} m (\mathbf{v}_e - \mathbf{v}_i) - \frac{\nabla p}{\mathbf{n}} \quad (2.24)$$

The first simplification applied is the cold plasma model which means that the temperature term can be removed. In the previous section it was shown that all of the plasma modes except the EBW and its conversion can be captured using the cold plasma model. Within this thesis the plasma wave interactions will always be far away from EBW relevant parameters. Next the plasma is assumed to be collisionless; a low collisionality plasma is the operating regime for most current and all future tokamak plasmas. Thirdly the contribution from ions is neglected because the frequency range of waves considered within this thesis is four orders of magnitude higher than the frequency range of the ion relevant resonances and cut-off points. These first set of assumptions result in the electron fluid equation of motion shown in (2.25). The  $e$  subscripts are dropped from the vectors.

$$m_e \left( \frac{\partial \mathbf{v}}{\partial t} + (\mathbf{v} \cdot \nabla) \mathbf{v} \right) = -e(\mathbf{E} + \mathbf{v} \times \mathbf{B}) \quad (2.25)$$

In order to identify an update equation for the current density one must substitute in using its definition  $\mathbf{J} = -en\mathbf{v}$ . However, the desired update equation is for the perturbation in the current density resulting from the wave interaction therefore both of these equations must be linearised. In this way the field vectors are defined as  $\mathbf{A} = \mathbf{A}_0 + \delta\mathbf{A}_1 + \mathcal{O}(\delta^2)$ , where the subscript 0 defines an inherent plasma field and the subscript 1 is induced by the wave. The method involves taking finite centred differences to calculate the derivatives. It is noted that this was not done before for  $\mathbf{E}$  and  $\mathbf{B}$  because Maxwell's equations are by definition linear so already describe the perturbation. The justifications for the cancel to zero notation is provided after equation (2.27).

$$\mathbf{J}_0 + \delta\mathbf{J}_1 = -e(n_0\mathbf{v}_0 + \delta n_0\mathbf{v}_1 + \delta n_1\mathbf{v}_0 + \delta^2 n_1\mathbf{v}_1) \quad (2.26)$$

$$\begin{aligned}
& \frac{\partial \mathbf{v}_0}{\partial t} + \delta \frac{\partial \mathbf{v}_1}{\partial t} + \cancel{(\mathbf{v}_0 \cdot \nabla) \mathbf{v}_0} + \delta(\mathbf{v}_1 \cdot \nabla) \mathbf{v}_0 + \delta(\mathbf{v}_0 \cdot \nabla) \mathbf{v}_1 + \cancel{\delta^2(\mathbf{v}_1 \cdot \nabla) \mathbf{v}_1} = \\
& - \frac{e}{m_e} (\cancel{\mathbf{E}_0} + \delta \mathbf{E}_1 + \cancel{\mathbf{v}_0 \times \mathbf{B}_0} + \delta \mathbf{v}_1 \times \mathbf{B}_0 + \delta \mathbf{v}_0 \times \mathbf{B}_1 + \cancel{\delta^2 \mathbf{v}_1 \times \mathbf{B}_1})
\end{aligned} \tag{2.27}$$

The high orders of  $\delta^2$  in both equations are removed as negligible and all of the terms which totally involve a subscript 0 i.e.  $((\mathbf{v}_0 \cdot \nabla) \mathbf{v}_0)$  cancel each other out on the left and right hand side of the equation as the equilibrium fields. These are identified with the cancel to zero notation. It is noted that in equation (2.26), this means that the substitution definitions become  $\mathbf{J}_0 = -en_0 \mathbf{v}_0$  and  $\mathbf{J}_1 = -e(n_0 \mathbf{v}_1 + n_1 \mathbf{v}_0)$ . The background magnetic field is assumed to be slowly varying on the length scale of the wave ( $\nabla \times \mathbf{B}_0 \rightarrow 0$ ) which results in the background current density  $\mathbf{J}_0$  tending to zero because the background electric field is constant on the time scale of the wave (see equations (2.2)). The fluid flow velocity  $\mathbf{v}$  is made up of the parallel and perpendicular fluid flows. The perpendicular velocity of the fluid flows are drift velocities which are small compared to the velocity of the wave (of the order  $10 \text{ km s}^{-1}$ ) therefore the perpendicular fluid flow velocity contribution to  $\mathbf{v}_0$  is negligible. Because the thermal velocity has random direction it does not contribute to the fluid flow, and the parallel fluid flow velocity comes solely from the background current density, which as explained before is assumed to be negligible. It must be noted that in the presence of magnetic shear (non zero  $\mathbf{v}_0$  and  $\mathbf{J}_0$ ), effects on the wave mechanics should only become noticeable near a cut-off point where the group velocity becomes small and therefore comparable to the velocity of the current carrying fluid. This will be discussed further in the future work section of chapter 7. After dividing through by  $\delta$ , we now have the following equations:

$$\begin{aligned}
\mathbf{J}_1 &= -en_0 \mathbf{v}_1 \\
\frac{\partial \mathbf{v}_1}{\partial t} &= -\frac{e}{m_e} (\mathbf{E}_1 + \mathbf{v}_1 \times \mathbf{B}_0)
\end{aligned} \tag{2.28}$$

The substitution for the current density is now made by multiplying through

by  $-en_0$  which allows for the definition of the plasma frequency and the cyclotron frequency. The background magnetic field is absorbed into the cyclotron frequency leaving the unit vector resulting in the following equation.

$$\frac{\partial \mathbf{J}_1}{\partial t} = \epsilon_0 \omega_{p,e}^2 \mathbf{E}_1 - \omega_{c,e} \mathbf{J}_1 \times \hat{\mathbf{B}}_0 \quad (2.29)$$

From here the subscript 1 will again be dropped. The current density evolution equation couples the wave electric field to the plasma density through  $\omega_{pe}^2 = e^2 n_e / m_e \epsilon_0$  and the current density to the background plasma magnetic field,  $B_0$ , via  $\omega_{ce} = e B_0 / m_e$ . To get the discretised update equations we first write equation (2.29) in matrix form:

$$\dot{\mathbf{J}} = P \mathbf{J} + \epsilon_0 \omega_{p,e}^2 \mathbf{E} \quad (2.30)$$

where

$$P = \begin{pmatrix} 0 & -\hat{B}_z \omega_{c,e} & \hat{B}_y \omega_{c,e} \\ \hat{B}_z \omega_{c,e} & 0 & -\hat{B}_x \omega_{c,e} \\ -\hat{B}_y \omega_{c,e} & \hat{B}_x \omega_{c,e} & 0 \end{pmatrix} \quad (2.31)$$

The solution to this equation was described previously in [79], therefore here the solution is stated. However within this thesis the edit  $\nu = 0$  (zero collisionality) has been made:

$$\mathbf{J}|^{n+1/2} = \Theta \mathbf{J}|^{n-1/2} + \frac{\epsilon_0 \omega_{p,e}^2}{\omega_{c,e}^2 \Delta t} \Xi \mathbf{E}|^n \quad (2.32)$$

In the  $\mathbf{E}$  update equations (2.22), the  $\Delta t / \epsilon_0$  constant that is multiplying the  $\mathbf{J}$  is now multiplied through which removes the  $\epsilon_0 / \Delta t$  multiplying the  $\mathbf{E}$  in (2.32). The following definitions have been used in (2.32):

$$\Theta_{ij} = B_i B_j [1 - \cos(\Delta t \omega_{c,e})] - \epsilon_{ijk} B_k \sin(\Delta t \omega_{c,e}) + \delta_{ij} \cos(\Delta t \omega_{c,e}) \quad (2.33)$$

$$\Xi_{ij} = B_i B_j \alpha - \epsilon_{ijk} B_k \beta + \delta_{ij} \gamma \quad (2.34)$$

$$\alpha = \omega_{c,e}^2 - \omega_{c,e} \sin(\Delta t \omega_{c,e}) \quad (2.35)$$

$$\beta = \omega_{c,e} - \omega_{c,e} \cos(\Delta t \omega_{c,e}) \quad (2.36)$$

$$\gamma = \omega_{c,e} \sin(\Delta t \omega_{c,e}) \quad (2.37)$$

Here  $\epsilon_{ijk}$  is the Levi-Cevita symbol,  $\delta_{ij}$  is the Kronecker delta symbol and  $B_i$  is the vector component of the magnetic field where the magnitude is contained in  $\omega_{c,e}$ . The equation requires the electric field  $\mathbf{E}$  to have been updated and must use the previous value of  $\mathbf{J}$  which means it must be evaluated after both, on the same half time step as  $\mathbf{B}$ . Furthermore because it does not take a derivative of  $\mathbf{E}$  and uses the value from one half time step earlier it must be evaluated on the same spatial location as  $\mathbf{E}$  in the Yee cell. Therefore the following update equations can be written:

$$\begin{aligned} J_x|_{i+1/2,j,k}^{n+1/2} &= \Theta_{1,1} J_x|_{i+1/2,j,k}^{n-1/2} + \Theta_{1,2} J_y|_{i,j+1/2,k}^{n-1/2} + \Theta_{1,3} J_z|_{i,j,k+1/2}^{n-1/2} \\ &\quad + \omega_{p,e}^2 (\Xi_{1,1} E_x|_{i+1/2,j,k}^n + \Xi_{1,2} E_y|_{i,j+1/2,k}^n + \Xi_{1,3} E_z|_{i,j,k+1/2}^n) \\ J_y|_{i,j+1/2,k}^{n+1/2} &= \Theta_{2,1} J_x|_{i+1/2,j,k}^{n-1/2} + \Theta_{2,2} J_y|_{i,j+1/2,k}^{n-1/2} + \Theta_{2,3} J_z|_{i,j,k+1/2}^{n-1/2} \\ &\quad + \omega_{p,e}^2 (\Xi_{2,1} E_x|_{i+1/2,j,k}^n + \Xi_{2,2} E_y|_{i,j+1/2,k}^n + \Xi_{2,3} E_z|_{i,j,k+1/2}^n) \\ J_z|_{i,j+1/2,k}^{n+1/2} &= \Theta_{3,1} J_x|_{i+1/2,j,k}^{n-1/2} + \Theta_{3,2} J_y|_{i,j+1/2,k}^{n-1/2} + \Theta_{3,3} J_z|_{i,j,k+1/2}^{n-1/2} \\ &\quad + \omega_{p,e}^2 (\Xi_{3,1} E_x|_{i+1/2,j,k}^n + \Xi_{3,2} E_y|_{i,j+1/2,k}^n + \Xi_{3,3} E_z|_{i,j,k+1/2}^n) \end{aligned} \quad (2.38)$$



# Chapter 3

## EMIT-3D

### 3.1 Code development

The following details the work done by the author in developing EMIT-3D from the initial code that was developed by T. R. N. Williams [79].

#### 3.1.1 3D Parallelisation

The most significant modification made was to write EMIT-3D so that it was fully parallelised in all three dimensions which necessitated rewriting the entire code. The parallelisation is required to ensure that the code scales well enough to be used efficiently on large supercomputers. This first development phase was essential considering the long term goal for EMIT-3D is to perform fully 3D Doppler reflectometry simulations of SAMI that require a large number of time iterations to resolve the frequency shifts in a large spatial grid.

The computational domain of EMIT-3D is a cuboid Cartesian grid of equal grid spacing  $\Delta x$ , where the size in each dimension ( $n_x$ ,  $n_y$ ,  $n_z$ ) is set by the user in the input deck. The most obvious way to parallelise is to split the domain into a number of smaller cuboids, which are equal in number to the number of processes requested. Each cuboid is created on its allocated process and therefore only holds data for its portion of the grid. The processes communicate with adjacent processes in between each leapfrog update time-step. In this way the **B**- and **J**-fields are communicated first after their update followed by the **E**-field one half time-step later after its update:

- i. Begin time-step 1.
- ii. Update current density and magnetic field on local process.
- iii. Communicate the new current density and magnetic field values at the edge of the cuboid on the local process to adjacent processes.
- iv. Update electric field on local process.
- v. Communicate the electric field values at the edge of the cuboid on the local process to adjacent processes.
- vi. Begin time-step 2.

The communication is achieved via ghost cells of single cell thickness which surround the cuboid and do not themselves update. Each of the fields,  $\mathbf{E}$ ,  $\mathbf{B}$ ,  $\mathbf{J}$ , have three components stored in memory which all need to be communicated. Consequently, each of the 9 field arrays all have a ghost cell layer surrounding them. Information is sent from the real layer in one process to the ghost layer in the adjacent process. In this way the ghost cells act as a bridge between the adjacent process' real layers (see figure 3.1). The ghost cell itself cannot update as it is the final grid point in the array on the local process and the finite differencing scheme of the spatial derivatives requires a point on either side. The real layer therefore uses the ghost layer when it updates and information is passed seamlessly.

Within the code, OpenMPI is used as the message passing interface (MPI) which is initialised immediately as the code starts using `MPI_INIT()`. A function has been written that defines the number of processes that will be present in each direction, given the total number of processes requested. The output is then used by the function `MPI_CART_CREATE()` which creates a Cartesian grid of processes, ranked in a logical manner (`MPI_CART_RANK()`), with each process assigned a Cartesian co-ordinate (`MPI_CART_COORDS()`) with which to be referred to. In this way the physics of the domain such as the density, antenna and background field profiles can be defined on each process for its portion of the global 3D grid by referencing its own location in Cartesian coordinates. Furthermore, the `MPI_CART_RANK()` function can be used

locally to return the rank of any other process by using the co-ordinates of that process, which allows the send and receive functions to index the adjacent processes easily.

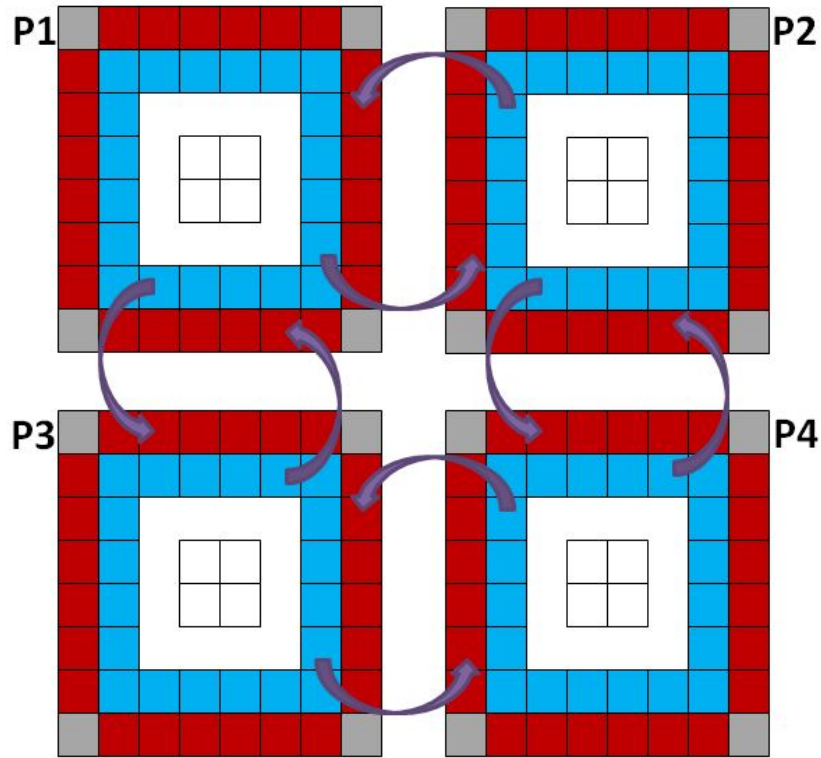


**Figure 3.1:** A 2D illustration of the transfer of data between ghost cells and the real cells. Each square denotes one memory unit of type double in the code which corresponds to one component ( $x, y, z$ ) of one of the fields ( $\mathbf{E}, \mathbf{B}, \mathbf{J}$ ) on a single grid point. The red cells are the boundary layer and the blue cells are the first real layer. The white space denotes multiple cells until the centre of the local process' grid.

### 3.1.2 Boundary conditions

The boundaries use a damping layer to reduce the wave amplitude such that the returned power is negligible, thus simulating an infinite box. A perfectly matched layer is not implemented due to the high complexity and large amount of Ph.D. time required to implement in 3D. Within the boundary layer each component of the wave electric field is multiplied by a parabolic function  $D(r)$  of the form  $D(r) = 1 + \frac{13}{T}((r - d_{\text{bound}})/d_{\text{bound}})^3$ , where  $T$  is the wave period,  $d_{\text{bound}}$  is the boundary thickness and  $r \leq d_{\text{bound}}$ . It is important to note that two types of reflections occur from the boundary layer. The dominant reflection is the one from the last physical grid point; the second more subtle reflection is a reflection from the gradient of the damping profile which is a result of the numerical stepping of the damping function.

The parabola is a function of the wavelength and the period  $T$  so then the gradient changes adaptively with the simulation parameters. If a simulation has a larger time step for a given spatial step then the wave will be travelling at a larger effective velocity through the grid. It will therefore 'see' a steeper gradient than one going at a slower effective velocity with smaller time step and will reflect more strongly off the gradient. Similarly if a low resolution spatial step is defined then the parabolic function will become less smooth with larger steps resulting in larger reflections. An adaptive boundary is therefore required. These kinds of reflections are not strongly dependant on the functional multiplication factor and so the value of 13 is arbitrary and different values are acceptable to adaptively reduce the gradient and minimise reflections from the gradient. Moreover, it was more important to choose the correct functional form which ensures a gradual fall off. A number of different functional forms are shown in figure 3.2.

The largest contribution to the total damping of the wave and its reflections from the damping function gradient is the boundary thickness. Any wave travelling through the boundary will be reflected at the last grid point and travel back through the same damping layer. In this way the damping power of a layer is doubled. Through a series of tests it was found that a boundary layer of three vacuum wavelengths consistently resulted in a relative reflected wave amplitude of less than  $10^{-4}$  (a power of less than  $10^{-8}$ ) back into the computational grid.

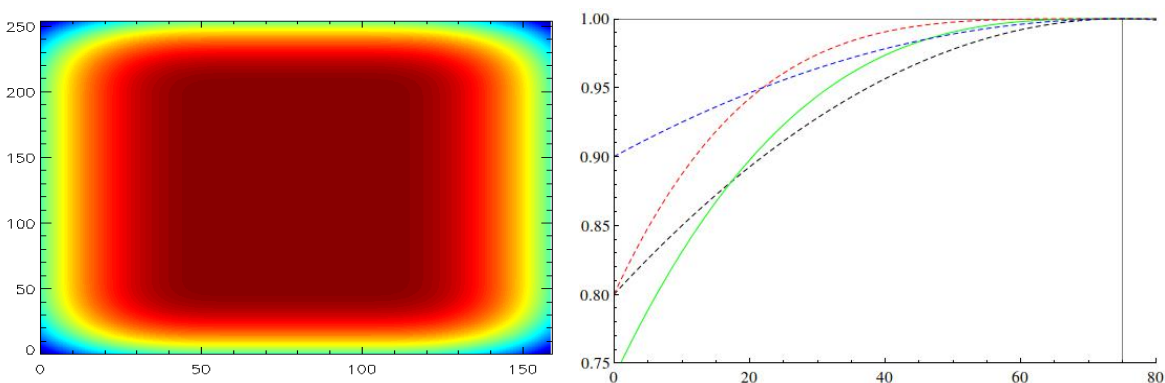


**Figure 3.2:** Left: A 2D illustration of the damping field used in the boundary layer. The field is smoothed around the corners of the domain so then there are no reflections from discontinuities at the corners. The units are in grid points as the domain size and damping layer structure is dependant on the simulation parameters. Right: Showing the functional form of the damping field in green for a 25 grid point per wavelength resolution. The dashed lines show other tested forms that were not used and the vertical line shows the boundary-domain interface.

The boundary layer function must be implemented in the code in such a way as to ensure a smooth transition between two different axes at the corners of the simulation domain. Strong reflections occur at the corners if a discontinuity is present in the damping profile which in some circumstances can lead to an instability. In order to remove this problem the damping layer grid is initialised to an array of ones instead of zeros which enables the multiply-equals operator ( $* =$ ) to be used to assign the function to each grid point. When this is done in a loop over the three co-ordinate axes then a smooth profile is obtained as shown in the left hand image of figure 3.2. The result is a reflected wave amplitude from the corners which is the same as from any other location on the boundary.

### 3.1.3 Antenna array

The antenna employs the full expression for a 3D Gaussian beam (3.1) which excites a single directional component of the wave electric field in the  $x$  direction.

$$E(r, z) = E_0 \hat{x} \frac{w_0}{w(z)} \exp \left[ -\frac{r^2}{w(z)^2} \right] \exp \left[ -i \left( kz + k \frac{r^2}{2R(z)} - \psi(z) \right) \right] \sin(\omega t) \quad (3.1)$$

$$\begin{aligned} w(z) &= w_0 \sqrt{1 + \left( \frac{z}{z_R} \right)^2} \\ R(z) &= z \left[ 1 + \left( \frac{z}{z_R} \right)^2 \right] \\ \psi(z) &= \arctan \left( \frac{z}{z_R} \right) \\ z_R &= \frac{\pi w_0^2}{\lambda} \end{aligned} \quad (3.2)$$

This expression includes a term describing the waist radius  $w_0$  which is the radius of the beam at the focal point. For a non focussed beam such as those used for ECRH in tokamaks this would be the radius of the beam as it leaves the launcher after which it will diverge. Therefore, within EMIT-3D this defines the radius of the beam at the antenna unless a focal distance  $z_0$  is defined as non zero. The radius is defined

as the distance from the centre of the beam where the amplitude falls to  $1/e$  of its peak value at the centre. This corresponds to a power factor of  $1/e^2$ . The radius at any given location along the trajectory is defined as  $w(z)$ ,  $r$  is defined as the radial distance from the centre axis and  $z$  is the axial distance from the waist.  $R(z)$  is the radius of curvature of the wave fronts and  $\psi(z)$  is the Guoy phase which is an extra phase term beyond that attributed to the phase of the light which accounts for the apparent increase in the wavelength and phase velocity near the waist. Each term is defined in the list of equations (3.2). Figure 3.3 shows an O-mode polarized beam in a homogeneous background plasma and magnetic field.

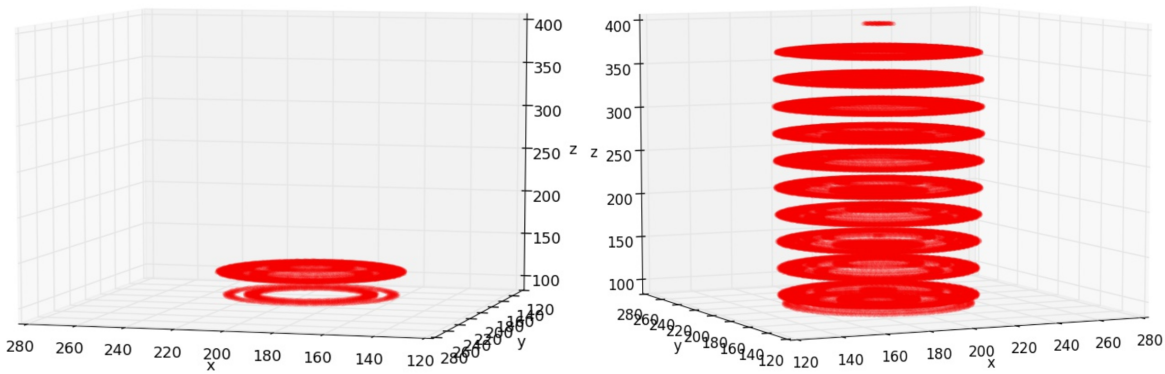


**Figure 3.3:** 3D output from EMIT-3D with the boundary layers removed showing an O-mode polarised wave in a homogeneous background plasma and magnetic field. Points of constant wave electric field are plotted resulting in disc shaped contours. The axes are in grid points because the simulation applies to any wavelength. The left image shows an early point in the simulation showing the antenna launching a Gaussian beam from  $z = 100$ . The right image shows a later point in time.

Using the full expression allows the beam to be phased across the array so that the resulting beam propagates at any angle chosen. To do this in 3D,  $r$  and  $z$  have been written in terms of their  $x$ ,  $y$  and  $z$  components in spherical polar coordinates. In this way one can define the beam  $k$  vector in terms of  $\theta$  and  $\phi$  from the  $z$ -axis. Equations (3.3) show how this is done and a phased beam can be seen later in section 3.1.5.

$$\begin{aligned}
 r^2 &= (x - x_0)^2(\sin(\phi) + \cos(\theta) \cos(\phi))^2 + (y - y_0)^2(\cos(\phi) + \cos(\theta) \sin(\phi))^2 \\
 z &= (x - x_0) \sin(\theta) \cos(\phi) + (y - y_0) \sin(\theta) \sin(\phi) + z_0
 \end{aligned}
 \tag{3.3}$$

The antenna acts as a soft-source which means it is transparent to any waves in the simulation domain which makes it ideal for reflectometry simulations. The soft

source is achieved by using the plus-equals operator ( $+ =$ ) to impose the field which adds the antenna field to the field already present without removing it. By carefully selecting the orientation of the beam propagation and the magnetic field vector, one can excite pure single polarisation modes or any specific mixture of polarisations.

### 3.1.4 NetCDF I/O and 3D visualisation routine

Network Common Data Form (NetCDF) was chosen as the format for inputting and outputting data. The format is machine independent and is widely used in the scientific community with the software libraries being readily available and usually pre-installed as a module on large computing institutions. Each process creates its own NetCDF file and writes the data for its portion of the grid to file. The user may specify which component of the wave electric field to write and select the location of a 2D slice in each of the three dimensions. The user may also write 3D information which will be discussed next. NetCDF allows each variable stored to be named arbitrarily so that it can be easily identified. Parallel NetCDF is available where each process can write to the same file so that a single coherent file is generated rather than one for each process. However, this feature is not currently used in EMIT-3D because the necessary modules are not always installed on supercomputing machines and it would make EMIT-3D less portable. When this feature does become more widespread it will be implemented.

In order to regroup the files a serial code called `RegroupNetCDF.c` is used which collects the data from each process. The user needs to state the path to the files and whether one or more simulations will be collected. If more than one simulation is to be collected then each folder must be named in numerical order  $n$ , such as `/path/to/simulations/run-n/`. The regroup routine outputs a separate NetCDF file for each write plane and for the 3D visualisation. The user is asked to specify whether to remove the boundaries, if an RMS of the electric field is to be calculated and if the total electric field is calculated from the components. If so, the total electric field is written to a separate file containing all of the planes and the RMS electric field.

The 3D visualisation routine provides qualitative information only in order to aid understanding of what the physics of the wave propagation looks like. This is

very useful for giving talks where it is difficult to explain a 3D simulation with 2D images. Moreover, this routine has proven useful in picking up behaviour that is not always seen in the 2D slices or the quantitative analysis. In a 3D grid of doubles (8 bytes) the data storage requirements become enormous. For example, in a rather small simulation with an equal 250 grid point cubic grid, a resolution of 20 grid points per wavelength resulting in 60 grid point boundaries, for 500 time-steps, the memory storage requirements would be  $370^3 \times 8 \times 500 = 202.6$  GB. Removing the boundaries and converting to floats (4 bytes) still results in 31 GB. To resolve this issue, EMIT-3D instead writes to file the integer grid point location (storing  $x$ ,  $y$  and  $z$ ) where the electric field is approximately equal to the waist radius of the beam. This is the default setting and any other electric field value can be defined. The approximation is defined as a range,  $\delta$ , that the field must lie between as it will rarely be an exact value on any grid point. In this way surfaces of iso-electric field are stored and can be plotted on a scatter plot which reproduces the wave fronts as seen previously in figure 3.3. This method stores an array of shorts (2 bytes) of the form [T, P, D] where T is the total time-steps, P is the total number of points in that time-step and D is the stored  $x$ ,  $y$  and  $z$  location. Even with 10 000 iso-electric field points in each time-step, for 2000 time-steps, the memory requirements are 0.125 GB. This value of 10 000 points per time-step has never been reached even for the largest simulations and a common value is 6000. This results in a very efficient way of storing the 3D data. All of the 3D visualisations in this thesis are produced in this way.

### 3.1.5 Benchmarking - dispersion relation

EMIT-3D has been benchmarked at numerous stages along the development process. The initial benchmarking task was to reproduce the properties of the dispersion relation for both O-mode and X-mode. A series of simulations were conducted where the homogeneous plasma density was changed in each simulation scanning from low to high density. The magnetic field was kept constant and homogeneous and orientated so that either pure O-mode or pure X-mode was present in the simulation domain depending on the scan. The scan in density was to reproduce the behaviour of the

wavelength of the wave near to a cut-off point and a resonance. The results are shown for both O-mode and X-mode in figure 3.4. The simulation was large enough for 10 vacuum wavelengths, at a resolution of 30 grid point per wavelength. The CFL number was 0.5 and the data was collected after steady state for 200 wave periods. Both the spatial resolution and time resolution are well within the theoretical region of stability resulting in high accuracy. The size of the domain and length of the simulations ensured a good ensemble average resulting in high precision. The blue dots represent the output from the simulation and the red line is the analytical expression. Excellent agreement is found for both O-mode and X-mode.

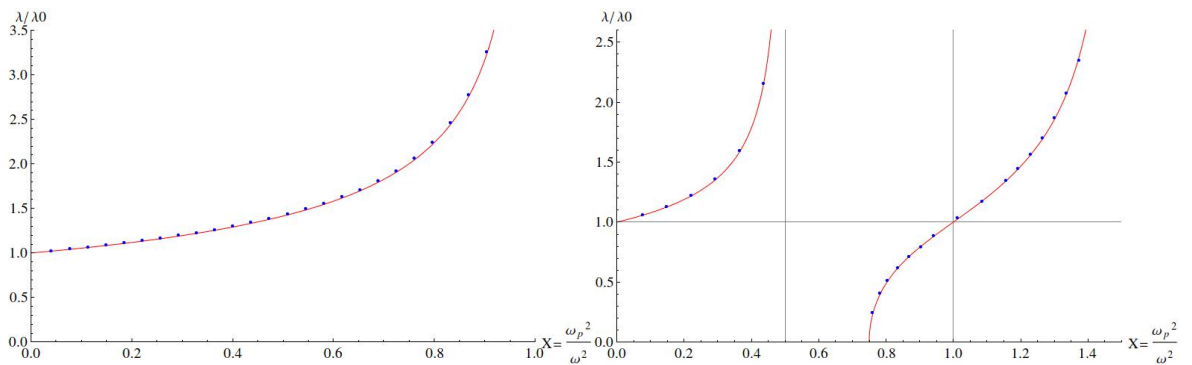


**Figure 3.4:** Relationship between the wavelength and plasma density calculated analytically using the dispersion relation (red line) and numerically from the output from EMIT-3D (blue dots). The left figure is O-mode and the right is X-mode.

Subsequently the code was then used along with a 2D full wave code IPF-FDMC which was developed at the University of Stuttgart to conduct the research in chapter 4. Excellent agreement was found between the two codes and accordingly this acts as a further benchmark of EMIT-3D. The next section will discuss the development of EMIT-3D for reflectometry use, during which further benchmarking is performed.

### 3.1.6 Scalability

EMIT-3D prints the run time of the simulation to the machine output file at the end of every simulation. During the campaign on the Helios supercomputer many simulations were conducted for the reflectometry discussed at the end of this chapter, the work in chapter 4 and a small part of chapter 5. This resulted in a large amount of run time data for a wide range of grid sizes and cores which allowed a scaling law to be

produced:

$$T = (0.7033 \times 10^{-4} + 2.45 \times 10^{-9} C^{-1.06} P^{1.07}) \times \tau \quad (3.4)$$

T is the time in minutes, C is the number of cores, P is the total number of grid points and  $\tau$  is the number of simulation time steps. The scalability for this method of parallelisation results in a near doubling of the speed when doubling the number of cores. Notable loss in this scalability trend is only encountered when a large fraction of the split cuboid is taken up by ghost cells. This occurs at a ghost cell to real cell ratio of  $> 12\%$  which can be seen in figure 3.5.

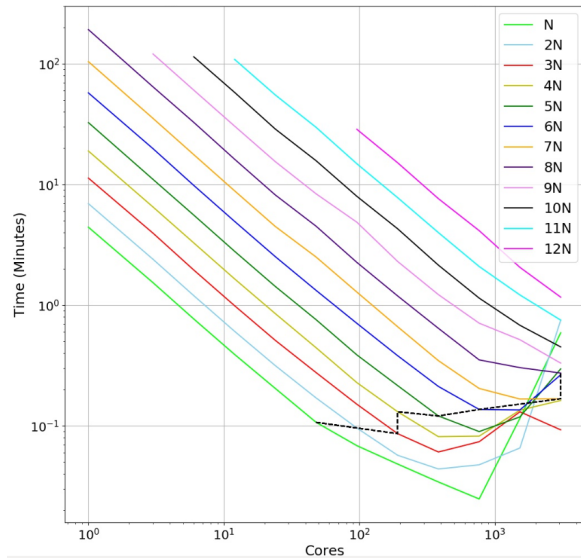


**Figure 3.5:** Scaling of EMIT-3D on the Marconi super computer. The black dashed line is when the scaling is broken and marks the point when the ratio of ghost cell to real cell reaches greater than 12%. N is the total number of grid points in run 1 which equals 512000.

## 3.2 Development for reflectometry and SAMI modelling

### 3.2.1 Density profile functions

A wave propagating up a non-turbulent electron density gradient will reflect from a flat surface where the plasma frequency is equal to the wave frequency. Within a tokamak edge region, a steep plasma gradient exists which gives rise to large plasma

density fluctuations. The plasma turbulence creates a cut-off surface which is no longer flat but rough, whose shape can be modelled as the superposition of many sinusoidal waves. The waves reflect according to the Bragg law given in (3.7). The first step towards developing EMIT-3D for reflectometry was to include analytic function for a sinusoidal corrugated density profile that would be superimposed on top of a hyperbolic tangent density gradient. Figure 3.6 shows the output from EMIT-3D showing a slice through two different corrugated density profiles. This formulation isolates the effect of a single structure by imposing a sharp step-like gradient. The options to change the amplitude and wavelength of the sinusoid appear in the input deck. The amplitude acts as a proxy for the radial correlation length whilst the wavelength corresponds to the binormal correlation length with the magnetic field homogeneous and into the page. Binormal refers to a direction perpendicular to the magnetic field vector and the radial direction. A velocity may be given to these functions in 2D by simply recalculating the function after each time step with a phase shift. By phasing the array antenna any angle of beam propagation may be chosen. In this way investigations of Doppler reflectometry may be carried out where the specific plasma properties of correlation length can be isolated and studied.

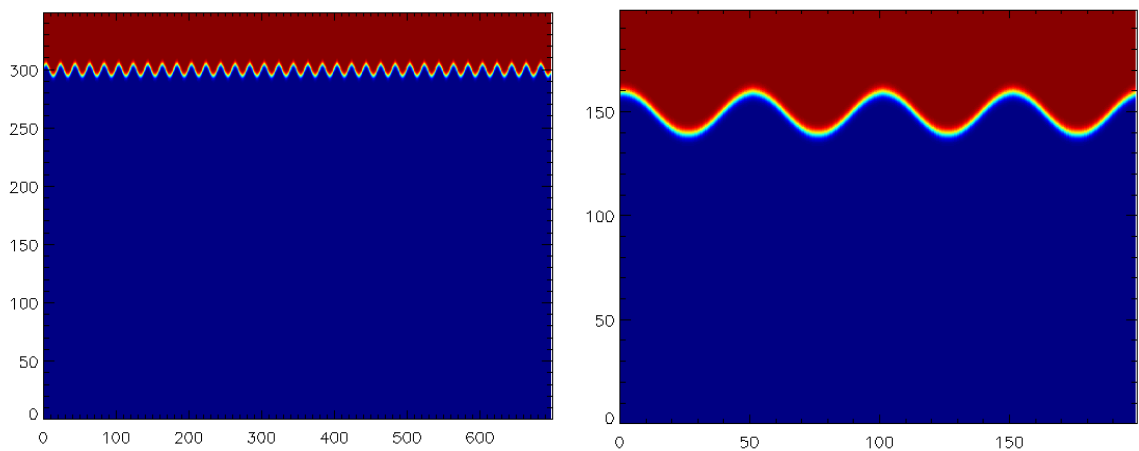


**Figure 3.6:** An analytic density function showing two different corrugated density profiles with a sharp step-like density gradient from low density (blue) to above cut-off (red). The axes are in grid points because the simulation applies to any wavelength or structure size. The axes are also arbitrary and this structure can be defined along any axis.

### 3.2.2 Interpolation for moving density

In some cases it may be necessary to model reflectometry with a more realistic density profile such as those generated from a dedicated turbulence code. For such profiles one must use an alternative method to apply a velocity to the density. The applied velocity will rarely move the density profile by exactly one grid point per time step; therefore an interpolation routine is used to transport the profile. A built in interpolation function does not exist in C programming which leaves the programmer with the option of writing their own or importing a library. In EMIT-3D an open source interpolation library called *einspline* is implemented [82]. Einspline is a C library for creating and evaluating cubic basis splines (B-splines) in 1D, 2D and 3D. In EMIT-3D only the 2D functionality is employed because the turbulence profiles are 2D in nature and simply extended along field lines into 3D. Consequently, interpolation in this direction is unnecessary. The method employed in EMIT-3D is as follows:

- i. Identify how many extra grid points of turbulence data are needed in each axis for the specified run time and velocity vector and hold these extra data points in a 2D array.
- ii. Place the next required data point in the ghost cell on the side of the domain from which the new data is moving.
- iii. Communicate the density between all adjacent processes such that the density in the final real layer of one process is in the ghost layer of the adjacent process and vice-versa.
- iv. Create the B-splines on each local process using the ghost cells as the final points.
- v. Evaluate the B-splines using the grid co-ordinates shifted by the velocity vector.
- vi. Check if the turbulence has moved by more than one grid point. If so then begin from ii. If not then begin from v.

The communication of the density profile to adjacent processes is achieved in exactly the same way as described in section 3.1.1. The density of the adjacent process'

real cell needs to be communicated to the ghost cell of the current process to ensure the B-spline is continuous across the parallelised domain.

### 3.2.3 Benchmarking - reflectometry

#### 3.2.3.1 Doppler shift from flat cut off surface

As a first test in the benchmarking phase a simple flat cut off surface normal to the beam propagation was placed in the simulation domain and was given a velocity in the same direction as the propagating beam to induce a red shift. The aim of the benchmark was to recover the velocity that was given to the moving density surface by analysing the time trace of the reflected O-mode wave electric field at the antenna plane by means of a Fourier transform. The Doppler shift is calculated by the radar Doppler shift equation:

$$f_D \approx 2 \frac{v}{c} f_{\text{probe}} \sin(\theta) \quad (3.5)$$

where  $\theta$  is the angle between the beam wavevector and the orthogonal direction to the velocity vector, in this case the normal to the cut-off surface. The frequency bin space in the Fourier spectrum is  $f_{\text{bin}} = 1/T$ , where  $T$  is the total acquisition time. Therefore, to resolve the Doppler shift to 1 bin space, one must run the simulation for  $1/f_D$  time steps. Consequently, a simulation must be run for 100 times this value to resolve to an error of 1%. It is important that high resolution is attained because if a Doppler shift lies between 2 bins with low resolution the power is spread across these bins and neither the peak amplitude nor a correct Doppler shift can be resolved. This is a result of sampling over a non integer number of wave periods known as spectral bleeding. One way to resolve the amplitude is to manually change the bin size after a simulation by taking the Fourier transform of less time steps until the peak lies exactly on a bin. This way the peak return amplitude can be extracted accurately. This vastly reduces the accuracy on the frequency so cannot be used to extract a frequency.

The first instability encountered was due to the spatial and temporal resolution

chosen which caused the electric field amplitude to go to infinity after approximately 20 000 time steps. The default parameters are 20 grid points per wavelength with a CFL condition of 0.5 which is stable for the default simulation time of less than 10 000 time steps. The CFL condition which specifies the limit of stability for the code can be seen as a proxy for the wave group velocity through the grid in a vacuum. The default value of 0.5 results in a movement of the wave front by one grid point every two time steps. The CFL condition can be thought of as a limit to how low the combined resolution can be in both time and space. Intuitively the structure of the wave can be missed by poor spatial resolution, yet if this is combined with poor time resolution then a large fraction of the wavelength moves in each time step, such that the full structure also cannot be captured in time. Therefore one must find the limit of stability of the code by altering the CFL number and the spatial resolution.

When attempting to search for acceptable stability parameters by increasing the resolution it is important to make the simulations as efficient as possible in terms of computational expense. The box size is dictated by the spatial resolution of the wave. An increase in resolution by  $n$  grid points per wavelength increases the boundary layer of 3 vacuum wavelengths by  $6n$  in each dimension. It increases the computational box by  $n\lambda/z$  in  $z$  and  $n\frac{w_0}{\lambda}\frac{w_0}{L_{box}}$  in  $x$  and  $y$  ( $w_0 =$  beam waist radius). Doubling the resolution of the grid in space can add one order of magnitude onto the run time. However, doubling the resolution in time (halving the CFL number) adds only a factor of 2 onto the run time and is therefore more favourable for maintaining stability. Through many simulations of trial and error it was found that a resolution of 25 grid points per wavelength and a CFL number of 0.2 to 0.1 ensured stability for much longer run times of between 200 000 to 1 000 000 iterations (as discovered in later simulations).

A second instability was encountered when extending the size of the computational domain in the  $z$ -axis. For the testing of large run times for larger Doppler resolution it was necessary to extend the size of the computational domain so the reflection surface, which retreated from the antenna, stayed within the computational domain. The simulation became unstable much earlier than before with the larger domain size and all other simulation parameters unchanged. The density was modelled

as a hyperbolic tangent function which stepped from a background plasma to 1.5 times the cut off density to ensure reflection. The density remained at 1.5 after the cut-off which meant that a large amount of the domain was now at high density. This instability is rather difficult to understand and after many conversations with (international) colleagues the author is still unsure of the physical explanation for the instability. The consensus however is that the solution to this instability is to reduce the total density within the simulation domain by ramping down the density to zero after the cut off and only having a density peak at  $X = 1.2$ . An example of this can be seen in figure 3.7 where the hyperbolic tangent is used to step the density down to zero in the boundaries and 1.5 vacuum wavelengths after the reflection surface. Following the correction of these two instabilities the velocity of the retreating surface was able to be recovered to any accuracy required depending on run time.

### 3.2.3.2 Doppler shift from corrugated cut off surface

As stated a large simulation time needs to be achieved for a reasonable Doppler resolution of 1%. For a turbulence velocity of the order seen in experiments  $v \approx 10 \rightarrow 50$   $\text{kms}^{-1}$  [35], at a resolution of 1% and a beam angle of  $20^\circ$ , one may calculate the necessary computation time.

$$T = 100 \times \frac{1}{2 \frac{v}{c} f_{\text{probe}} \sin(\theta)} = 877141 \times \frac{1}{f_{\text{probe}}} \quad (3.6)$$

The probing frequency is the ratio of CFL number to wave resolution which is  $0.125/25 = 0.005\Delta t^{-1}$  using the above conditions. Therefore a full simulation will be 175 million time steps. Using the equation for simulation run time scaling found in section 3.1.6 one can calculate the computational expense of the run. For 1024 cores on a small (200,200,200) grid with a boundary of 75 this yields approximately 53000 minutes which is 37 days which is not a realistic run time not only for computational expense but also for maintaining stability.

The physics of interest here is to investigate the structure of the returned Doppler shifted spectrum for which the velocity has no impact. The velocity of the turbulence

does not impact the physics other than change the Doppler shifted frequency. It is therefore irrelevant what velocity is chosen and a much larger velocity may be selected to reduce computational expense. Nonetheless, it is necessary to ensure that the velocity is not so large that relativistic effects start to impact the physics. As a quick check one can calculate the Lorentz factor ( $\gamma = 1/\sqrt{1 - v^2/c^2}$ ) of an object moving at  $v = 0.05 \sin(\theta)c$ . Here  $\gamma = 1.00031$  for a beam angle of  $\theta = 30^\circ$ , so the ratio of the change in length scales between the wave and the density structures due to Lorentz contraction is less than  $10^{-4}$  which is negligible.

For the same values as above a velocity of  $0.05c$  gives a simulation time of 467808 time steps with a run time of 141 minutes (2.35 hours). A further advantage of running with a very fast velocity is encountered when modelling Doppler reflectometry from realistic turbulence profiles produced by a turbulence code. With such a large velocity the wave will interact with a large variation of turbulence passing the reflection point during one simulation which means that the wave is sampling a large ensemble of turbulence which increases the statistical significance of the simulation. If this were not the case then many simulations of the same turbulence parameters would be needed in order to get a statistically relevant result which would be impossible with such large run times.

With the stability conditions set and the velocity of the turbulence fixed, benchmarking of the code against Bragg's law can begin. To this end a parameter scan in launched beam angle is made which reflects back from a corrugated cut-off surface with a single  $k$  corrugation as described in 3.2.1. The wavenumber  $k_{\text{turb}}$  of the corrugated density surface is changed to satisfy the Bragg condition for the particular launch angle to ensure an  $n = -1$  reflection back down the beam line. It is therefore expected that the returned  $n = -1$  power remains constant for all launch angles. The Bragg condition, first discussed in chapter 1, is given again below to aid the reader.

$$k_{\text{fluct}} = -2k_{\text{probe}} \sin(\theta) \quad (3.7)$$

The first problem encountered was a further instability issue. The hyperbolic

tangent used to step the density was too steep to be used with a sin profile for the density. This is because the sin profile as seen in figure 3.7 is in the  $y$ - $z$  plane and the tangent steps in  $z$  which means there can be sharp gradients where the sinusoid curves towards the  $z$ -axis which created an instability. This was resolved by reducing the hyperbolic tangent gradient.

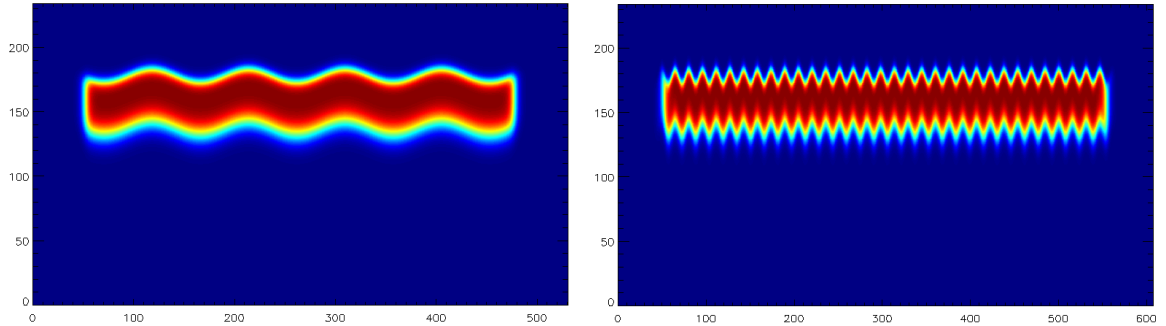


**Figure 3.7:** Density profile of a corrugated surface that satisfies the Bragg condition for two different angles of propagation. Left:  $6^\circ$ , Right:  $40^\circ$ . The velocity of the profiles is from the left to the right at  $v = 0.05c$ . The boundary layer has been included in both to show the step down of the density into the boundary to remove the instability resulting from large domain densities. The axes are in grid points because the simulation applies to any wavelength or structure size. The axes are also arbitrary and this structure can be defined along any axis.

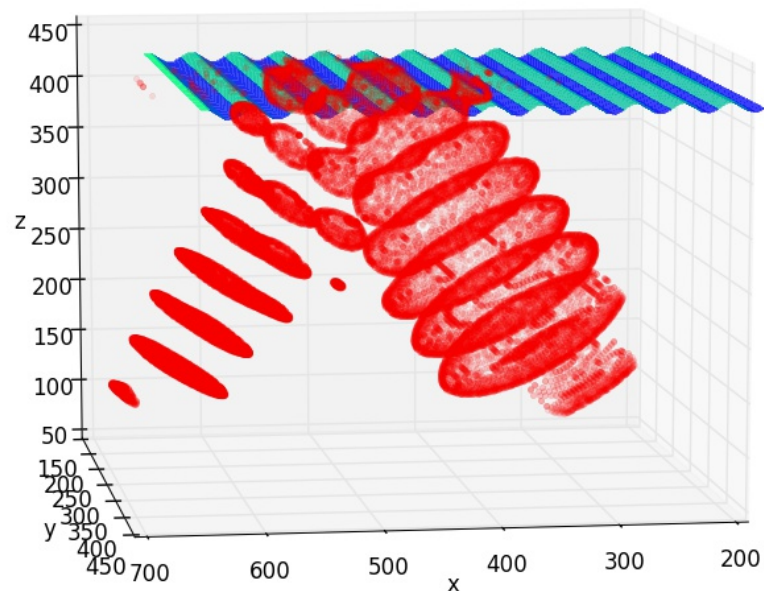


**Figure 3.8:** 3D visualisation of the Bragg reflection benchmarking scan for a particular reflection angle. The blue sinusoidal surface is located at the cut-off surface. The sinusoid is extended along the direction of the homogeneous magnetic field. The axes are in grid points because the simulation applies to any wavelength or structure size.

The Doppler shift spectrum is calculated by integrating the total signal along a line parallel to the velocity vector of the density at the radial position of the antenna plane. Figure 3.8 shows the 3D visualisation of the simulation domain for a particular propagation angle. O-mode polarisation was used for the benchmarking as in the flat surface case. The integration is taken over the antenna diameter ( $2w_0$ ) in the centre of the Gaussian beam. This means that for a small injection angle with a broad beam, the antenna should also detect the Bragg-reflected peaks from  $n = 3$  down to  $n = -4$  and not only  $n = -1$ . This is indeed what is seen and shows blue shift for  $n = 1, 2, 3$  and red shift for  $n = -1, -2, -3, -4$ . The spacing between the shifted peaks is  $nf_D$  and the power decreases as the order of reflection increases. The  $n = 0$  peak is not shifted and lies over the probing frequency as expected. Figure 3.9 shows the results of the angle scan where all peaks can be seen to lie on the expected theoretical frequency as defined by equation (3.5) ( $f_D/f_{\text{probe}} = -2 \times 0.05 \times \sin(\theta)$ ).

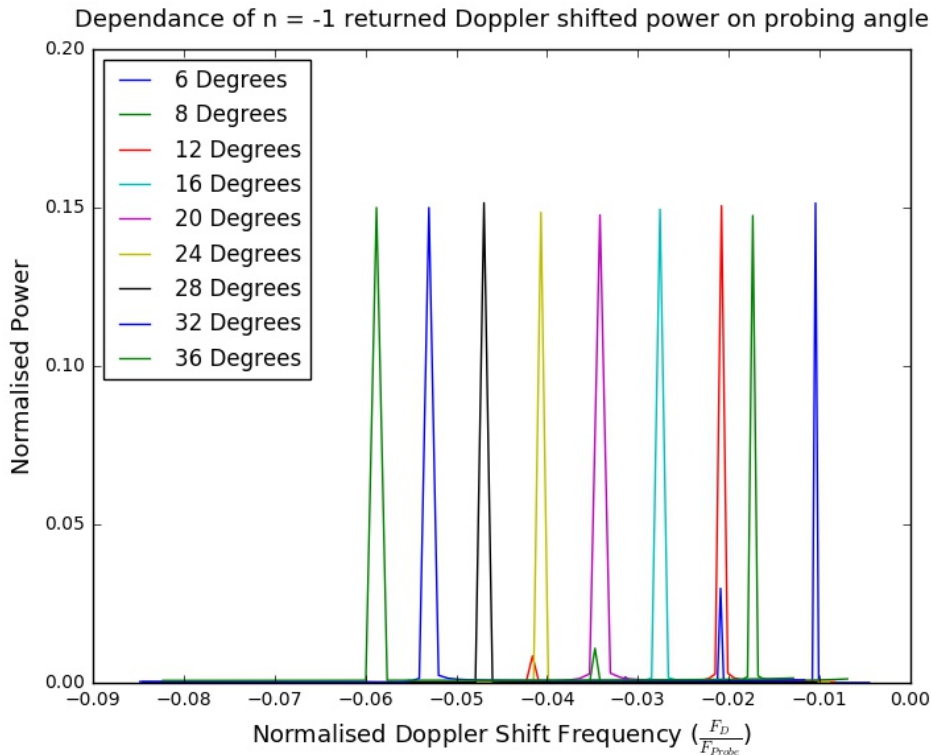


**Figure 3.9:** Measurement of  $n = -1$  reflected power from a single k corrugated density surface for a range of beam injection angles. The higher order reflections can be seen as the smaller peaks of the same colour.

The returned amplitude is constant across all angles as expected when the Bragg condition is satisfied for a hard mirror cut off. The higher order  $n = -2$  reflections

can be seen for injection angles of 6, 8 and 12 degrees and lie at their expected values. The negative Doppler shift denotes a velocity moving away from the antenna.

### 3.2.3.3 Turbulence slab Doppler reflectometry

The difference between a single corrugation to a turbulent density profile is that instead of having one wavenumber  $k_{\perp,\text{turb}}$ , the density has a spectrum of  $k_{\perp,\text{turb}}$ . This spectrum of wavenumbers will scatter the beam across a spectrum of return angles with each return angle Doppler shifted by a different amount. If all of the scattered signal were collected across all return angles then one would measure a spectrum of Doppler shifted power which would not yield a meaningful measurement of the velocity. However, it is possible to isolate one specific return angle by making a very narrow beam originating from the far field. The returned signal is now selected as the portion of the beam interacting with the  $k_{\perp,\text{turb}}$  which satisfies the Bragg condition for the beam angle, resulting in an  $n = -1$  reflection back down the beam line. All other back scattered signal from different wavenumbers will have a return angle which is away from the beam line angle and will not re-enter the antenna horn (see figure 3.10). The result is a measured Doppler spectrum with a Gaussian distribution which centres on the Doppler shifted frequency corresponding to the velocity of the turbulent layer.

The Gaussian distribution is a result of scattered power from wavenumbers very close to the wavenumber of the  $n = -1$  reflection which have an angle similar enough to the nominal  $n = -1$  return angle such that they are received back into the antenna horn. Because these different return angles create different Doppler shifts then power is seen in the frequency bins either side of the  $n = -1$  reflection. The power returned back into the antenna horn from these angles away from the  $n = -1$  nominal angle falls off as the angle becomes more distant to the nominal angle, resulting in the Gaussian shape. Further Gaussian broadening of the Doppler signal occurs as a result of the divergence of the beam. The beam will diverge and have a range of  $k$  vectors interacting with the cut-off surface at slightly different angles which again correspond to different Doppler shifts when re-entering the antenna horn. The result of this benchmark and the simulation domain can be seen in figure 3.10.

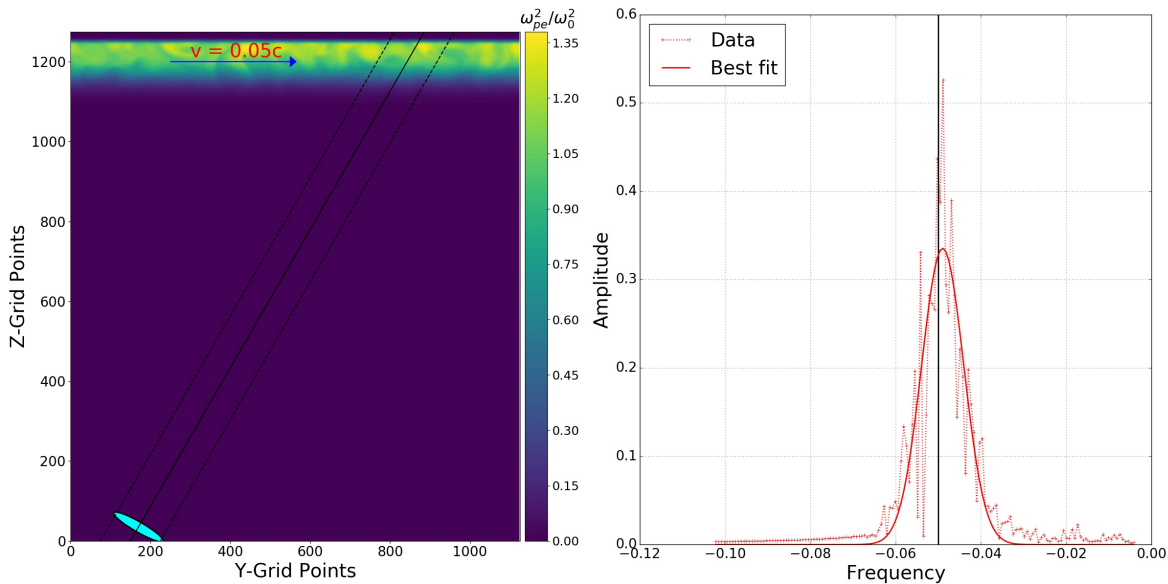


**Figure 3.10:** Left: A 2D slice of the simulation domain which shows the turbulence slab and its velocity vector along with the angle of the injected microwave beam at  $30^\circ$ . The magnetic field is into the page along which the turbulence is extended. The boundary layer has been removed. Right: The Doppler shifted spectrum detected by integrating across the beam width at the antenna plane. The Gaussian shape of the spectrum peaks at the Doppler shifted frequency corresponding to the slab velocity, marked with the vertical black line.

The turbulence used was Hasegawa-Wakatani pressure-driven drift wave turbulence which was modelled using the BOUT++ framework. A description of this model is provided in chapter 4 section 4.2. An O-mode wave was excited at an angle of  $30^\circ$  and a hyperbolic tangent was used to provide a background density gradient beginning five vacuum wavelengths from the cut-off surface. The Doppler shift is calculated as before, by integrating across the beam width at the antenna plane. The Gaussian shape of the Doppler shift can be seen to peak on the location of the normalised Doppler shift for a velocity of  $v = 0.05c$ .

### 3.2.4 Broad beam Doppler reflectometry in turbulence slab

The synthetic beam which is formed by SAMI to focus on specific locations in the plasma within the post processing analysis is broad compared with the distance to the reflection surface. This is because SAMI has only eight antennas in its current design (see chapter 1 section 1.4). To understand the data from SAMI it is necessary to understand the effect of a broad beam in Doppler reflectometry. To this end four simulations were carried out at different launch angles with the same simulation pa-

rameters as in the benchmarking section 3.2.3.3 but with the beam ten times closer to the turbulent layer. This increases the effective beam diameter in comparison to the distance to the cut-off surface without having to increase the beam waist radius in the previous simulation parameters. Increasing the waist radius by ten times in the previous simulation domain would have resulted in an increase in the box dimensions by the same amount in both  $x$  and  $y$ , which as discussed previously, would significantly increase the computational expense. The physics of interest is the ratio between the beam diameter and the distance to the cut-off surface. By bringing the surface closer instead, the divergence of the narrow beam is kept small as it would be for a beam with a larger waist radius propagating over a larger distance. The results are shown in figure 3.11.

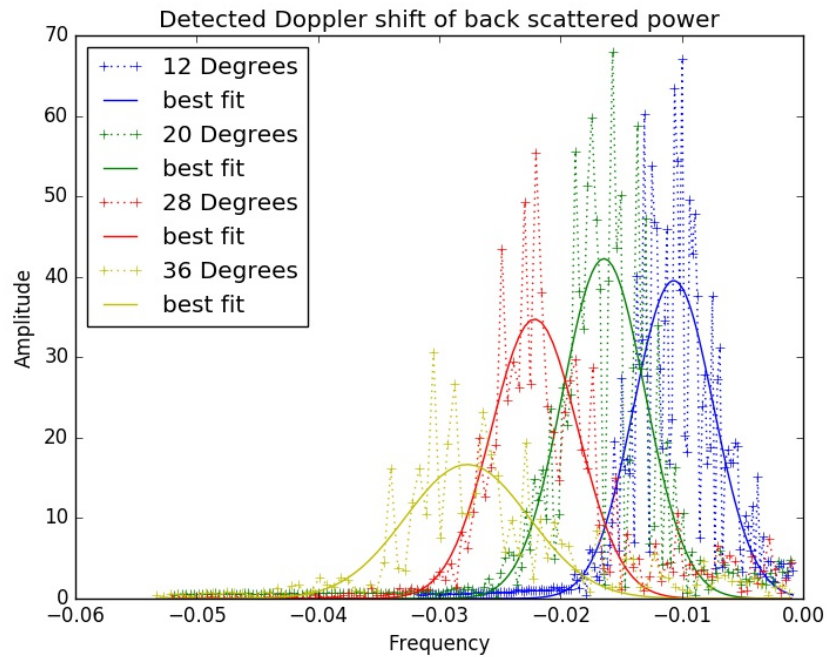


**Figure 3.11:** The Doppler shifted spectrum calculated by taking the Fourier spectrum of the total integrated power across the beam diameter at the antenna plane. The probing beam frequency would peak at zero and is subtracted. The best fit to the data is a Gaussian distribution which is plotted over the raw data.

The returned power is found to be constant at small angles and then falls off as the incident angle of the beam is increased. This is explained by noting that the power spectrum of the turbulence wavenumber is constant before falling off sharply after the knee point, towards larger values of  $k_{\text{turb}}$ . As the angle of the beam is increased the Bragg condition is satisfied by increasingly smaller turbulence correlation lengths

(larger  $k_{\text{turb}}$ ) as can be seen in figure 3.7. This means that at larger angles the  $k_{\text{turb}}$  necessary to satisfy the Bragg condition for  $n = -1$  reflection is less dominant and will therefore backscatter less power.

The Gaussian peaks are no longer centred on the Doppler shifted frequency corresponding to the velocity of the turbulence slab and are instead peaked at approximately one half of the correct frequency. To understand the cause, the problem is reduced in complexity by looking at the case of a density profile with two different  $k_{\perp,\text{turb}}$ ;  $k_{1,\perp,\text{turb}}$  and  $k_{2,\perp,\text{turb}}$ . The wave launch angle  $\theta_1$  is set to  $30^\circ$  and  $k_{1\perp}$  is set to satisfy the Bragg condition (for  $\theta_1 = 30^\circ \rightarrow k_{1\perp} = k_{\text{probe}}$ ) such that the reflection angle  $\theta_2 = \theta_1$  for a  $n = -1$  reflection down the beam line. However, now there is a second density corrugation  $k_{2,\perp,\text{turb}}$  which does not satisfy the Bragg condition and will have a different return angle  $\theta_2$  for the  $n = -1$  reflection which will not come back down the beam line. In order to find the angle of this part of the returned beam  $\theta_2$  and its respective Doppler shift, modified equations (3.8) and (3.9) must be used.

$$k_{\text{fluct}} = -k_{\text{probe}}(\sin(\theta_1) + \sin(\theta_2)) \quad (3.8)$$

$$\frac{f_{\text{D}}}{f_{\text{probe}}} \approx \frac{v}{c}(\sin(\theta_1) + \sin(\theta_2)) \quad (3.9)$$

Using this we can now tabulate what the returned beam angle is from the second corrugation and what its expected Doppler shift will be for a range of different  $k_{2,\perp,\text{turb}}$ .

$k_{2\perp}/k_{\text{probe}}$	1.5	1.3	1.2	1.1	0.9	0.8	0.7	0.5
$\theta_2$	90.00	53.13	44.43	36.87	23.58	17.46	11.54	0
$f_{\text{D}}/f_{\text{probe}}$	-0.075	-0.065	-0.060	-0.055	-0.045	-0.040	-0.035	-0.030

**Table 3.1:** The calculated back scattered angle and associated Doppler shift for different values of  $k_{2,\perp,\text{turb}}$  given a fixed launch angle.

To test the hypothesis in the broad beam regime, four simulations were conducted

with double corrugations, keeping  $k_{1,\perp,\text{turb}} = k_{\text{probe}}$  and using the values of  $k_{2,\perp,\text{turb}}$  from  $0.8 \rightarrow 1.2k_{\text{probe}}$ . The domain and beam parameters were identical to the broad beam turbulence case above. It was expected that in each simulation the antenna would pick up two  $n = -1$  large peaks (plus smaller peaks from higher order reflections for both corrugations). The peak from the nominal reflection off  $k_{1,\perp,\text{turb}}$ , satisfying the Bragg condition, would consistently lie on the expected Doppler shift. The peak from the secondary reflection off  $k_{2,\perp,\text{turb}}$ , not satisfying the Bragg condition, would lie on the Doppler shift as tabulated in table 3.1.

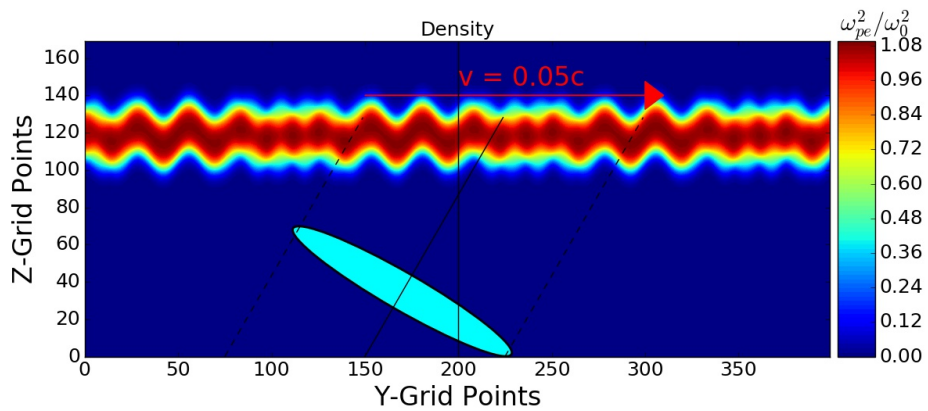


**Figure 3.12:** The density profile for the  $k_{2,\perp,\text{turb}} = 0.8k_{\text{probe}}$  simulation.

Smaller  $k_{\perp,\text{turb}}$  corresponds to larger structure sizes, which scatter a large portion of the beam power towards the right side of the antenna with a small  $\theta_2$ , resulting in a smaller Doppler shift as seen in table 3.1 and figure 3.13. The opposite is true for larger  $k_{\perp,\text{turb}}$ . The returned power is also larger for the smaller  $k_{\perp,\text{turb}}$  at lower Doppler shifted frequency. This is key to understanding figure 3.11 which peaks at Doppler shifted values much smaller than expected. It is now clear that if the density profile is a continuous turbulence spectrum and not discrete values of  $k_{\perp,\text{turb}}$ , then a continuous spectrum of Doppler shifted frequency is expected. If the launching antenna is narrow and in the far field then the dominant signal detected will be the returned signal down the beam line ( $n = -1$  reflection). However, if the beam is broad then the scattered signal from a large range of the  $k_{\perp,\text{turb}}$  not satisfying the Bragg condition will also be detected. Because the scattered power is stronger for the large structure sizes, resulting in a smaller Doppler shift, then the resulting integrated Doppler spectrum

will be swamped by Doppler shifted power at low frequencies and thus not return the correct expected Doppler shift for the launch angle and instead be shifted to peak at a lower frequency.

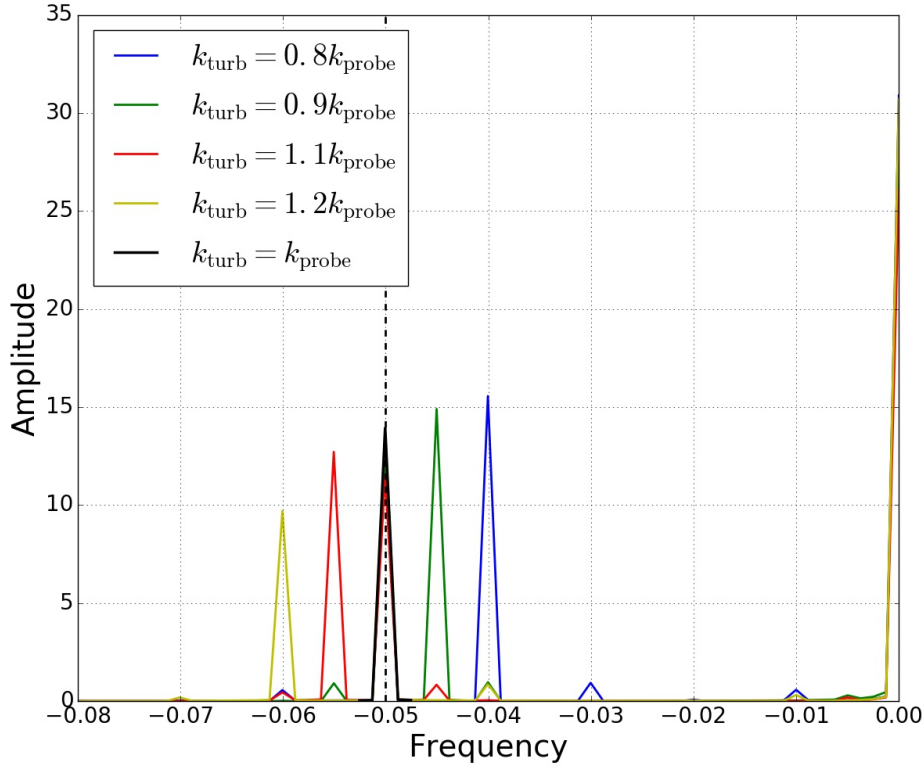


**Figure 3.13:** Measurement of  $n = -1$  reflected power from a density surface with two different corrugation wavenumbers  $k_{1,\perp,\text{turb}}$  and  $k_{2,\perp,\text{turb}}$ . The launch angle and  $k_{1,\perp,\text{turb}}$  is held constant for all four simulations resulting in the black peak at the expected normalised Doppler shift frequency. The coloured peaks are the reflections from the four simulations of different  $k_{2,\perp,\text{turb}}$ , scanning from  $0.8 \rightarrow 1.2k_{\text{probe}}$ .

As a final test that this hypothesis is truly representative of the turbulence case, figure 3.14 returns to the turbulence case of the blue Gaussian in figure 3.11 and shows the Fourier spectrum taken at four different locations across the antenna. For clarity, figure 3.11 is the total integrated signal across the entire antenna aperture. One can see that the power increases and the Doppler shifted frequency decreases as one moves from the left to the right side of the antenna. This corresponds to larger power reflection contributions from smaller  $k_{\perp,\text{turb}}$  resulting in smaller  $\theta_2$  in agreement with the hypothesis.

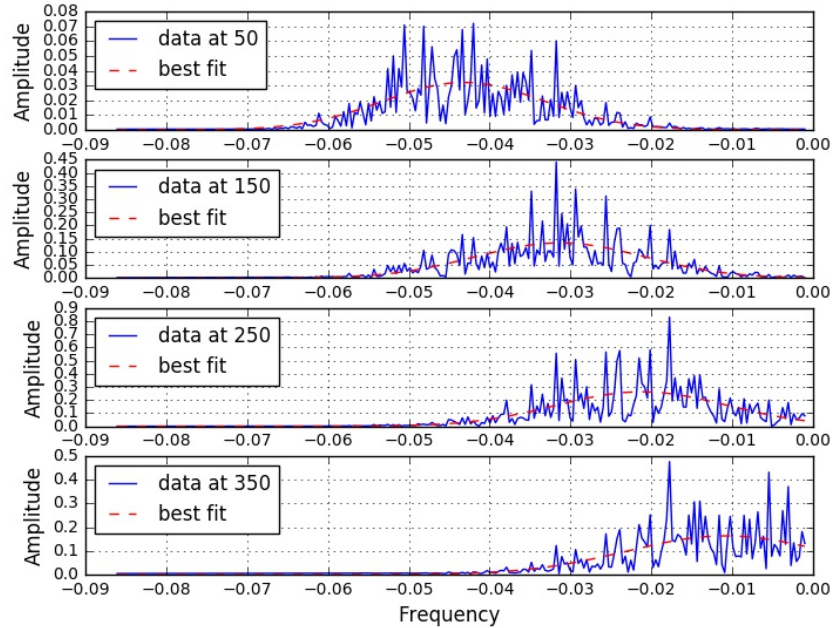


**Figure 3.14:** The Fourier spectrum of the simulation time series at four different locations across the antenna aperture. The locations in the legend are defined as number of grid points in from the edge of the antenna aperture beginning from the furthest left side of the antenna near the boundary. The grid point of the centre of the antenna would be at 200 and is 300 grid points in diameter. One can see that the power increases as one moves to the right side of the antenna and also the Doppler shifted frequency reduces which is in agreement to with the hypothesis.

### 3.2.5 Modelling the SAMI diagnostic on MAST-U and NSTX-U in 3D curved tokamak geometries

To model the Doppler reflectometry capabilities of SAMI on either MAST or NSTX-U requires a very large grid domain compared to the previous simulations. This is due to the large distance between the antenna and the cut-off surface relative to the small  $< 3$  cm wavelength ( $10 \rightarrow 34.5$  GHz) of the active probing signal and the large viewing angle of  $\pm 40^\circ$ . It was shown in the previous sections that stability is reached for a minimum of 25 grid points per wavelength with a CFL number of 0.1. In the MAST geometry shown in figure 3.15 the upper viewing angle is reduced to  $17^\circ$  due to the obstruction from the poloidal field coil and the lower angle to  $35^\circ$  due to the angle of the density profile to the beam at the bottom of the tokamak. The latter is the result of being located 20 cm above the mid plane.

A first estimate from the figure of the domain size for a Cartesian box at a fre-

frequency of 10 GHz ( $\Delta x = 1.199$  mm) would be [840, 840, 840] grid points plus boundary layers. In the previous experimental work with SAMI on MAST by D. Thomas *et al.* [61] the frequency range used was 14  $\rightarrow$  17 GHz which results in a domain size of a 1170  $\rightarrow$  1420 cube plus boundaries which is far too large to simulate repeatedly. The focus of this modelling work is to provide experimental support in order to aid understanding of the received signal which will require many simulations. Therefore, the simulation domain must be reduced.

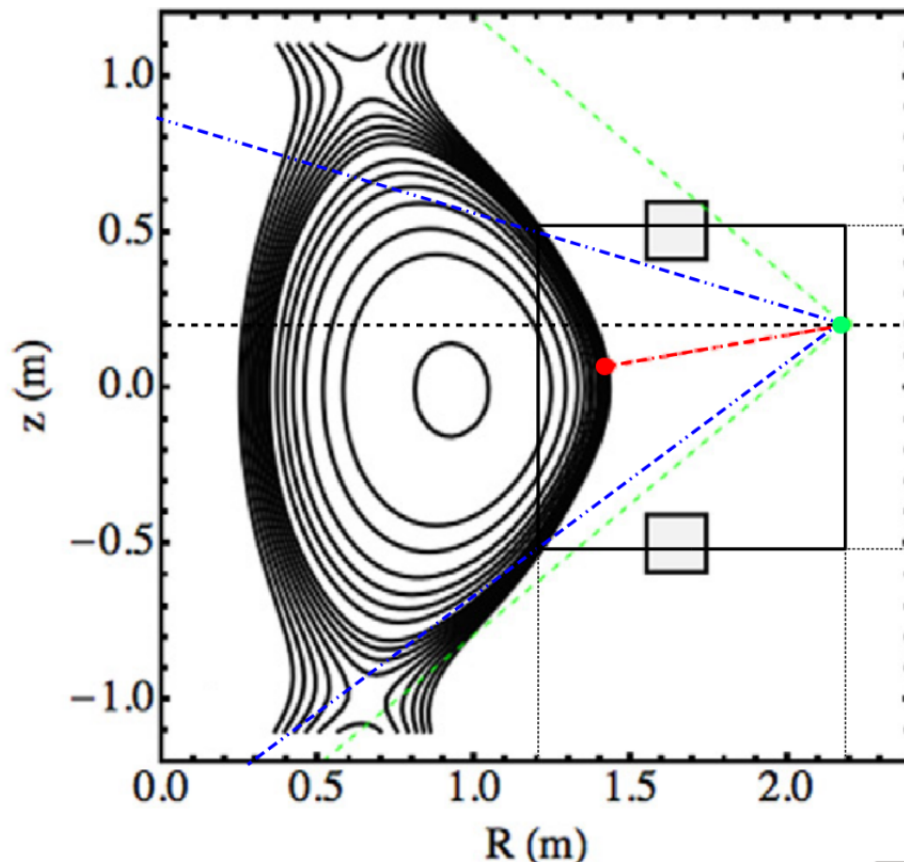


**Figure 3.15:** The poloidal view of SAMI on the MAST tokamak. The green lines depict the viewing angle range of SAMI of  $\pm 40^\circ$  from the horizontal black dashed line. SAMI is located 20 cm above the mid-plane; consequently a poloidal field coil (upper and lower small square boxes) can be seen to block the upper view of SAMI reducing the upper view angle to  $17^\circ$ . The Blue lines depict the viewing angle from which useful data is received and the red line is the shortest distance to the plasma cut-off surface. The blue lines are coincidentally equidistant about the red line at an angle of  $\pm 26^\circ$ . The black box is the simulation domain if a Cartesian box were used instead of a cone shaped domain.

Reducing the box size in this case is non trivial. Due to the nature of Doppler reflectometry a spectrum of frequencies is returned from the cut-off surface. For this reason one may not simply use ray tracing methods to propagate from the antenna to the plasma to reduce the domain size. Therefore, even though a large portion of the

box is vacuum, full-wave is still required. The geometry in figure 3.15 shows that a Cartesian box is an inefficient method for this calculation as a large portion of grid points behind the cut-off surface and above and below the antenna are unnecessary. By modelling a cone shaped simulation domain one may reduce the number of grid points by  $1/3$ . A further reduction is found by removing the grid points behind the cut-off surface, which would be dependant on the poloidal and toroidal curvature of the surface. Furthermore, it may not be necessary to model the full angular range of the SAMI diagnostic particularly in the direction parallel to the field line where the density is elongated resulting in zero back scatter. These reductions and the method for producing the unconventional simulation domain will be considered in the next sections.

### 3.2.5.1 Non-isotropic and non-homogeneous plasma profiles

In EMIT-3D significant speed up of the code is employed when the background magnetic field is defined to be homogeneous. This is an assumption commonly made when the propagation distance is small such that the magnetic field does not change significantly over the simulation domain. This is not the case for modelling SAMI. As shown in chapter 2 section 2.2.2.1 the background magnetic field couples to the wave through the plasma current density update equation via two  $3 \times 3$  matrices resulting in 18 components. If the plasma is homogeneous then only 18 components need to be defined for the whole grid; however an inhomogeneous magnetic field means that these 18 components will be different on each grid point, requiring  $18 \times n_x \times n_y \times n_z$  blocks in memory. This significant increase in the memory requirement slows down the memory access for the magnetic field and reduces the speed. A reduction in speed by a factor of 2 is found by employing a non-homogeneous magnetic field.

The magnetic field implemented in EMIT-3D for the SAMI simulations is provided by EFIT for the specific shot in question. This way the modelling ensures that the magnetic field is as accurate as is possible for direct comparison with the experimental data received by SAMI for a particular shot. Furthermore the EFIT magnetic field provides the curvature of the density and therefore the cut-off surface resulting in

a geometry which is accurate to within the errors of EFIT. By ensuring the modelled geometry and magnetic field profile is identical within errors to the experiment one can isolate the density effects on the data.

A *Mathematica* notebook receives the EFIT information directly from MAST and creates a NetCDF file which is then read by EMIT-3D. The data begins at the antenna location and is stepped in Cartesian coordinates spaced in  $\Delta x$  where  $\Delta x$  is provided by the probing frequency chosen. In this way the grid points of the Cartesian magnetic field grid overlay directly with the simulation grid spacing. The Thomson diagnostic provides a location for the steep density gradient region so that the curvature of the magnetic field at the cut-off surface can be modelled by a function both poloidally and toroidally from the EFIT data. The function returns a radial distance to the cut-off surface from the centre of the antenna.

Within EMIT-3D the curvature function calculated by *Mathematica* is currently hard coded in though in future this will be moved to the input deck. This function is needed to define the cone shaped simulation domain along with the 3D parallelisation of the new domain shape. This is discussed in the next section. After the Domain and parallelisation is constructed, the 18 components of the two matrices are calculated at each grid point using the magnetic field vector on that grid point. The Thomson diagnostic can provide a 1D time averaged density gradient profile at the mid-plane for the shot in question, which is assumed to be constant along the curvature within the SAMI viewing range.

The simulation domain is now matched to the experimental plasma parameters for time averaged density profile, magnetic field profile and geometry. This isolates the effects on the data to density perturbations which can be defined as well understood analytical functions. Therefore one may be able to isolate structures in the experimental data associated with different turbulence effects.

### 3.2.5.2 Non-Cartesian parallelisation

EMIT-3D begins by defining the cone of the new simulation domain using the function provided by the *Mathematica* file. The SAMI array antenna locations are used to define an array diameter, the centre of which is defined as the origin  $[0,0,0]$  in Cartesian coordinates. One may specify the angular view to be modelled which then defines the radius of the cone at the reflection surface. From these definitions the outline of the cone shape may be defined and a boundary layer attached onto the outside.

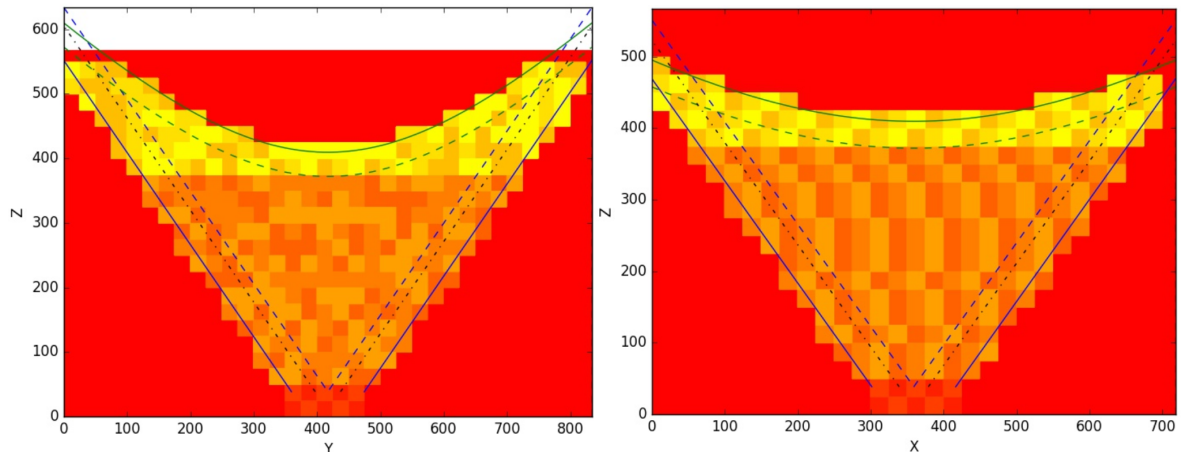


**Figure 3.16:** The cone shape of the SAMI domain in EMIT-3D. The coloured boxes within the cone are the processes. The SAMI antenna is located at the bottom surrounded by a boundary layer. The antenna diameter spans the two black dashed lines which then extend to the curved cut off surface at the defined SAMI viewing angle range. The solid blue line is the extent of the boundary layer from the edge of the SAMI view domain. The dashed blue line is the cone defined from the origin. The curved surface is defined at the top in this case is an analytic 2D quadratic used for testing which has a different form poloidally and toroidally. The solid green line is the edge of the boundary and the dashed green line is the edge of the simulation domain. The red space is the area in the Cartesian grid where no processes are defined which in this case reduces the computational expense by 45%. Left:  $y$ - $z$ -plane Right:  $x$ - $z$ -plane. The axes are in grid points because the simulation applies to any wavelength and the figure is to illustrate the splitting of the domain.

To facilitate parallelisation of the world domain, each local process remains a Cartesian box and the world grid remains defined as a Cartesian grid (with a cone inside). Processes are assigned to locations in the grid that are within the cone boundaries (see figure 3.16). By keeping this simplification, the same ghost layer technique described in this chapter (section 3.1.1) can be implemented so that the code used for the MPI only requires minimal modification. For the MPI to work, the send and receive calls need to be passed the rank of the process to which the data will be sent. Previously within a Cartesian domain this was conveniently done with the MPI func-

tion `MPI_CART_CREATE()` which assigns logical co-ordinates to each process. Any process can then pass these co-ordinates to the function `MPI_CART_RANK()` to retrieve the rank of any other process. With a cone shaped domain these MPI functions are no longer valid. Instead one must assign Cartesian co-ordinates to the processes manually along with its physical grid point location in the world grid. Furthermore, each process must hold in memory the location and rank of every other process.

To achieve this, a rank matrix is defined on every process whose size is the number of processes that would fit in each dimension in the Cartesian box in figure 3.16. The matrix is filled with  $-1$  so that the MPI interface will throw an error if it is passed this value and not simply communicate with rank 0. A for loop then loops through each dimension and assigns a rank and Cartesian co-ordinate to a processes if more than 25% of the process falls within the cone domain. The rank matrix then contains  $-1$  everywhere outside of the cone domain (in the red space in figure 3.16) and a rank number anywhere inside the cone domain. Each process can now retrieve the rank of any other process by indexing the rank matrix with the Cartesian co-ordinates. To specify if the local process is on the edge of the cone domain and therefore does not communicate information outside of the cone each process defines an array of 6 values, 1 for each face of the process box. Each process uses the rank matrix to check if any of the co-ordinates on the 6 sides of the process return a  $-1$  from the rank matrix. If this is so then the communication array stores a 0 (False) for that face to prevent communicate whereas faces that return a real rank store a 1 (True).

The boundary layer must still ensure that the damping function is smooth along the boundary of the cone to avoid any non-physical reflections of the wave as discussed in 3.1.2. The damping routine uses the definitions of the cone simulation domain to define a radius from the centre of the cone which is normalised to the radius at the edge of the simulation domain. The same damper equation is then used to define the boundaries resulting in the boundary layers shown in figure 3.17.

There was insufficient time during the Ph.D. to bring the modelling of the SAMI diagnostic to full fruition. However the work is ongoing and a brief plan of future work is laid out in section 7.3.2.

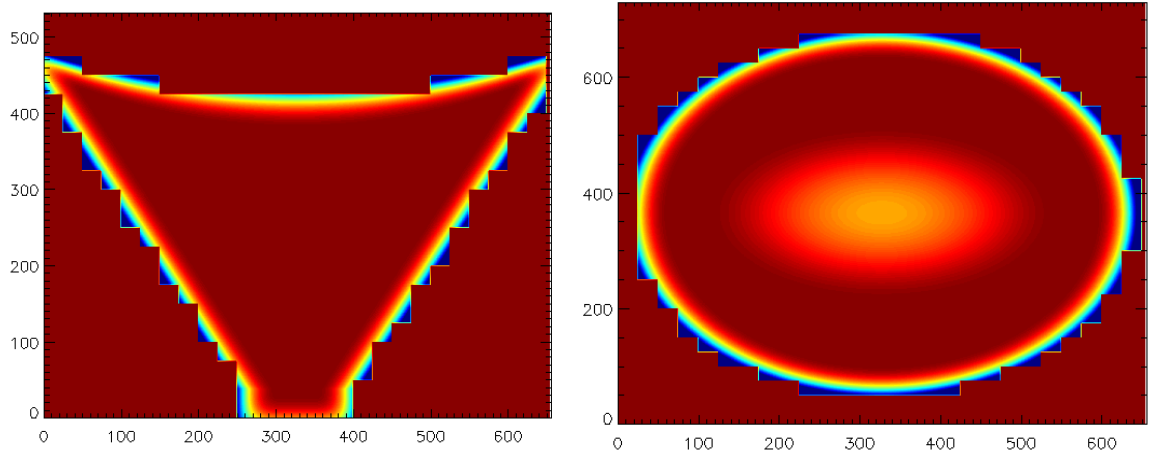


**Figure 3.17:** Output from an EMIT-3D boundary test in SAMI geometry. The red is a value of 1 and dark blue is 0. A value of 1 has been assigned outside of the cone domain so then the process parallelisation can also be seen. Left:  $x$  is horizontal and  $z$  vertical. Right:  $x$  is horizontal and  $y$  vertical. Slice taken at a  $z$  location of 410, where the centre is a result of the curvature. The axes are in grid points because the simulation applies to any wavelength and the figure is to illustrate the boundaries in the domain.



# Chapter 4

## Microwave scattering due to plasma density fluctuations

The work presented in this chapter has been previously published in:

A. Köhn, E. Holzhauser, J. Leddy, M.B. Thomas and R.G.L. Vann: *Plasma Phys. Control. Fusion* **58** 105008 (2016)

©IOP Publishing. Reproduced with permission. All rights reserved.

<http://iopscience.iop.org/article/10.1088/0741-3335/58/10/105008/meta>

A. Köhn, E. Holzhauser, J. Leddy, M.B. Thomas and R.G.L. Vann: *EPJ Web of Conferences* **147** 01001 (2017)

### 4.1 Motivation

It is commonly understood through Snell's law that an electromagnetic wave propagating obliquely through a region of changing refractive index will subsequently change path. Therefore, the cumulative effect on a beam of photons is to perturb the beam away from its original shape. By considering Snell's law in a medium of inhomogeneous refractive index the beam scattering is expected to occur most strongly when the density inhomogeneity scale length is comparable to the wavelength of the incoming beam. This scenario is the case in the edge region of the vast majority of magnetically confined fusion plasmas. Yet it is not understood what the relationship is between various plasma parameters such as density, turbulence structure size and fluctuation

level and the resultant scattering of the beam. As discussed in chapter 1, section 1.3, microwaves, which must always propagate through the turbulent edge region of the tokamak, are used to provide a wealth of information through passive and active diagnostics. Moreover, they are essential for heating, current drive and stability control where large amounts of power of the order of megawatts is injected. This necessitates precise targeting within the experiment to ensure that other instruments are not damaged by the beam and the plasma is not destabilised. Therefore, knowledge of the influence of turbulence on beam propagation through a parameter scan of the salient plasma characteristics is required. This is the purpose of this work. The work in this chapter is in units normalised to the wavelength of the wave and so any graphs which show the domain have axes in grid points. This is because the scattering is the same on any scale length and what is important is the ratio of the wavelength to the turbulence parameter. Therefore this work applies to any scale from galactic scales to ultra fine scales. The number of grid points per wavelength used in the simulations is 50.

## 4.2 Turbulence model

Considering the turbulent plasma on the time scale of the microwave, the fluctuations appear to be frozen in: the typical frequency scales are in the kHz range [53, 54, 83] whereas the microwave frequency lies in the GHz range. Moreover, due to the large frequency of the injected microwaves it is only the fluctuating electron density which plays a role as explained in chapter 2. The important parameter is the group velocity of the injected O-mode which can be expressed as  $v_g \approx c\sqrt{1-X}$ , with  $c$  the speed of light and  $X = \omega_{pe}^2/\omega_0^2$ . If the turbulent structures, i.e. the non-homogeneities in the electron density are interpreted as drift-wave structures, their phase velocity can be estimated by the electron diamagnetic drift velocity, yielding values which are typically  $< 10^4 \text{ ms}^{-1}$  [53]. Hence, even if the electron density reaches values of 99.9% of the O-mode cut-off density, the resulting group velocity of the wave is still a factor of 1000 larger than the velocity of the density structures and the assumption of a frozen plasma in the frame of the microwave is therefore justified.

The dominant cause of anomalous transport in tokamak L-mode plasmas is pressure driven drift wave turbulence [84,85]. This kind of turbulence is present everywhere in the tokamak but is most prominent in the edge where the large temperature and density gradients are. The BOUT++ framework [86] was used to generate turbulence profiles using the Hasegawa-Wakatani drift-wave turbulence model. This set of profiles can be accessed at [87] and an example is shown in figure 4.1. Hasegawa and Wakatani [88] derived a simple set of equations 4.1 which describes two variables, the electric potential  $\phi$  and the density  $n$  in a 2 fluid system. The model is 2D, assuming a homogeneous magnetic field in a zero-curvature slab geometry. Since 1984 it has been used both to simulate edge turbulence as well as to benchmark more complex models [89–91].

$$\begin{aligned} \rho_s^2 \frac{d}{dt} \nabla^2 \phi &= -D_{\parallel} \nabla_{\parallel}^2 \left( \phi - \frac{n}{n_0} \right) + \nu \nabla^2 \nabla^2 \phi \\ \frac{dn}{dt} - D_0 \nabla^2 n &= -D_{\parallel} \nabla_{\parallel}^2 \left( \phi - \frac{n_0}{n} \right) \end{aligned} \quad (4.1)$$

where  $\rho_s$  is the species Larmour radius,  $D$  is the diffusion coefficient,  $\parallel$  denotes parallel to the field line and  $\nu$  is the collisionally.

### 4.3 The simulation set-up

The simulations were conducted in 3D geometry using EMIT-3D and in 2D using IPF-FDMC. The characteristics of the normalised turbulence generated from BOUT++ are manipulated to perform parameter scans. The profiles may be multiplied to change the root mean square (RMS) fluctuation level or interpolated to change the turbulence correlation length in relation to the wavelength. In order to ensure the scattering is statistically representative of the probed turbulence it is necessary to perform many simulations using uncorrelated density profiles where the average properties of the density profiles remains the same. To this end the normalised profiles are cut into many uncorrelated slices of a fixed width of  $10\lambda_0$  and required propagation depth  $n\lambda_0$  (the default is  $d_{\text{turb}} = 3\lambda_0$ ).

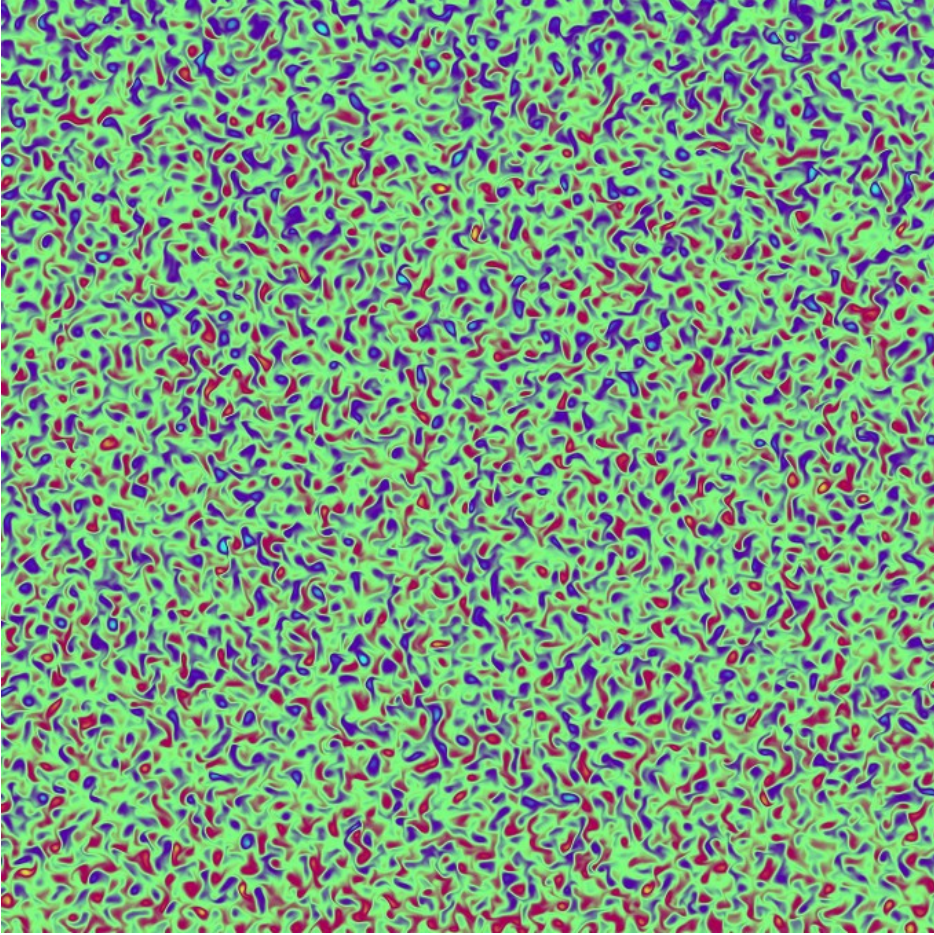


**Figure 4.1:** Contour plot of the electron plasma density generated by BOUT++. Shown is one time slice of the turbulence which evolves in time. Axes labels and dimensions are not included as the space applies to any length scales. The figure is to illustrate the 2D turbulence generated by these equations.

For the following description of the simulation domain the reader should refer to figure 4.2 which shows the 3D output from EMIT-3D for a particular set of turbulence parameters. A homogeneous background electron density  $n_0$  may be chosen onto which a layer of turbulent electron density fluctuations is superimposed (the density will henceforth be quoted in terms of the normalised plasma frequency  $X = \omega_{p,e}^2/\omega_0^2$ ). The emitting antenna, placed at the lower boundary of the grid, injects a Gaussian beam in the  $z$ -direction, perpendicular to the filamentary structures. A receiving antenna is located at the upper boundary of the grid. Both antennas extend along the whole  $x$  and  $y$  axes. The distance between both antennas and the boundary of the turbulence layer is set to one vacuum wavelength  $\lambda_0$ . The default value for the waist radius of the beam is  $w_0 = 2\lambda_0$ . Despite the relatively small beam waist, the divergence of the beam is negligible for the default size of the computational grid. The wave is launched in the

homogeneous background which is then smoothly transitioned to the turbulence layer. The same method is employed for the receiving antenna on the far side of the turbulence layer. The electron density structures are taken to be uniform along the direction of the homogeneous background magnetic field ( $B\hat{y}$ ) resembling the filamentary structures observed in experiments [53, 54]. This allows a direct comparison between the 2D simulations of IPF-FDMC with the 3D simulations of EMIT-3D which can lead to a conclusion of whether the scattering in the geometry used is inherently 2D or 3D in nature. A background magnetic field is chosen so that O-mode is the only solution to the dispersion relation for the background density in the simulation domain. With a default background density of  $X = 0.5$  the magnetic field was  $Y = \omega_{e,c}/\omega_0 = 0.5$ . This ensures the scattering observed is not a result of cross polarisation mixing but purely of the density structures.

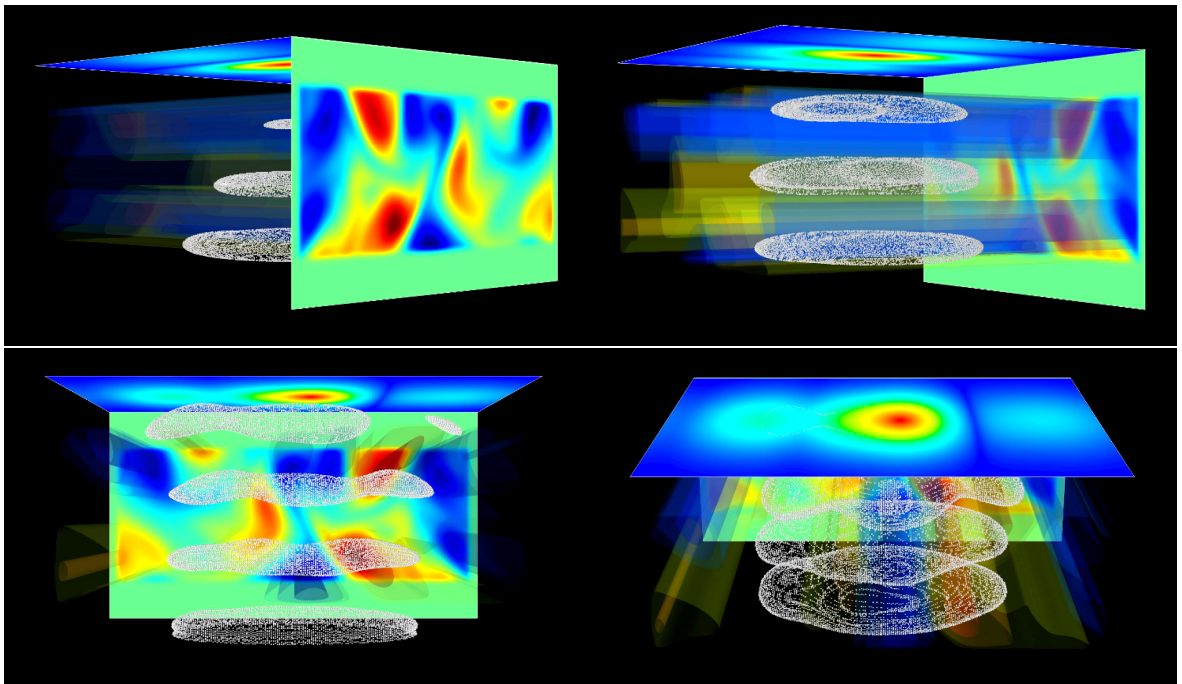


**Figure 4.2:** The figures show successive times in one simulation moving in the order top-left, top-right, bottom-left, bottom-right. The turbulence slab is of depth  $d_{\text{turb}} = 3\lambda_0$ . Homogeneous background plasma,  $n_0 = 0.5n_{\text{cut-off}}$ , on which the turbulence is superimposed extends  $1\lambda_0$  above and below for launching the beam and receiving the scattered signal. The turbulence has fluctuation level of  $\sigma = 8.75\%$  and correlation length of  $L_c = 0.5\lambda_0$ . The density profile is extended along the homogeneous magnetic field forming the filamentary structures. The white dots form surfaces of constant electric field amplitude forming the wave fronts. The 2D image at the backplane is the receiving antenna which calculates the RMS electric field taken over 2 wave periods.

## 4.4 Interpreting the data

The simulations are conducted in the time domain and so are allowed to run until a steady state signal is present at the receiving antenna. From this point in time the receiving antenna records the three spatial components of the wave electric field at every spatial point in its two dimensional  $x$ - $y$  plane. The signal is recorded for two wave periods and from this a Root Mean Square (RMS) value for the electric field over time  $t$  is found across the plane  $i, j$  (see figure 4.2). This is performed independently on each grid point  $i, j$  and so these subscripts are omitted.

$$E_{\text{rms}} = \sqrt{\frac{\sum_{t=1}^T (E_{x,t}^2 + E_{y,t}^2 + E_{z,t}^2)}{T}} \quad (4.2)$$

This two dimensional signal is found for each turbulence time slice. Figure 4.3 illustrates the effect of turbulence on the signal from a number of different slices as compared with a homogeneous case.

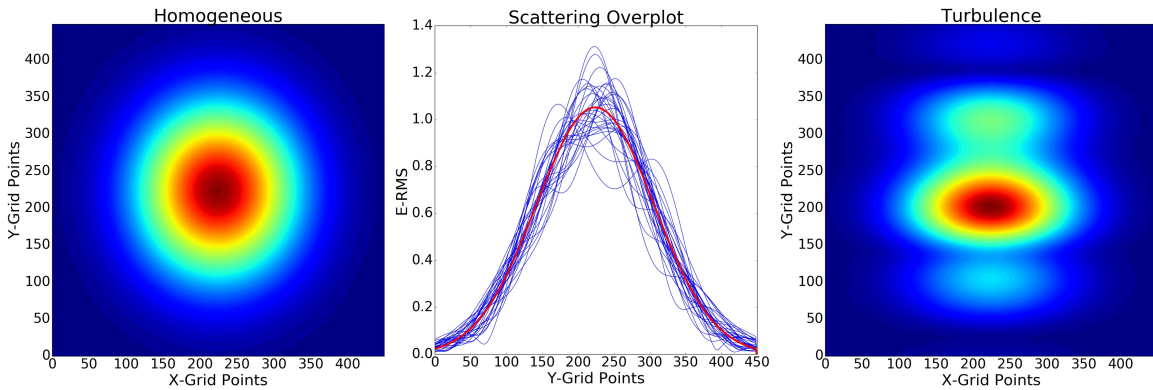


**Figure 4.3:** The image on the left shows the two dimensional RMS electric field of the wave at the receiving antenna for a beam propagating through a homogeneous plasma. The image on the right shows the RMS field for a beam propagating through a turbulent region. The middle image shows the RMS field for a cut through the centre of the beam. Homogeneous is in red and overlaid in blue is the signal from multiple turbulence slices.

In order to ensure that the calculated scattering is truly representative of the specific turbulence parameters an ensemble of slices must be simulated. The ensemble size  $N$  depends on the amount the beam is scattered. For example in the regime of low amplitude fluctuations with a fluctuation level  $\ll \lambda_0$  the turbulence tends to a homogeneous plasma as seen by the wave and a small ensemble will be needed. The

ensemble size also depends on the average spatial size of the electron density structures: if they are very small compared to the vacuum wavelength, many of them exist in one turbulence slice resulting already in a good average. When, in contrast, the spatial dimensions of the electron density structures exceed  $\lambda_0$  and only very few of them exist in one turbulence slice, a high number of samples is required. The quality of the ensemble average is controlled by determining the average position  $\tilde{x}_{\max}$  (tilde denotes perturbed due to turbulence) of the maximum in the  $\tilde{E}_{\text{rms}}$  signal in the detector antenna plane. This value is then compared with the position of the maximum signal  $x_{\max}$  for the homogeneous plasma ( $\Delta = \tilde{x}_{\max} - x_{\max}$ ). One would expect that with increasing ensemble the sum of these differences should asymptote to zero. Figure 4.4 shows the analysis where the correlation length  $L_C = 0.66(\pm 0.03)\lambda_0$ . The correlation length,  $L_C$ , is defined as the average distance over which the normalised autocorrelation falls off to a value of 0.5 which corresponds to the average eddy radius when the density amplitude falls to  $1/e$ .  $L_C$  therefore corresponds to average structure size. This particular case corresponds to both a very large scattering event whilst also containing a small number of structures along the propagation path within the domain. The combination of these two things means that a very large ensemble is necessary for these parameters.  $\Delta$  approaches zero after  $N = 2000$  but strictly asymptotes to zero towards  $N = 15000$ . This is one of the largest ensemble sizes necessary and other parameter scans conducted required much smaller ensembles.

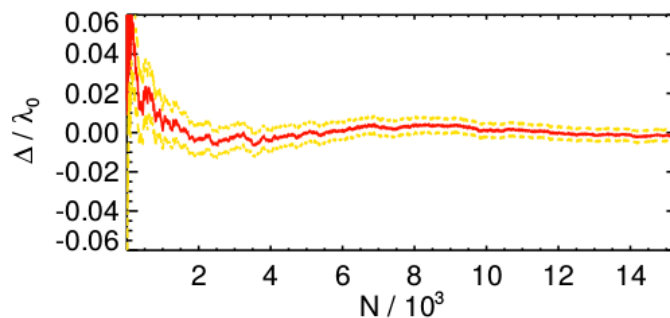


**Figure 4.4:** Average value of the spatial deviation of the maximum signal in the detector antenna plane as a function of the number of ensembles. The red central curve corresponds to the arithmetic mean and the upper and lower orange dashed curves correspond to the error given by the standard deviation of the mean. This figure has been reproduced with the kind permission of Dr Alf Köhn.

Two separate methods for describing the effect of turbulence on the beam will be

considered. The RMS electric field at the backplane for a wave propagating through homogeneous plasma forms a Gaussian with a specific width  $w_{\text{homog}}$ . One can find the mean of the RMS field of the scattered beams over the ensemble  $N$  and fit a Gaussian of width  $w_{\text{turb}}$ . In this way the two widths can be compared and a fractional beam broadening deduced. The beam width is an important parameter for the case of a localized current drive: if the beam is too large compared to the width of the magnetic island it is supposed to stabilize, its impact on it is reduced (see chapter 1, section 1.2). The drawback of this method is, however, that side lobes due to strong scattering events are not taken into account. For a time averaged beam experiencing scattering, side lobes represent power that lie outside of a Gaussian fit to the new scattered beam either side of the peak. This is explained by figure 4.5 and its accompanying discussion. The second method defines a scattering parameter  $\alpha$  (equation 4.3), which is a measure of the percentage change in the energy distribution across the receiving antenna.

$$\alpha = \sum_{i,j} \frac{(\tilde{E}_{\text{rms}} - E_{\text{rms}})^2}{E_{\text{rms}}^2} \quad (4.3)$$

Here the  $\tilde{E}_{\text{rms}}$  represents the RMS calculated from a turbulence profile and is normalised to the RMS calculated from a homogeneous profile. This compresses the result from one turbulence snapshot into a single value. A separate value of  $\alpha$  is obtained for each sample and ensemble averaging is then performed to get the scattering for one set of turbulence parameters. The strength of the fluctuations is calculated as the standard deviation of the electron density in the turbulence slice where  $N_{x,y}$  is the number of grid points in the turbulence slice.

$$\sigma = \sqrt{\frac{1}{N_{x,y}} \sum_{x,y} (\tilde{n}_e(x,y) - n_0)^2} \quad (4.4)$$

In order to assign uncertainties to the data it is important to understand how the calculation of the scatter parameter depends on ensemble size. Figure 4.5 shows that the scattering displays a log-normal distribution with increasing ensemble size which

means that the nature of the turbulence gives rise to the occurrence of random large scattering events which significantly perturb the beam.

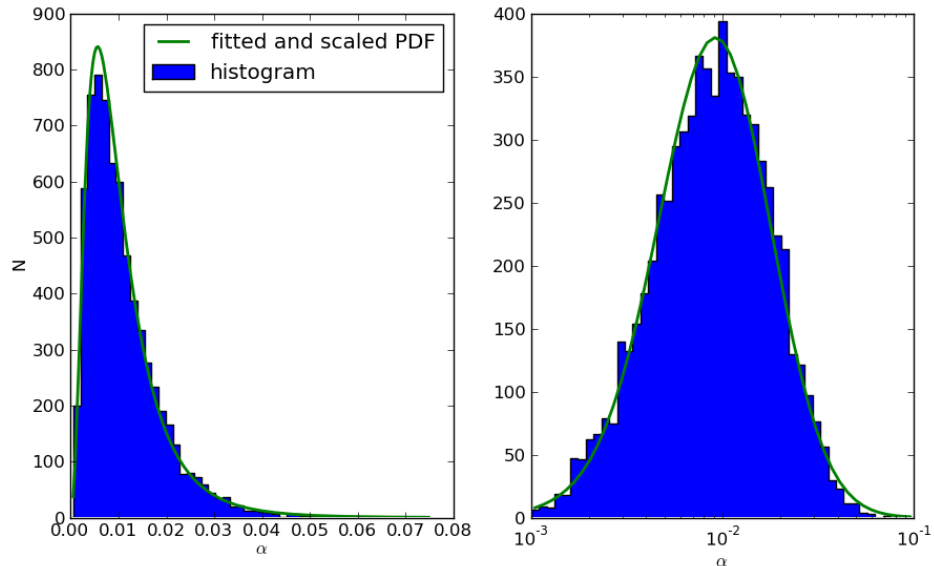


**Figure 4.5:** Histogram and fitted PDF of the scattering parameter  $\alpha$  for a size of the turbulent density structures of  $L_C \approx 0.5\lambda_0$ . The histogram follows a log-normal distribution. This figure has been reproduced with the kind permission of Dr Alf Köhn.

It is for this reason that side lobes develop. The side lobes are a direct result of the scattering from turbulent fluctuations having correlation lengths similar to the vacuum wavelength of the injected microwave and/or having a significant amplitude. This effect would not be expected in turbulence that is smoothly varying relative to the wavelength ( $L_C \ll \lambda_0$ ). In order to account for this it is the median of the scatter parameter that is taken over the ensemble size which is less sensitive to large outlying events than the mean. Consequently it is the median absolute deviation (MAD) that is defined as the uncertainty, which is then converted to a standard deviation. The MAD is converted to a standard deviation to include the sensitivity to outlying events in the uncertainty but not in the data point. For IPF-FDMC the ensemble size is so large that the effect of random large scattering events is negligible on the result and does not lead to an artificial over-estimation in the scatter parameter as it would with the low ensemble size of EMIT-3D.

## 4.5 Results

### 4.5.1 Variation of the correlation length

The average size of the electron density structures in the turbulence region is varied from  $L_C \approx 0.06\lambda_0$  to  $1.04\lambda_0$  an illustration of which can be seen in figure 4.6. The average fluctuation strength here is  $\sigma = 4.0(\pm 0.1)\%$ , the background density  $n_0 = 0.5n_{\text{cut-off}}$ , the turbulence layer is  $d_{\text{turb}} = 3\lambda_0$ , the beam width is  $w_0 = 2\lambda_0$  and the magnetic field is  $Y = 0.5$ .

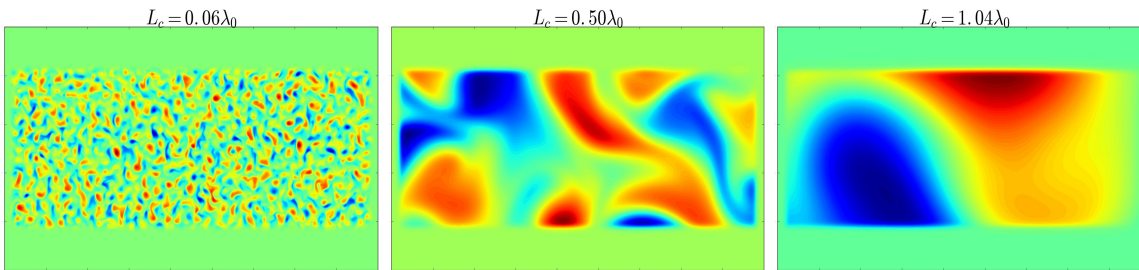


**Figure 4.6:** 2D density contour plots showing three different correlation lengths across the range in the parameter scan as they look in the simulation domain. All other plasma parameters are kept constant. The magnetic field is into the page along  $x$ , The horizontal is the  $y$ -axis and the vertical is the  $z$ -axis.

As discussed in section 4.4, the ensemble size  $N$  for IPF-FDMC is increased with increasing values of  $L_C$ . For  $L_C \approx 0.20\lambda_0$ , for example, it is  $N = 1200$ , whereas for  $L_C \approx 1.04\lambda_0$ , it is  $N = 29\,000$ . This was not possible for the 3D simulations of EMIT-3D and so the ensemble was capped at  $N = 130$ . In section 4.4 the required ensemble size was argued to be a function of both the scattering power of the turbulence and the number of structures contained within the domain. As can be seen from figure 4.7, the uncertainties on the EMIT-3D measurements increase towards the maximum scattering correlation length and decrease afterwards. This shows that the optimum ensemble size to maintain good statistics is dependant on the scattering strength of the turbulence. Furthermore for the same value in scatter parameter the uncertainties are larger for large values of  $L_C$  than small values. This demonstrates the dependence of the required ensemble size to the number of structures contained within the domain.

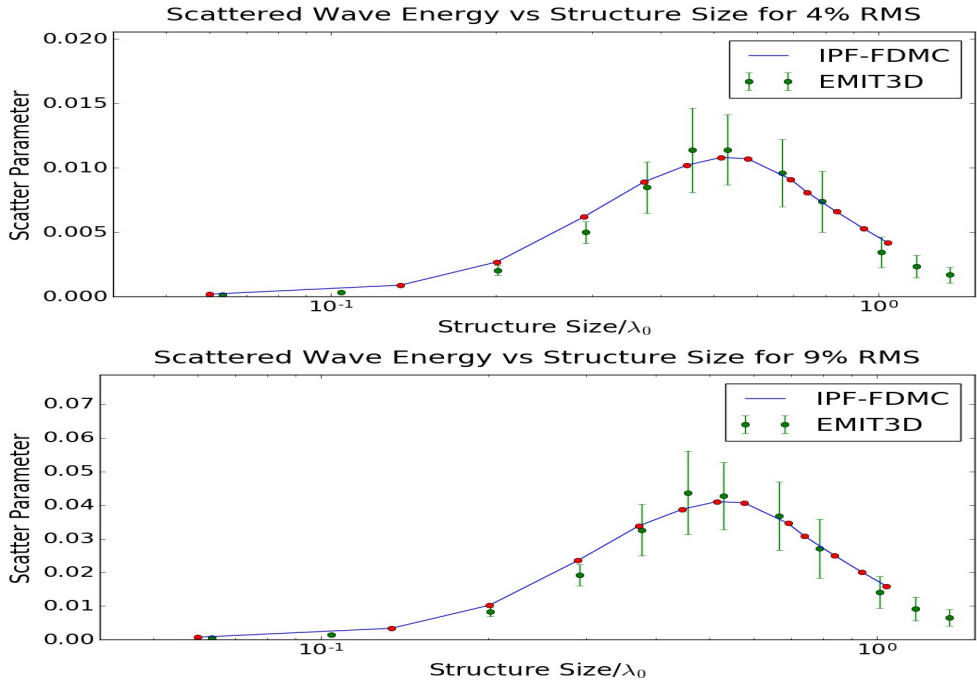


**Figure 4.7:** Dependence of relative turbulence structure size to scattering power for two distinct RMS fluctuation levels (top = 4% and bottom = 9%). The trend is shown for both the 2D (IPF-FDMC) and 3D (EMIT-3D) simulations. The error bars for IPF-FDMC are included but too small to be seen due to the large ensemble taken.

There are three key results to be taken from this parameter scan. Firstly, the maximum effect on the traversing microwave beam is observed for an average correlation length of  $L_C = 0.52(\pm 0.02)\lambda_0$ . This result can be thought of in two ways. Firstly and most simply, the Bragg condition for perpendicular propagation is  $2L_C = \lambda_0$ . Though this is intuitive it is a vast simplification. Secondly, the correlation length can be thought of as the averaged eddy radius and not diameter therefore the peak scattering occurs when the average structure size is the same size as the wavelength. For very large electron density structures exceeding the vacuum wavelength,  $L_C \gg \lambda_0$ , the scattering is expected to reach an asymptotic value. For the microwave, the turbulence layer will then appear as a homogeneously increased or decreased electron density layer. Compared to the case without fluctuations, this will result in increased or decreased divergence of the beam, respectively.

The second result is that the dependence of scattering on correlation length is independent of the fluctuation level. One can see in figure 4.7 that the shape of the curve is exactly the same for both fluctuation levels with the difference coming from the magnitude of the scattering. Finally the third result is that very good agreement

was found between the 3D simulations of EMIT-3D and the 2D simulations of IPF-FDMC despite the low ensemble size used by EMIT-3D. This demonstrates that for perpendicular incidence of the wave on the filamentary structures the scattering is inherently 2D and scatters the power perpendicular to the filamentary structures.

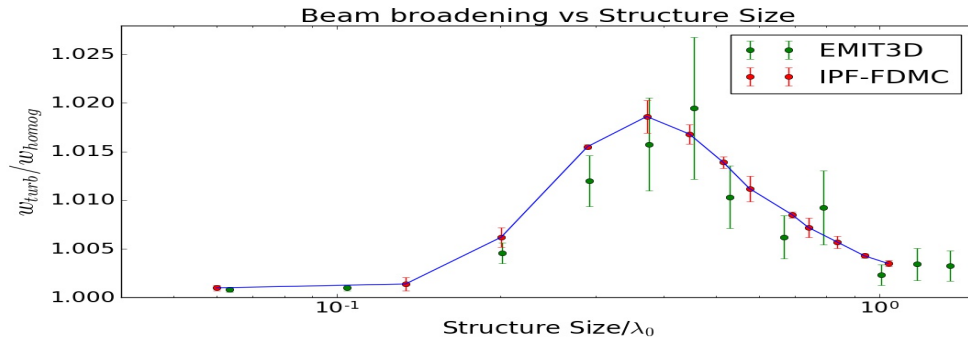


**Figure 4.8:** Average beam broadening as a function of the average structure size  $L_C$  for the case of an average fluctuation level of  $\sigma \approx 4\%$  and a size of the turbulence layer of  $d_{\text{turb}} = 3\lambda_0$ .

The scaling of the average beam broadening with  $L_C$  is qualitatively similar: a maximum perturbing effect at a certain structure size is found (see figure 4.8). This size is, however, slightly smaller than in the case of the scattering parameter  $\alpha$ . For  $L_C \gg \lambda_0$ , both methods approach asymptotically the homogeneous case on both sides of the peak. The agreement between EMIT-3D and IPF-FDMC is degraded somewhat in the large scattering region. This is because in order to calculate the beam width one must take a time average which means that the method is very susceptible to outliers, contributions from uncommonly large or small scattering events. This manifests when performing the Gaussian fit to the time averaged beam which is very sensitive to the shape of the time averaged signal. Therefore, in order to obtain better agreement a larger ensemble is needed for the large scattering region for this method. It should be kept in mind that this method suffers from the fact that scattering into side lobes is ignored as explained in the previous section. The advantage of the scattering parameter  $\alpha$  is that it does not suffer from this problem as it simply sums up the squared deviations from the homogeneous case.

### 4.5.2 Variation of the RMS fluctuation level

To vary the average fluctuation amplitude, the output from the BOUT++ code (the raw density data in 4.1) is multiplied by a constant factor before it is added to the background plasma. This procedure is chosen to ensure that the underlying turbulence remains constant through the parameter scan. The alternative approach would be to re-run the BOUT++ simulations with different input parameters that result in larger fluctuation levels. This would have led to a significant increase in the overall computation time. It has, however, been checked for a few cases that input parameters leading to larger fluctuation amplitudes do not change the other average turbulence parameters, namely the structure size. It is therefore justified to scale the fluctuation amplitude as it is done here. A variation of  $\sigma = 2\%$  to  $12\%$  is realised. The standard parameters of  $n_0 = 0.5n_{e,\text{cut-off}}$  and  $d_{\text{turb}} = 3\lambda_0$  are used. For the average structure size, the value which yielded the strongest perturbation in the previous section 4.5.1 is used,  $L_C \approx 0.52\lambda_0$ .

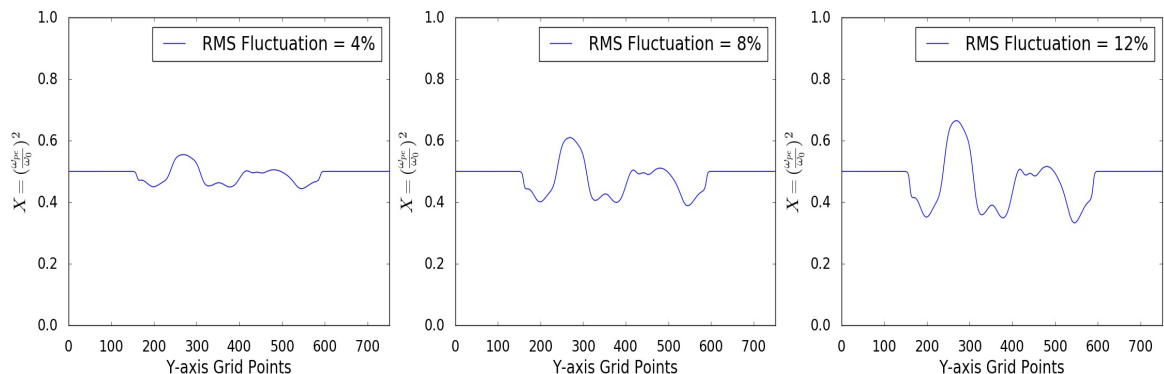


**Figure 4.9:** An illustration showing three different fluctuation levels across the range in the parameter scan. All other plasma parameters are kept constant.

Figure 4.10 shows the scattering parameter  $\alpha$  as a function of the fluctuation level  $\sigma$ . The increase can be described by a power law of the form  $\alpha = a\sigma^b$ , with  $a \approx 1 \times 10^{-3}$  and  $b \approx 1.9$ , i.e. approximately a quadratic increase. When the turbulence layer is assumed to be of small depth and treated as a phase variation of a traversing Gaussian beam, it can be shown that the intensity variation due to the phase perturbation scales with the square of the electron density variation [92]. Hence, the parameters considered for the full-wave simulations in this section resemble this case. The average beam broadening exhibits similar behaviour to the scattering parameter  $\alpha$ . Its dependence

on the fluctuation level can again be described by a power law with rather similar coefficients of  $a \approx 1.1 \times 10^{-3}$  and  $b \approx 2.1$ . Very good agreement is found between EMIT-3D and IPF-FDMC. Better agreement is found for the scatter parameter for reasons explained in the previous section.

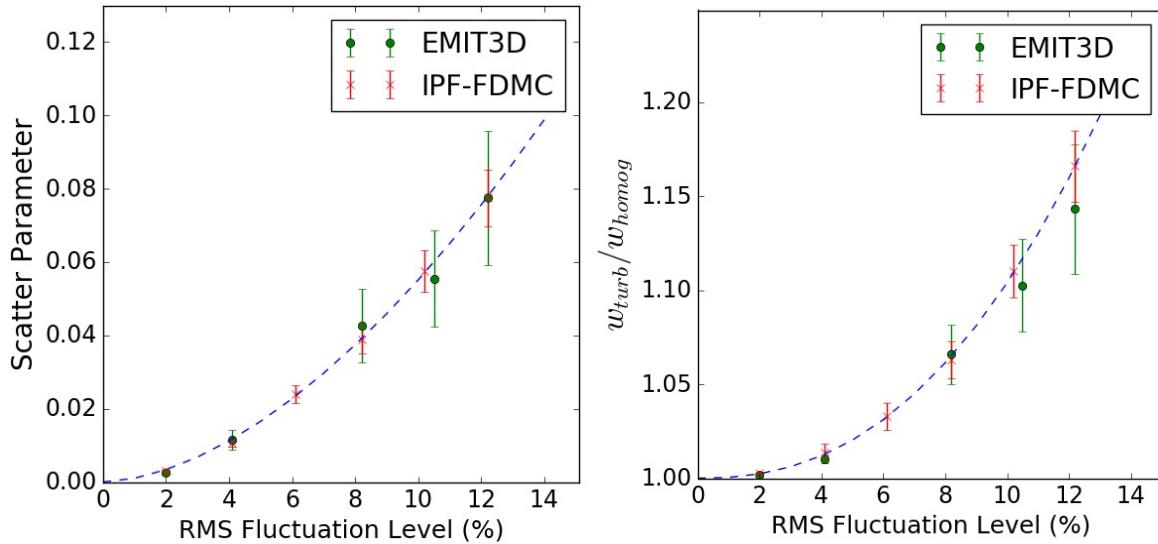


**Figure 4.10:** Left: Median of the scattering parameter  $\alpha$ . Right: Average beam broadening as a function of the normalized fluctuation amplitude for the case of an average structure size of  $L_C \approx 0.52\lambda_0$ , and a depth of the turbulence layer of  $d_{\text{turb}} = 3\lambda_0$ . The dashed line represents a power law fitted to the data.

### 4.5.3 Variation of the turbulence layer thickness

The depth of the turbulent density region is varied in the range of  $d_{\text{turb}} = 2$  to  $7\lambda_0$ . For the average structure size  $L_C$ , the value which yielded the strongest perturbation is again chosen. The average fluctuation strength and the background density are the same as in section 4.5.1.

Figure 4.11 shows the median of the scatter parameter  $\alpha$  as a function of  $d_{\text{turb}}$ . This is the only scan where EMIT-3D and IPF-FDMC disagree. Both codes agree that the scattering increases linearly for small values of  $d_{\text{turb}}$ . However, where EMIT-3D continues to increase linearly towards larger values of  $d_{\text{turb}}$ , IPF-FDMC begins to deviate. The simulations with IPF-FDMC did not increase the domain width with increasing  $d_{\text{turb}}$ . This meant that the domain width was not large enough to include all of the scattered power in the large  $d_{\text{turb}}$  simulations, which led to scattering of the microwave into the left and right boundaries. These components are not detected

by the receiving antenna placed at the top of the computational domain. In EMIT-3D the domain width was increased with increasing  $d_{\text{turb}}$ . Figure 4.2 shows the 3D output from EMIT-3D which for illustration purposes displays a particularly strong perturbing properties,  $L_C \approx 0.52\lambda_0$  and  $d_{\text{turb}} = 3\lambda_0$ . One can see that the microwave begins to split into two beams and so for large values of  $d_{\text{turb}}$  these begin to fall within the boundary layers for IPF-FDMC. The average beam broadening is also shown as a function of  $d_{\text{turb}}$  in figure 4.11. It exhibits a similar behaviour to the scatter parameter.

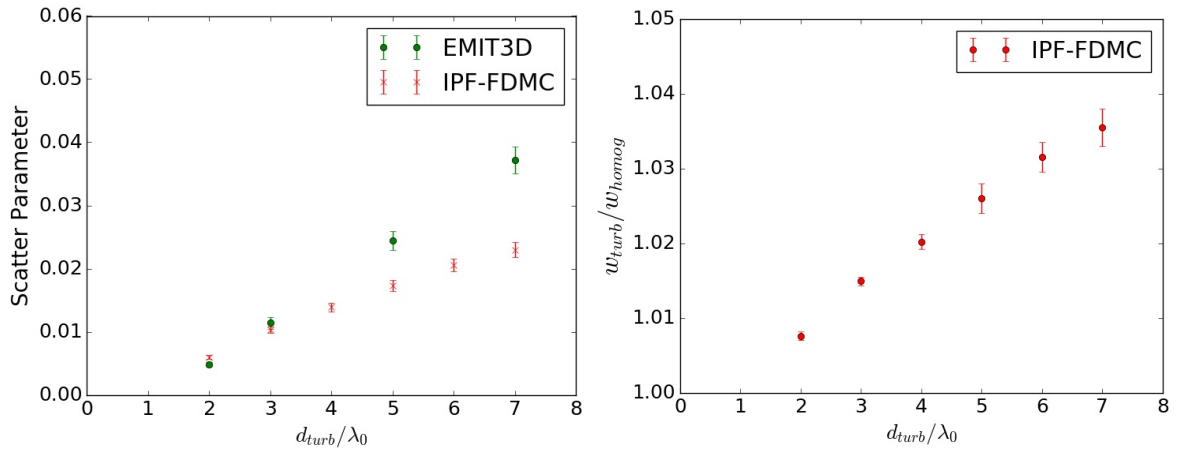


**Figure 4.11:** Left: Median scattering parameter  $\alpha$ . Right: Average beam broadening as a function of the thickness of the turbulence region for the case of an average fluctuation level of  $\sigma \approx 4\%$  and an average structure size of  $L_C \approx 0.52\lambda_0$ .

#### 4.5.4 Variation of the injected beam waist

Future modelling of the scattering of microwave beams through tokamak edge plasmas will aim to model the simulated beam closely. However, experimental beams have a beam waist radius that is approximately 20 times the vacuum wavelength which is an order of magnitude larger than the default value used in these simulations. In the description of the simulation geometry (see section 4.3) it was argued that despite the relatively small value of  $w_0$ , the simulations still resemble fusion-relevant cases. In this section we investigate this point further by scanning through to larger beam waists. To ensure the physics is not affected by the size of the computational domain, the  $x$ - and  $y$ -directions are increased to  $30\lambda_0$ . The other parameters are kept at their default values of  $L_C \approx 0.52\lambda_0$ ,  $\sigma \approx 4\%$ , and  $d_{\text{turb}} = 3\lambda_0$ .

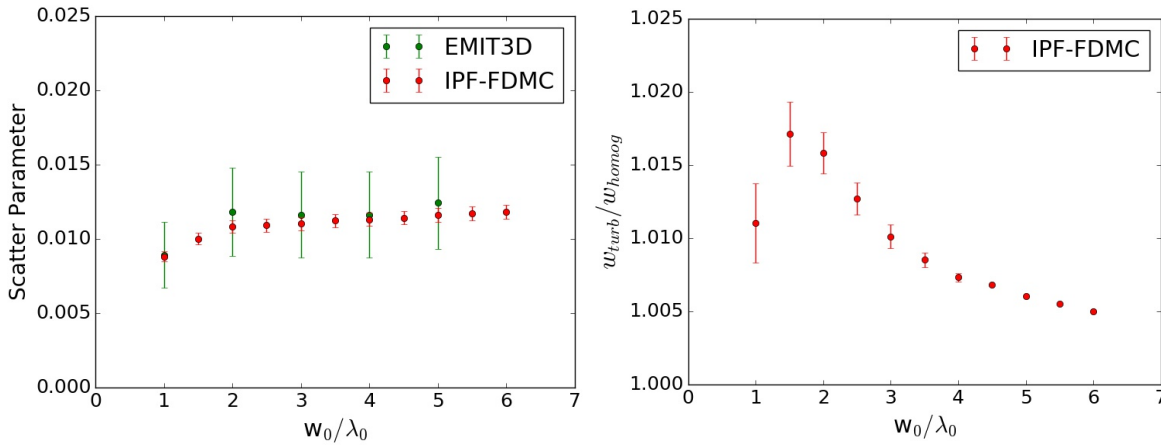


**Figure 4.12:** Left: Median of the scattering parameter  $\alpha$ . Right: Average beam broadening as a function of the size of the beam waist for the case of an average fluctuation level of  $\sigma \approx 4\%$  and an average structure size of  $L_C \approx 0.52\lambda_0$ , and a depth of the turbulence layer of  $d_{\text{turb}} = 3\lambda_0$ .

Figure 4.12 shows the scattering parameter  $\alpha$  asymptotes to a constant value at  $w_0 = 2\lambda_0$ . Therefore, the assumption made that a default value of  $w_0 = 2\lambda_0$  is relevant for fusion experiments holds for the calculation of the scatter parameter. The measure of the beam broadening however exhibits different behaviour. An asymptotic value is still approached but at a larger value of the beam waist. This is due to the fact that the average beam broadening is a normalised quantity (normalised to the unperturbed beam). Thus, the wider the beam, the smaller the relative beam broadening.

The decrease of the beam broadening for the smallest beam considered can be explained by the geometry used: in the detector antenna plane, the smallest beam has a wider electric field distribution as the beam with the next beam width considered. This is due to the strong divergence for the smallest beam considered. The beam broadening graph shows the points from IPF-FDMC only as IPF-FDMC has a much smaller uncertainty. This makes the graph less cluttered so then the shape can be seen more clearly. As has been the case in all other parameter scans, very good agreement has been found between IPF-FDMC and EMIT-3D for the calculation of the scatter parameter. Relatively good agreement was found for the beam broadening yet it was somewhat degraded as compared with the calculation of the scatter parameter. Again this is consistent with previous scans.

### 4.5.5 Variation of the background density

The background plasma density onto which the turbulence is superimposed affects how strongly the beam interacts with the turbulence. The default background electron density value so far has been kept fixed at a value of  $n_0 = 0.5n_{e,\text{cut-off}}$ . This is to ensure that O-mode is the only solution present in the simulation domain. Now it is decreased by a factor of 5 to a value of  $n_0 = 0.1n_{e,\text{cut-off}}$ . In this configuration, simulations were performed with  $d_{\text{turb}} = 3\lambda_0$  and the average electron density structure size which yielded the strongest perturbation. An average scattering parameter of  $\alpha = 2.11 (\pm 0.06) \times 10^{-4}$  is obtained. Note that this is a factor of 50 below the corresponding value for the higher background electron density. The average beam broadening is with a value of  $w_{\text{turb}}/w_{\text{no-turb}} = 1.0002 (\pm 3 \times 10^{-5})$  smaller by a similar factor.

### 4.5.6 Oblique propagation to the filamentary structures

The goal of this section is not to present a comprehensive parameter scan including a full angular scan. Instead the goal is to briefly look at what 3D effects may present themselves when moving to oblique propagation angles to set the precedent for future work. This is the case in experiment when the microwave beam is intended to drive current along the field lines. In this scenario an angle of  $\pi/4$  between the microwave beam and the magnetic field is used.

Figure 4.13 shows a snapshot of the output from EMIT-3D in the geometry described showing iso-field surfaces of the electric field of a microwave beam. The size of the beam waist is  $w_0 = 2\lambda_0$ . The electron density fluctuations are assumed not to vary in the direction parallel to the background magnetic field, thus their filamentary appearance. The scattering of the microwave beam is clearly 3D in nature which results in an interesting impact on the scattering. The beam appears to scatter in a way that does not cause as large of a divergence of the beam as found in the perpendicular cases. In fact indications of a reduced scattering are found as compared to the perpendicular injection. However, the data is not conclusive and require further verification using a sufficiently good ensemble average and a scan through propagation angle.

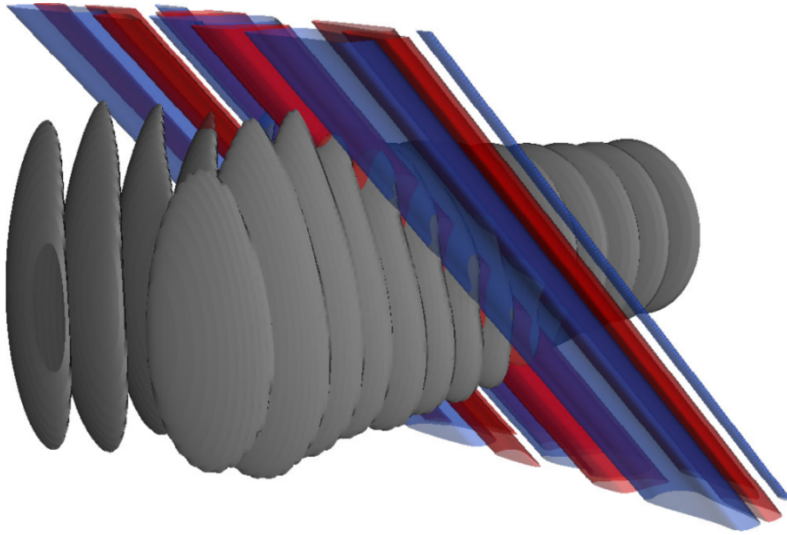


**Figure 4.13:** Snapshot of the positive wave electric field together with contours of the electron density fluctuations (red and blue corresponding to positive and negative perturbations respectively) for an angle of 45 degrees between the injected microwave beam and the electron density filaments.

### 4.5.7 Considerations for the experimentalist

To assist in making the results of the modelling work more accessible to the experimentalist, the consequences of the simulation results are briefly discussed for two different experimental cases. The first case considers the diagnostics of microwave radiation emitted by the plasma. The second considers the localized absorption of high-power microwaves in the confinement region of the plasma.

#### 4.5.7.1 Microwave emission experiments

The case of the synthetic aperture microwave imaging (SAMI) diagnostic installed at the MAST spherical tokamak is considered here [51]. This diagnostic detects electron Bernstein wave emission in a frequency range of 10 to 36.5 GHz, corresponding to a vacuum wavelength of  $\lambda_0 \approx 1$  to 3 cm. The electrostatic electron Bernstein waves are generated by electron temperature fluctuations in the electron cyclotron frequency range. They are mode-converted into electromagnetic waves in the vicinity of the plasma frequency layer and the upper-hybrid resonance layer [93] and can then leave the plasma. The SAMI diagnostic aims to use the recorded signal to estimate the pitch angle and thus the edge current density profile. The case of a background density

of  $n_0 = 0.5n_{e,\text{cut-off}}$  discussed in section 4.5.1 can be applied here. The average size of the density structures at the plasma edge is  $L_C = 5$  to  $10$  cm [94, 95] and an average amplitude of 10% to 20% can be assumed. Comparing the structure size with the wavelength range of the diagnostics, the scattering should be noticeable in the lower frequency range (corresponding to the larger wavelength of the microwave). At the upper end of the frequency sensitivity of SAMI (corresponding to the smaller wavelength of the microwave), it should be strongly reduced. The large frequency range of SAMI provides an interesting scenario to experimentally investigate the scattering of microwaves as a function of the wavelength of the microwave (equivalent to varying the average density structure size). The results could then be compared with appropriate simulations.

#### 4.5.7.2 Microwave injection and absorption experiments

As mentioned in the motivation for this work injected microwaves can be used to drive toroidal currents (ECCD). ECCD beams are used to suppress the growth of magnetic islands in order to stabilize NTMs. In the ASDEX Upgrade tokamak, beams with a heating frequency of 140 GHz are used, corresponding to  $\lambda_0 \approx 2$  mm and a cut-off density of  $n_{e,\text{cut-off}} \approx 2.4 \times 10^{20} \text{ m}^{-3}$  [45]. As a first approximation values of the background density and blob size and fluctuation level are used from a single location, although it is understood that these values change over the large density gradient region. The size of the blobs appearing in the scrape-off layer is on average  $L_C \approx 7$  mm [96], the density at this location is typically  $n_e < 3 \times 10^{19} \text{ m}^{-3} \approx 0.1n_{e,\text{cut-off}}$  [97] and the fluctuation strength  $\sigma \approx 15\%$ . Despite this rather large fluctuation amplitude, the effect on the injected microwave is expected to be small since the background density is far below the corresponding cut-off density. This has been discussed in section 4.5.5. The distance from the antenna to the intended place of absorption is, however, very large with a value on the order of  $100 \lambda_0$ . Very small scattering angles are therefore expected to be of larger significance than in the simulation geometry discussed in this paper.

## 4.6 Summary

In this chapter the scattering effect of turbulence on an O-mode microwave beam, injected perpendicular to the density filamentary structures (and magnetic field), has been investigated. It is the first time a parameter scan of these parameters has been performed. The work has produced the basic knowledge of the dependence of microwave scattering power on the turbulence parameters from which future work can be built. Full-wave simulations have been used which capture the full effect of the scattering on the wave mechanics. In a series of parameter scans the properties of the electron density fluctuations and of the microwave beam have been varied. Very good agreement between 2D and 3D simulations was demonstrated for all sets of parameters which shows that the scattering at perpendicular injection is purely 2D in nature. The strongest scattering of the microwave beam was found for a perpendicular correlation length of the electron density structures of  $L_C \approx \lambda_0/2$ . The correlation length corresponds to an average eddy radius so this result means that the peak scattering occurs when the structure size is the same size as the wavelength. The scattering of the microwave and the average beam broadening were found to increase linearly with the depth of the turbulence layer and quadratically with the fluctuation strength. The quadratic behaviour corresponds to the theory of scattering at a thin phase grid. An asymptotic behaviour was observed for increasing the size of the beam waist. This result is very important for future simulations which aim to directly model experiment because it is now understood that one may use a smaller beam waist in the modelling which vastly reduces computational expense. Indications for an overall reduced scattering were found if the microwave beam propagates obliquely to the electron density perturbations which is a purely 3D effect. As a next step the knowledge gained from the simulations here will be applied to modelling the scattering of an experimental microwave beam. The simulations will aim to model as closely as possible the experimental system and therefore test our most complete theory of the wave mechanics and turbulence against experimental measurements of beam broadening.

# Chapter 5

## Resolving ECRH deposition broadening due to edge turbulence in DIII-D by 3D full-wave simulations

The work presented in this chapter has been previously published in:

“*Broadening of microwave heating beams in the DIII-D tokamak by edge turbulence*”:  
M.B. Thomas, M.W. Brookman, M.E. Austin, K. Barada, M. Cenghar, R.J. La Haye,  
J.B. Leddy, T.C. Luce, C.C. Petty, T. Rhodes, Z. Yan, A. Köhn and R.G.L Vann:  
Submitted to *Phys. Rev. Lett.* Mar 2018.

“*Resolving ECRH deposition broadening due to edge turbulence in DIII-D by the  
heat flux measurements*”:  
M.W. Brookman, M.B. Thomas, M.E. Austin, K. Barada, M. Cenghar, R.J. La Haye,  
J.B. Leddy, T.C. Luce, C.C. Petty, T. Rhodes and R.G.L. Vann: Submitted to *Nucl.  
Fusion* Apr 2018.

Uploaded to ArXiv: 1710.03503 10/10/2017

“*Resolving ECRH deposition broadening due to edge turbulence in DIII-D by 3D  
full-wave simulations*”:  
M.B. Thomas, M.W. Brookman, M.E. Austin, A. Köhn, R.J. La Haye, J.B. Leddy,  
R.G.L Vann and Z. Yan: Submitted to *Nucl. Fusion* Apr 2018.

Uploaded to ArXiv: 1710.03028 09/10/2017

## 5.1 Motivation

Many current and future magnetically confined fusion devices rely on collimated electromagnetic beams for precision heating and current drive in the plasma. ITER will use O-mode beams to provide electron cyclotron resonance heating (ECRH) and current drive (ECCD) from an upper port launcher. One primary objective is to stabilise the expected  $m = 3$ ,  $n = 2$  and the  $m = 2$ ,  $n = 1$  neoclassical tearing modes (NTMs) [24, 98]. As discussed in chapter 1, section 1.2, the stabilising effect of ECCD is most effective within the O-point of the NTM. Consequently if the deposition profile is broadened to be larger than the island width or the alignment of the beam is not centred on the O-point then the stabilising efficiency is reduced [46]. However it has been widely observed that significant broadening of the ECRH deposition profile occurs to a varying degree (1.4 – 2.7 times the width calculated by a beam tracer) across a range of devices such as ASDEX-U [99], DIII-D [100–102] and TCV [103] in a range of operating scenarios. This is of concern for ITER as it increases the power required to suppress a given island. Previous work suggests that for the current ITER design, full ECCD power from all gyrotrons is needed to suppress the 3/2 island if the deposition profile is broadened by  $> 200\%$  compared to ray tracing calculations [104]. This means that there will not be any power remaining to stabilise the 2/1 island. More recent work suggests that a deposition broadening by  $> 100\%$  may necessitate power modulation for NTM suppression [105]. Most important however, is that the performance Q value of ITER will be reduced if it becomes necessary to increase the power requirements for NTM suppression or to continuously use ECCD power. This is of direct consequence for one of ITER’s main goals.

The broadening of ECRH deposition profiles has usually been attributed to the radial transport of fast electrons through diffusion [99, 100, 106]. Though this is able to explain the broadening profile observed, the necessary bremsstrahlung emission that would be associated with the large radial transport of fast electrons is not observed

in experiment [107, 108]. Furthermore it is noted in Ref. [105] that if the profile is broadened by scattering of the beam by density fluctuations in the edge then the impact of finite transport is reduced. With a view to ITER, direct simulation of the 3/2 and 2/1 surfaces by gyrokinetics code GKW [109] constrains the diffusion coefficient to a value that would account for broadening of the deposition profile by only 10% [110]. Indeed recent experiments [101–103] have shown a significant broadening effect which is attributed to scattering of the ECRH beam by density perturbations in the edge.

There are many predictions for ECCD broadening due to edge density fluctuations using beam tracing codes with a statistical turbulence approximation [74–78, 103]. There are no similar studies using a full wave code along with a turbulence code to treat the edge. This makes benchmarking with our most complete theoretical description impossible. Furthermore there has only been one ray tracing study (with statistical turbulence included) which directly compares the modelled ECRH beam broadening with the experimentally measured heating profile, for a particular shot, on a systematic basis [103]. As a consequence there have been no opportunities to test our theoretical models in multiple shots with substantially differing edge turbulence (once more there is no full wave equivalent). The purpose of this work is to address these issues. The chapter is laid out in the following way: we begin in section 5.2 with the experimental measurements of ECRH broadening in DIII-D for the specific shots simulated by EMIT-3D. In section 5.3 the turbulence model (section 5.3.2) is outlined along with the method for matching the simulated turbulence domain to experimental turbulence. Section 5.4 presents the analysis of simulation results and section 5.5 provides a discussion of the work.

## 5.2 Experimentally measured ECRH Deposition Broadening in DIII-D

In DIII-D 110 GHz X-mode polarised beams are used to drive ECCD and ECRH at the location where the electron cyclotron frequency is 55 GHz (second harmonic absorption). Beams from up to 6 gyrotrons are launched from a set of steerable mirrors

located at a poloidal angle of  $60^\circ$ . The beam waist radius at the launcher is between 6–7 cm ( $\approx 23\lambda_0$ ) depending on the launcher, resulting in a Gaussian beam with a large waist to wavelength ratio which can be approximated as a plane wave solution with very little divergence. The beam path and deposition profile is calculated by the ray tracing code TORAY-GA on a shot by shot basis (see figure 5.1). The corresponding experimental work to this chapter, described in detail in [102], has shown significant differences between the calculated deposition profile and the measured heating profile. It was found that the broadening of the heating profile cannot be explained by transport effects and instead is found to scale with the level of edge density fluctuation. This led to the conclusion that the beam broadening is caused by scattering of the beam in the tokamak edge region. The experimental broadening is defined as a ratio of the measured heating deposition width and that calculated by TORAY-GA and is shown in table 5.1.

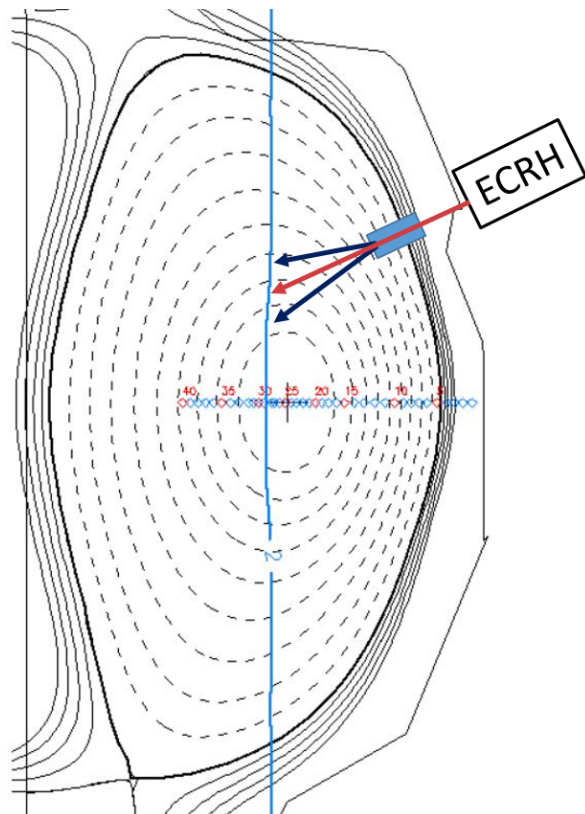


**Figure 5.1:** An illustration of the ECRH launch angle and path of the rays. The blue rectangle approximately covers the full wave simulation domain and the arrows by the subsequent projection technique discussed in section 5.4.2. The blue vertical line is the targeted electron cyclotron resonance surface. The separatrix is denoted by the solid black line. The blue circles along the mid-plane illustrate the view of the diagnostics relative to the ECRH injection.

	Neg-Tri	Diverted	QH-mode	Limited	Diverted
	L-mode	H-mode		L-mode	L-mode
	#166191	#165146	#157131	#154532	#165078
Fluc. Level	3	5	8	10	12
Broad. Fac.	$\times 1.4 \pm 0.2$	$\times 1.7 \pm 0.2$	$\times 1.9 \pm 0.4$	$\times 2.3 \pm 0.2$	$\times 2.7 \pm 0.3$

**Table 5.1:** Plasma scenario and corresponding shot number with measurements of the fluctuation level made on the normalised poloidal flux surface  $\psi_N = 0.95$  and the ECRH broadening factor relative to ray tracing calculations.

## 5.3 Theoretically modelled ECRH Deposition

### Broadening in DIII-D

#### 5.3.1 The simulation domain and beam initialisation

Of the cases shown in table 5.1 three cases with distinct edge plasma characteristics, L-mode, H-mode and negative triangularity L-mode, are considered to compare directly with experiment. As discussed in section 5.1, a full wave treatment is only necessary when the inhomogeneity scale length is comparable to the wavelength. This occurs in the steep density gradient region of the plasma edge. Because full wave simulation is computationally expensive, the simulation domain is chosen to span the region about the separatrix shown in figure 5.1. The method for propagating to the absorption surface from the end of the simulation domain is discussed in section 5.4.2. To reduce computational expense the domain size was constrained to be as small as possible without affecting the wave mechanics. To this end a resolution of 20 Yee cell grid points per vacuum wavelength is chosen in EMIT-3D. The optimum width of the simulation domain was found to be 4 times the beam diameter in the direction perpendicular to the filamentary structures in  $\hat{x}$  (where scattering is expected) and 1.8 in the direction parallel to filamentary structures in  $\hat{y}$  (figure 5.2). The experimental beam waist is  $47\lambda_0$  which is not practical to simulate here. Instead a beam is launched which ensures a flat plane wave-front. It was found in previous work [111] that the dependence of scattering power of turbulence on a Gaussian beam asymptotes to a constant value

beyond a beam waist  $6\lambda_0$ . Therefore  $6.8\lambda_0$  was chosen to represent the experimental beam. An X-mode Gaussian beam is launched by exciting only the component of the wave electric-field that is perpendicular to both the background magnetic field and the wave vector,  $\hat{\mathbf{k}}$ , within a homogeneous background plasma. The background plasma is then smoothly transitioned to the turbulence profile by use of a hyperbolic tangent function. The turbulence layer was  $38\lambda_0$  deep in the propagation direction  $\hat{z}$ .

### 5.3.2 Generation of the turbulence

The turbulence used for simulating microwave interaction was generated using the BOUT++ framework [86]. The Hermes model [112] was simplified to include only electrostatic effects in a quasi-3D geometry. In the perpendicular plane the fluid equations were modelled explicitly, while separate closures were used for the parallel direction to simulate the behaviour inside and outside the separatrix. The Hasegawa-Wakatani [88] closure describes the closed field line region, which models nearly adiabatic electrons through a parallel current and resistivity. Outside the separatrix, a sheath model provides a sink for plasma density and energy [113].

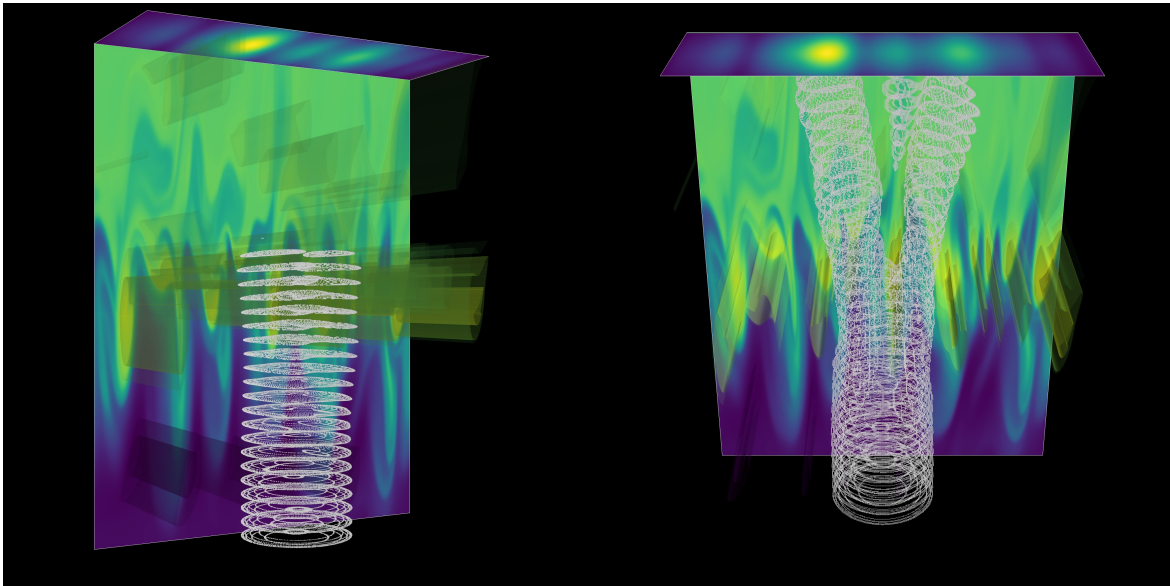


**Figure 5.2:** The output from EMIT-3D for one particular turbulence snapshot in the ensemble for L-Mode. Left: The 2D turbulence profile generated by BOUT++ is shown to be extended along the magnetic field lines into filamentary structures and a 3D wave propagates from low density to high density (blue to green). The white contours are plotted at the beam width where the amplitude falls to  $1/e$  of the maximum. Right: A later time in the same simulation where a particularly large structure is seen to split the beam. The image at the backplane (top) is the RMS electric field calculated over two wave periods.

### 5.3.3 Using experimental diagnostics to constrain the simulated turbulence characteristics

We begin with the diverted L-mode shot #165078. The Thomson Scattering diagnostic [114] provides the time averaged electron density (henceforth referred to as density) and electron temperature profile whilst EFIT provides the magnetic field. These serve as inputs to the Hermes model and drive the plasma turbulence. As the frequency of the wave is much larger than the eddy turnover frequency, the turbulence is considered as stationary. Therefore, as the turbulence evolves in time, 2D density profile snapshots are selected at sufficiently spaced time intervals to provide a large uncorrelated ensemble in order to capture the time averaged effect of turbulence on the beam. Away from the divertor the parallel density gradients are negligible due to fast parallel transport. This requires that the 2D profile is then extended into 3D along the magnetic field lines reproducing the distinctive filamentary structures. The ensemble characteristics are then cross-checked with experiment to ensure that the spatial distribution of the root mean square (RMS) fluctuation level  $\xi$ , time averaged density  $n_{e,0}(r)$ , poloidal and radial correlation lengths are matched. The RMS fluctuation level is obtained by beam emission spectroscopy (BES) [115]. It is defined in equation 5.1 as the RMS fluctuation amplitude normalised to the time averaged density. The RMS fluctuation amplitude is defined as  $\tilde{n}_e(r) = \sqrt{\sum (n_e(r,t) - n_{e,0}(r))^2 / N}$ .

$$\xi = \sqrt{\frac{1}{N} \sum_{t=1}^N \left( \frac{n_e(r,t) - n_{e,0}(r)}{n_{e,0}(r)} \right)^2} \quad (5.1)$$

$N$  is the ensemble size and  $n_e(r,t)$  denotes the density profile in  $r$  for an instantaneous time  $t$ . The correlation length,  $L_C$ , is defined as the average distance over which the normalised autocorrelation falls off to 0.5 which corresponds to the eddy radius when the density fluctuation amplitude falls to  $1/e$ . This is clearly an averaged quantity and a range of structure sizes of differing power are present in the profile. The physics governing the correlation lengths is vastly different over the radial extent of the simulation domain spanning the separatrix. In the scrape off layer (SOL), blobs

dominate the structure therefore the radial correlation length is dominated by larger length scales [116,117] and across the separatrix the simulations show that radial length scales are enlarged due to the radial direction of advection. By contrast, inside the separatrix the binormal correlation length has been measured to be of the same size [118] and even larger [119]. It is difficult to exactly define the ratio between the radial and poloidal length scales on average in experiment due to the sensitivity of different diagnostics to specific values of  $k$  and also due to the spatial and temporal resolution. What can be stated though is a range in which the measured correlation lengths lie for DIII-D [53,120,121]. This is used as the constraint for the simulations. Furthermore as the correlation length describes only an average quantity it is necessary to check the  $k$  power spectrum of the simulated turbulence. The spectrum follows known power laws in specific regions corresponding to different underlying turbulence mechanisms, a comprehensive review of which can be found in Ref. [57].

Figure 5.2 illustrates the simulation domain with the turbulence generated from the Hermes model and the EMIT-3D output. Figure 5.3 shows the simulated and experimentally measured parameters described above for each of the cases modelled. The BES data for the RMS fluctuation level is only present inside the separatrix. Outside the separatrix it is understood that the fluctuation level continues to increase up to levels of 60% and in some cases 100%. A comprehensive review of edge turbulence measurements in toroidal fusion devices [53] demonstrates this increase in the SOL. The fluctuation levels and correlation lengths are also consistent with previous DIII-D measurements [53,57,120,121].

The turbulence mechanism for the negative triangularity L-mode operating scenario is the same as that for normal L-mode configuration though significantly suppressed [122]. Therefore the same profiles generated for the normal L-mode scenario were scaled to fit the negative triangularity experimental data. The time averaged density is changed by dividing through each snapshot with the L-mode time averaged density and multiplying through by the fit to the negative triangularity data. In a similar way once the time averaged density has been removed, leaving only the fluctuations, the RMS fluctuation level can be manipulated using a fit to the BES data

for the required shot. The correlation length is altered through interpolation of the grid to span a larger or shorter distance relative to the wave as required. Ideally for H-mode a multi scale gyrokinetics simulation of DIII-D would be used. However this was not available due to the huge computational expense of such a simulation at a grid resolution small enough for the wave mechanics to fully interact with the fine structure. Therefore the turbulence profiles generated by Hermes were scaled as described above to be consistent with the measured turbulence parameters of the H-mode shot. The radial correlation length in H-mode is expected to be reduced in comparison to L-mode due to the  $\mathbf{E} \times \mathbf{B}$  shear flow whilst increasing in the binormal direction [32, 57, 60]. For negative triangularity the correlation lengths are generally unchanged from L-mode according to the dimensionless  $\rho^* = \rho_i/a$  scaling law previously shown in [57, 119]. The experimental and simulated parameters for each case are shown in figure 5.3.

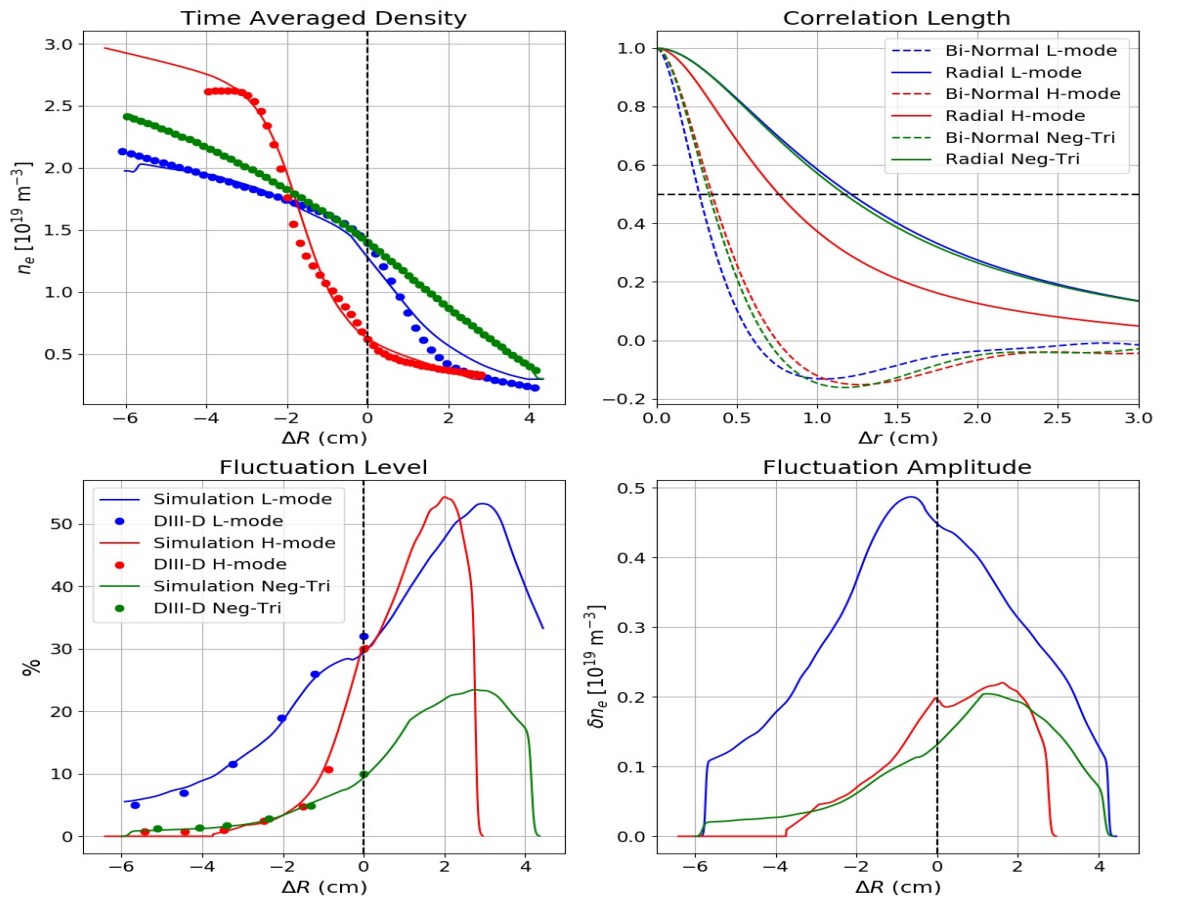


**Figure 5.3:** The properties of the generated turbulence ensemble along with the corresponding DIII-D measurements for each scenario considered. The dots represent experimental measurements whilst the solid lines are from the simulated turbulence. Each scenario is colour coded as shown in the legend of the bottom left plot.  $\Delta R$  is with respect to the outboard mid-plane with 0 denoting the separatrix.

An unavoidable challenge between experiment and simulation was encountered. The ECRH beam launcher is located at a poloidal angle of  $60^\circ$  whereas the diagnostic data used to match the simulation to experiment is located on the mid-plane. Recent global simulations of DIII-D [112, 123] have demonstrated that the turbulence amplitude changes with poloidal angle. The change is either positive or negative depending on the turbulence model used and the operating regime considered. Therefore it is not understood whether the change occurs in the same way for the total  $k$  spectrum of the turbulence or part of it. What can be concluded though is because the change in angle from the mid-plane is small (see figure 5.1) one should expect only a slight difference between the broadening estimated here and the measured deposition profile broadening.

## 5.4 Results

### 5.4.1 The ensemble

For each modelled scenario, a reference case is needed where the beam propagates through the time averaged density profile without turbulence. When turbulence is added a large ensemble of simulations per scenario is required. The root mean square of the wave electric field (equation 5.2) is calculated for each snapshot which is used to define a scatter parameter,  $\alpha_s$  (equation 5.3), which can be physically interpreted as a measure of the percentage change in the distribution of the beam energy across the two dimensional grid at the back-plane. The back-plane is shown in figure 5.2.

$$E_{\text{RMS}} = \sqrt{\frac{1}{2T} \sum_{t=1}^{2T} (E_{x,t}^2 + E_{y,t}^2 + E_{z,t}^2)} \quad (5.2)$$

$$\alpha_s = \frac{\sum_{i,j} (\widetilde{E}_{\text{RMS}}^2(i,j) - E_{\text{RMS}}^2(i,j))}{\sum_{i,j} E_{\text{RMS}}^2(i,j)} \quad (5.3)$$

$$\sigma_{\text{ensemble}} = \sqrt{\frac{1}{N} \sum_{s=1}^N (\alpha_s - \text{mean}(\alpha_s))^2} \quad (5.4)$$

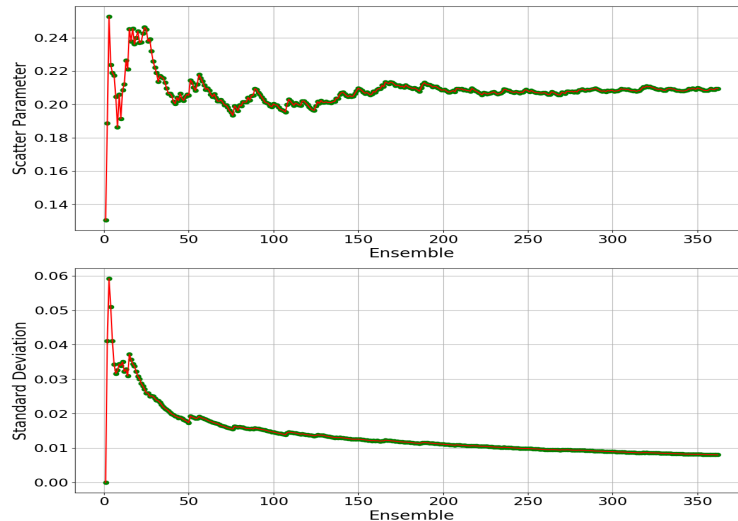


**Figure 5.4:** Convergence of the scatter parameter  $\alpha$  and the standard deviation  $\sigma$  with increasing ensemble size for L-Mode.

The necessary ensemble size may be determined by looking for the convergence of both the mean of  $\alpha_s$  over the ensemble (denoted  $\alpha$ ) and also its standard deviation  $\sigma$  (figure 5.4). For L-mode, convergence was found after approximately  $N = 250$  simulations though  $N = 360$  were used in the total ensemble. For H-mode and negative triangularity, convergence was found much sooner because the turbulence was weaker and therefore did not perturb the beam to the same extent. This allowed a smaller ensemble size of 150 to be used.

Once these parameters are observed to converge sufficiently one may take the mean of the RMS wave electric field along the beam propagation to analyse the time averaged effect of the beam over the ensemble. The result is a Gaussian beam with increased width and divergence in relation to the reference case due to scattering from turbulence (figure 5.5). However it is noted that though the main body of a time averaged scattered beam fits very well to a Gaussian, side lobes develop which are not captured by the Gaussian function; these will be discussed later.

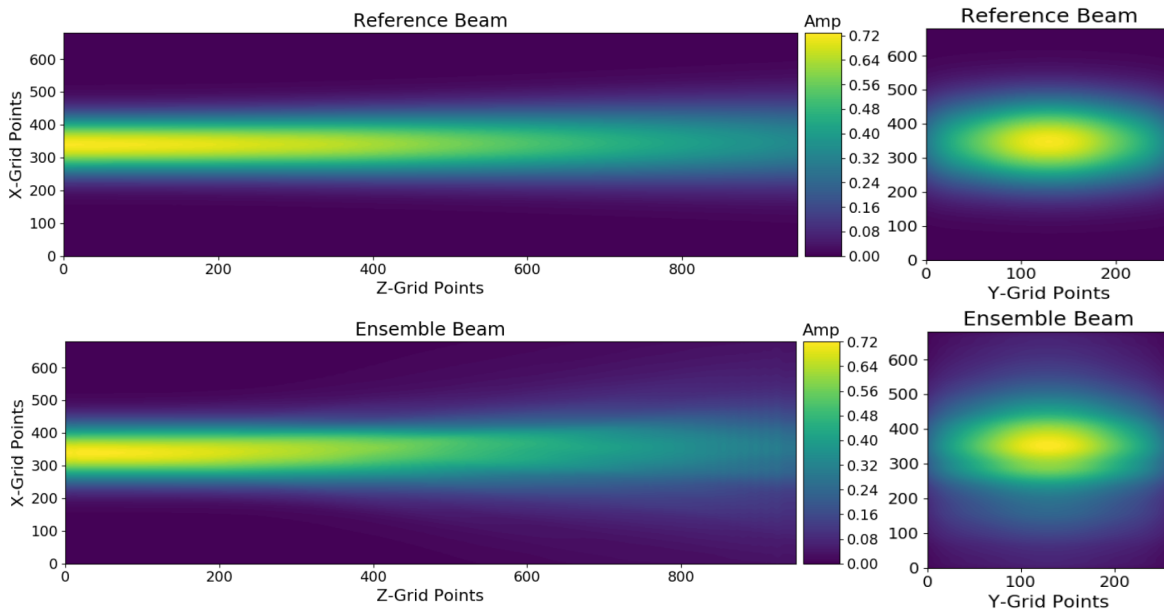


**Figure 5.5:** Output from the L-Mode simulations. Left: The RMS electric field of the ensemble beam and the reference beam along the propagation direction. Right: A cross section through the beam at the back-plane.

### 5.4.2 Projection to the absorption surface

The absorption surface of the ECCD power is much further into the plasma than the edge of the simulation domain. The exact distance is case specific. Due to the difference in divergence, the ratio of the beam widths will not remain constant from the simulation domain back-plane to the absorption surface. Therefore a method is required to calculate the ratio at the absorption surface given the divergence of both beams at the end of the simulation domain. The envelope of a Gaussian beam in homogeneous space after the Rayleigh range ( $R_R = \pi w(0)^2/\lambda_0$ ) will asymptote to a straight line drawn to infinity from the centre of the beam at the waist, at an angle corresponding to the divergence of the beam. This quality of a Gaussian beam allows one to fit straight lines to the envelope of the beam after the Rayleigh range to extrapolate the beam to greater distances assuming the subsequent propagation is through homogeneous space. This can be done for both the reference beam and the ensemble scattered beam as a first order approximation. This also assumes that the ensemble beam continues to be well described by a Gaussian whose divergence is defined by the ensemble scattering in the simulation domain.

The limitation of the method is that no further refractive effects from the changing

density gradient and magnetic field vector will be included. A further broadening of the beam is expected due to the orientation of the beam  $k$  vectors distributed over the wave-front to the density gradient vector and magnetic field vector. This effect is expected to be small due to the length scale of the gradients in comparison with the wavelength and will affect both the reference and ensemble beam in the same way. However the effect will be larger for the ensemble beam due to its larger divergence and although it will result in an underestimation of the broadening at the absorption point it is not thought to contribute by more than 10% as a conservative estimate.

### 5.4.3 Beam broadening in each scenario

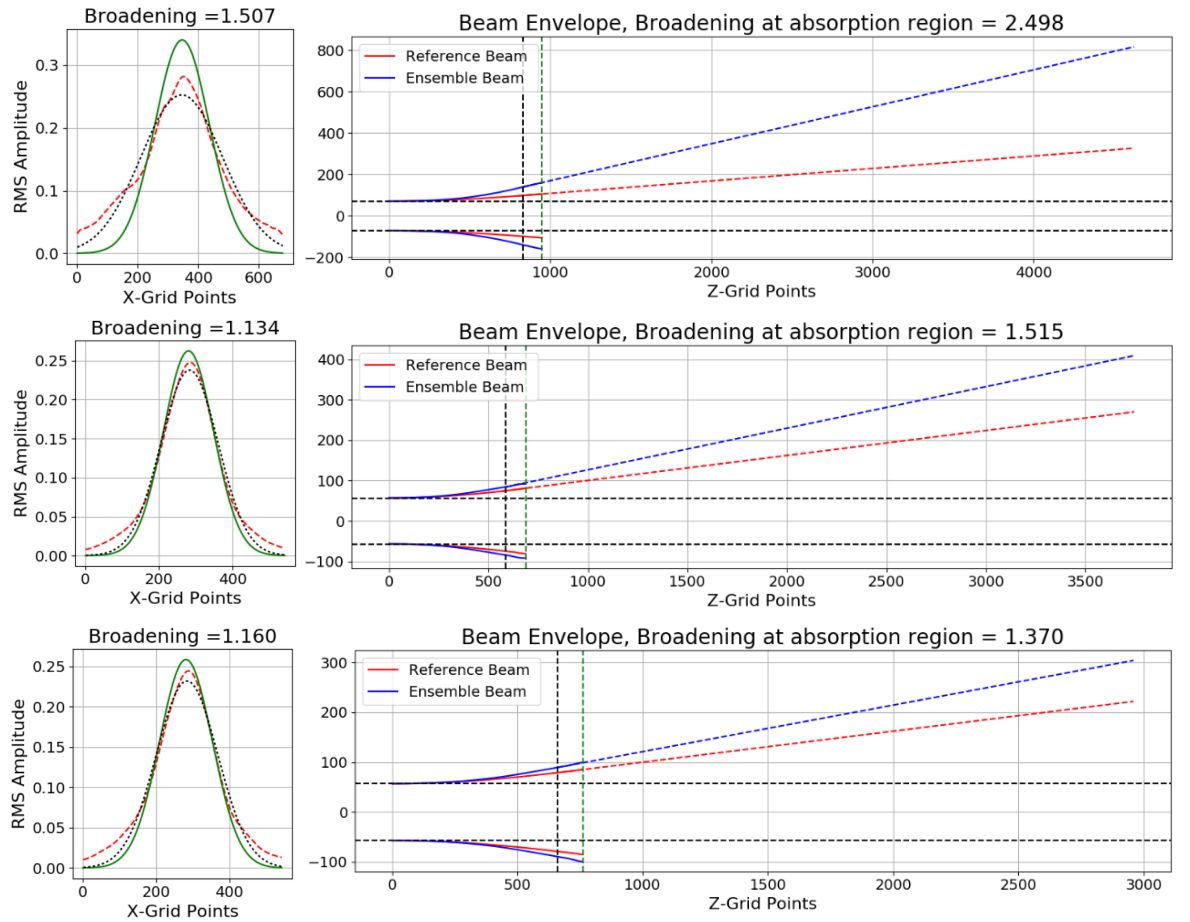


**Figure 5.6:** The top panel of plots are the L-Mode results, the middle panel is H-Mode and the bottom panel is negative triangularity. Left: A line plot of the back-plane beam cross section taken in the scattering direction. The backplane location and the scattering direction is shown as the green dashed line on the right hand plot. Shown is the RMS electric field for both the reference beam (green), the ensemble beam (red dashed) and the Gaussian fit (black dashed) to the ensemble beam. Right: Extrapolation of the beam envelope to the absorption region from the end of the simulation domain (green dashed line). The extrapolated line is fit between the black and green dashed lines at the end of the simulation domain.

Figure 5.6 shows the results of the three modelled scenarios and table 5.2 compares these with the experimental measurements. For each of the scenarios in figure 5.6 one can see the full scale of the beam paths. The solid blue and red lines show the beam envelope of the ensemble and reference beams respectively inside the simulation domain which ends at the vertical green dashed line. The dashed blue and red lines then show the extrapolation of the beams as discussed in section 5.4.2. The lines are fitted according to the divergence of the two beams at the end of the simulation domain between the black and green dashed lines. The path length to the absorption surface from the end of the simulation domain is different in each case. In L-mode this was 40.1 cm ( $\approx 147\lambda_0$ ), in H-mode it was 41.7 cm ( $\approx 153\lambda_0$ ) and in negative triangularity it was 30.0 cm ( $\approx 110\lambda_0$ ). It must be noted for comparing each graph directly, that for L-mode, a resolution of 25 grid points per wavelength was used and this was decreased to 20 in all other simulations.

In each case it is noted that side lobes develop which is an inherent property of scattering from turbulence and not dependent on the ensemble size. The side lobes are a direct result of the scattering from turbulent fluctuations having correlation lengths similar to the vacuum wavelength of the injected microwave and/or having a significant amplitude. This effect would not be expected in turbulence that is smoothly varying relative to the wavelength. It has been shown in [124] that the magnitude of scattering due to turbulence follows a log-normal distribution. The consequence is the occurrence of random large scattering events which significantly perturb the beam. The effect on the time-averaged beam is the appearance of side lobes which deviate from the Gaussian normal distribution. The ramification for the experiment is that more power may fall outside the width calculated here.

The broadening effect of the edge plasma (i.e that calculated in the simulation domain only) is slightly more in negative triangularity than it is in H-mode despite the fluctuation level of the turbulence being larger in H-mode. This is due to the higher background density in negative triangularity combined with the much shallower gradient. This means that the actual fluctuation amplitude is the same as in H-mode

and actually remains higher for a longer distance (see figure 5.3). The result is therefore not surprising and one can see that the reason the beam broadening is smaller at the absorption region is due to the much smaller propagation distance. It follows that the scaling of the expected beam broadening cannot simply be attributed to a measure of the fluctuation level at the edge but a combination of the background density and the fluctuation level. Moreover, the shape of the density profile and the fluctuation level profile play a major part in the magnitude of the beam broadening. This will be discussed further in the following section.

	Neg-Tri L-mode #166191	Diverted H-mode #165146	Diverted L-mode #165078
Exp. Broad. Fac.	$\times 1.4 \pm 0.2$	$\times 1.7 \pm 0.2$	$\times 2.7 \pm 0.3$
Sim. Broad. Fac.	$\times 1.370 \pm 0.074$	$\times 1.515 \pm 0.102$	$\times 2.498 \pm 0.298$

**Table 5.2:** The experimental measurements of the ECRH deposition profile broadening and the calculated beam broadening from the simulated ECRH beam in the same shot.

The errors on the calculation of the beam broadening from the simulation side are broken down as follows. The standard deviation is seen to converge between  $\pm 6\%$  to  $\pm 7\%$  depending on simulation scenario therefore contributing the same amount to the uncertainty on the beam broadening. A further contribution to the uncertainty as discussed in section 5.4.2 comes from the method to extrapolate the beam envelope to the absorption region. This contributes  $+10\%$  from the difference in refraction that will be encountered by the two beams through the core. A further  $\pm 7\%$  comes from the uncertainty in the fit of the line to the limited number of wavelengths at the end of the simulation domain and is calculated as the spread in broadening encountered. The total error is a combination of two indeterminate errors for which the sign is unknown and one determinate error with positive sign. When added together the indeterminate errors sum in quadrature and the determinate error sums conventionally. Consequently, the total error on the calculated beam broadening is  $\sigma = \sqrt{7^2 + 7^2} + 10 = 19.9\%$ . The uncertainty due to the mismatch in diagnostic position and ECRH launch position is unknown and therefore noted but omitted.

One can see from table 2 that the simulated beam broadening agrees with the experimental results very well and within the errors on the calculations. However there is a consistent under-prediction of the broadening. There is a slight discrepancy between the turbulence encountered by the experimental beam and the simulated beam due to the location of the diagnostics on the mid-plane and the injection angle at  $60^\circ$  as discussed in section 5.3.2. However it is uncertain whether this would lead to an under or over-prediction of the broadening. Most likely the consistent nature of the under-prediction could be partially attributed to the fast electron transport which is not decoupled from the experimental measurement and is contained within the errors. This is consistent with the constraint on the fast electron transport to contribute no more than 10% to the deposition broadening [110]. Furthermore, as discussed in section 5.4.2, the method for projecting to the absorption surface is predicted to underestimate the broadening by no more than 10% as a conservative estimate, which is contained in the simulation errors. These two effects combine to explain the consistent under-prediction. L-mode and negative triangularity simulations both agree with experiment to the order of 10%, whereas H-mode is of the order 25%. The reason for this extra 15% may be attributed to the resolution of the diagnostics, which affects the H-mode simulation the most due to the large gradients in the edge. This is discussed in the following section.

#### 5.4.4 Sensitivity of the modelled broadening to resolution of diagnostics

Both the Thomson scattering and the BES diagnostic systems have a spatial resolution of 5 mm. This means a misalignment of the profiles of up to 1 cm is possible. Furthermore the BES has the largest measurement error of up to 20% in the fluctuation level. Due to the uniquely steep gradients in H-mode of both the fluctuation level profile and the time averaged density profile the combination of these two uncertainties on the calculated beam broadening may be substantial. Modelling provides the ability to artificially scan through these uncertainties to quantify the effect on the predicted broadening.

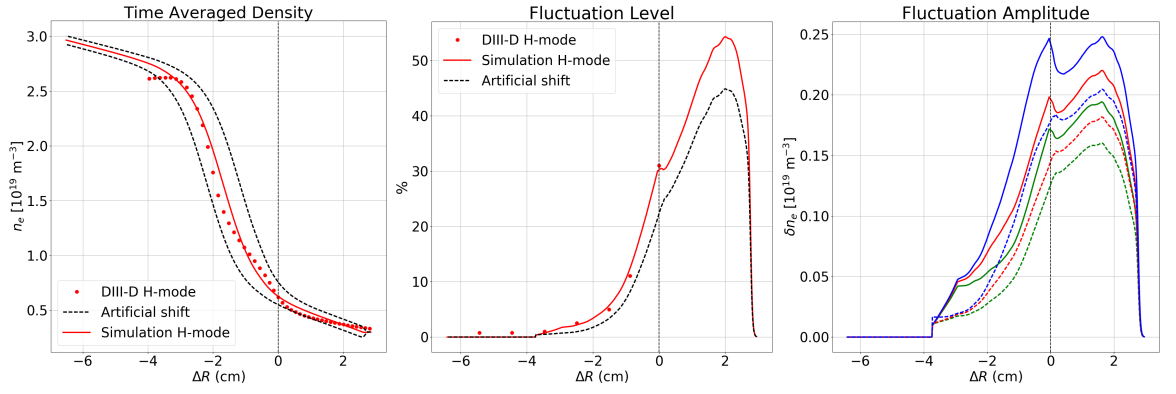


**Figure 5.7:** The left graph shows the scan in spatial resolution from the nominal location in red. The middle graph shows the scan in fluctuation level error where the red line shows the nominal profile. The right graph shows the fluctuation amplitude for the six locations. The colours correspond to the spatial offset where blue represents the density profile closer to the separatrix, red is nominal and green is further away. The solid lines all have the nominal fluctuation level and the dashed lines are lowered by 20%.

Figure 5.7 shows the six simulations within the diagnostic uncertainty space that have been conducted. The scan through spatial resolution is achieved by moving the time averaged density profile by  $\pm 5$  mm about the nominal location. For each of these three locations a simulation is run with the nominal fluctuation level and a subsequent simulation with the profile lowered by 20%. Table 5.3 shows the result for the diagnostic uncertainty. The value used in the broadening prediction is the nominal profile given by the diagnostics corresponding to  $\delta r = 0$  mm and  $\xi_{\text{err}} = 0$ .

	$\delta r = +5$ mm	$\delta r = 0$ mm	$\delta r = -5$ mm
$\xi_{\text{err}} = 0\%$	$\times 1.662 \pm 0.132$	$\times 1.515 \pm 0.102$	$\times 1.292 \pm 0.058$
$\xi_{\text{err}} = -20\%$	$\times 1.403 \pm 0.080$	$\times 1.302 \pm 0.060$	$\times 1.170 \pm 0.034$

**Table 5.3:** The results for the scan in diagnostic uncertainty.  $\xi_{\text{err}}$  is the error in fluctuation level and  $\delta r$  corresponds to a spatial shift relative to the nominal location. Positive  $\delta r$  is a movement towards the separatrix from the nominal and negative the opposite.

A reduction in the fluctuation level profile by 20% causes a decrease in the broadening at the absorption surface by 40%. This is consistent across the scan in spatial resolution. Uncertainty in the spatial location results in an asymmetric change in the calculated broadening. This is expected due to the asymmetric nature of both profiles in space. Moving the density profile by 5 mm results in up to a 50% change in the

background density for the same fluctuation level in the steep density gradient region. Because the background density determines how strongly the wave interacts with the plasma a large change in the scattering is encountered. This results in a change in the predicted broadening at the absorption surface of +30% for movement towards the separatrix (towards larger fluctuations) and -40% for movement away (towards smaller fluctuations).

## 5.5 Discussion

By combining experimental measurements with numerical modelling we have been able to show that the main source of ECRH deposition profile broadening is due to scattering of the beam by density fluctuations occurring solely in the edge region in DIII-D. Though fast particle and diffusive effects will occur they should not contribute more than 10% which is in agreement with previous work [101–103, 110]. Furthermore these diffusive effects contribute even less when the beam is already broadened [105] as is the case here. However, a consistent under-prediction of the broadening of  $\approx 10\%$  is observed in the simulations which is believed to be accounted for by the combination of two sources. Firstly, the fast electron transport is not decoupled from the experimental measurements of the deposition broadening. Secondly, the method for projecting to the absorption region is expected to under-predict the broadening. Both are sources of consistent mismatch between experiment and simulation neither of which are expected to contribute more than 10% and are contained within the respective errors. We have demonstrated the difficulty in modelling H-mode stems from the resolution of the diagnostics. A large change in the calculated beam broadening can occur within the resolution of the diagnostics which accounts for the somewhat diminished agreement found for this scenario. Doubling of the resolution and a reduction of the measurement error to 10% from 20% would be needed to allow for consistent modelling of H-mode. Yet despite the difficulties in making these measurements and matching the simulated plasma profiles to experiment, remarkable agreement with experiment is found across vastly different operating scenarios. It is worth noting that the broadening shown here is only maximised as a negative effect when the normalised poloidal flux,  $\psi_N$ ,

is perpendicular to the absorption surface (see figure 5.1). However if the absorption surface is aligned parallel then the fast parallel transport along field lines will negate the broadening (although it is uncertain how practical this may be in experiment).

Previously beam tracers with a statistical description of the turbulence have been used to calculate the beam broadening for experiments and to predict for ITER [74–78, 103]. However it is not yet clear whether such methods capture the full broadening of the wave. Due to the underlying formalism of the wave mechanics, contributions to the scattering from turbulence structures whose characteristic size is comparable to the wavelength will be missed because these lie outside of the beam tracing code’s region of validity. Moreover, this has been shown to be the precise region where the scattering is maximised [111, 124]. This is of concern for ITER as the beam broadening, which has already been calculated as 100% in these previous studies, could be an underestimation. It should be noted that as explained in section 5.1, this region of 100%-200% broadening is in the limit of operation for fully removing saturated NTMs even with the use of modulation. This is not to say that such a scenario will present itself - only that such codes used to predict the broadening for ITER should be benchmarked on a shot by shot basis to experiment and where also possible, the full wave description for the specific benchmark shot. This will be the subject of the future work which will also consider the requirements for robust ITER beam broadening predictions and the potential for reducing the beam broadening and may be possible without significantly affecting the ITER ECCD design. Additionally, within this work the main contributions to the errors on the modelling which come from the method used to project to the absorption surface will be removed. This will be done by using a ray tracer to trace the beam envelope through the experimentally measured density and magnetic field profiles for the core. Further reduction may be possible by matching the end of the simulation domain to a beam tracer, though this has not yet been considered in detail.



# Chapter 6

## An aside: Experimental investigation of electron transport across a magnetic field barrier in electropositive and electronegative plasmas

The work presented in this chapter has been previously published in:

M.B. Thomas, D. Rafalskyi, T. Lafleur and A. Aanesland: *Plasma Sources Sci. Technol.* **25** 045018 (2016)

©IOP Publishing. Reproduced with permission. All rights reserved.

<http://iopscience.iop.org/article/10.1088/0963-0252/25/4/045018/meta>

### 6.1 Introduction

Charged particle transport across magnetic fields due to  $\mathbf{E} \times \mathbf{B}$  drift is a well-known phenomenon. In the past few decades low temperature plasmas employing a magnetic field have found a wide range of applications. Most notably such plasmas include the Penning trap, Hall effect thrusters, magnetron sputtering for industrial coatings and negative ion beam sources [125–129]. The presence of co-extracted electrons in negative

ion sources, which is unwanted as it decreases the overall power efficiency, is also of significant interest to the development of neutral beam injection systems for magnetic confined fusion reactors [129,130]. The neutral beam injection systems used in magnetic confinement fusion devices implement negative ion sources and require high efficiency for economical application especially with a view to ITER and DEMO [131–133]. It is therefore of interest to decrease the fraction of co-extracted electrons compared to negative ions through increased understanding of drift mechanisms.

In many negative ion sources it is the geometry of the vacuum vessel and shape of the magnetic field that dictates the magnitude and direction of the drift. This magnetic field is usually applied transverse to the plasma source, so that the field lines are perpendicular to the central axis of the device. The plasma interaction with surrounding walls creates sheath and pre-sheath electric fields, which in the absence of externally applied electric fields, combine with the magnetic field to dictate the direction of the drift. Typical geometries are usually rectangular with a magnetic filter provided by a set of permanent magnets [129–132, 134]. Of the plasma diagnostic tools available, Langmuir probes are most widely used [135,136]. This probe gives reliable information on the plasma potential ( $V_p$ ), floating potential ( $V_f$ ), and the current at ground potential ( $I(V = 0)$ ) [135,136]. However these probes have been observed to unavoidably result in perturbations to the surrounding plasma. Non-invasive optical techniques including Thomson scattering and reflectometry are implemented when Langmuir probes are not well suited. However, here a line-of-sight integrated measurement is performed, as distinct from a two-dimensional spatial map of the ion extraction region that is of significant interest for applications [33, 136, 137].

Previous simulation work used 1D fluid models of the detailed chemistry for typical electronegative gases, but needed anomalous transport across the magnetic field with a scaling of  $1/B$  to explain the transport [138,139]. These simulations do not model the transverse walls, and hence no  $\mathbf{E} \times \mathbf{B}$  drift exists. S. Dujko *et al.* [140,141] conducted theoretical simulations of collisional transport and electron drifts on the basis of the ratio of the electron cyclotron to the collision frequency. Their work

provided a database of transport data for future simulations whilst highlighting the need for experimental work on  $\mathbf{E} \times \mathbf{B}$  transport. Work conducted by St Kolev *et al.* [142] provided insight into the charged particle transport in  $\mathbf{E} \times \mathbf{B}$  configurations by means of particle-in-cell (PIC) simulations. The 2D configuration allowed the transverse walls to play a key role showing an  $\mathbf{E} \times \mathbf{B}$  drift thus an anomalous transport is not needed. The simulations focused on low temperature electropositive plasmas in a typical rectangular vacuum vessel with a permanent magnetic field barrier. The results showed significant electron transport across the field to the downstream region on one of the four walls. In this configuration a diamagnetic drift caused by an electron pressure gradient across the magnetic barrier ( $\nabla p_e \times \mathbf{B}$ ) creates a current towards the wall responsible for the  $\mathbf{E} \times \mathbf{B}$  drift across the barrier. This results in an electron current three orders of magnitude higher than collisional transport.

In [143] a 1D wall current probe was proposed and implemented [144] to further study the  $\mathbf{E} \times \mathbf{B}$  drift. This study investigated the scaling of the electron drift with magnetic field strength, and showed a  $1/B$  dependence, proving the origin of the scaling found in [139]. Most recently experimental work on the PEGASES system by Renaud D *et al.* [145] studied the negative ion production and transport in electronegative plasmas. They reveal an anisotropy of the plasma due to a magnetic field induced electron drift. The drift of electrons across magnetic field barriers has yet to be investigated not least due to the lack of experimental work in electronegative plasmas. The degree to which the  $\mathbf{E} \times \mathbf{B}$  drift scales with pressure, whether it can be controlled, and how these electrons behave downstream of the magnetic filter across the extraction plane, are key open questions [143, 144, 146–148].

The chapter is laid out in the following way. Section 6.2 details the development of a two-dimensional array of planar Langmuir probes which spatially resolves the effect of electron drift at the extraction grid. Since the array is positioned downstream of the magnetic barrier, it enables measurement of the electron transport across the magnetic barrier with minimal perturbation to the plasma. In section 6.3 the significance of the electron transport (simulated in Ref. [142]) is experimentally verified.

Beginning with an electropositive argon plasma, section 6.3.1 shows the asymmetry of the floating potential for different plasma pressures. This is extended in section 6.3.2 to an electronegative ion-ion plasma. The origin of the  $\mathbf{E} \times \mathbf{B}$  drift is demonstrated and show an electron drift two orders of magnitude larger than that due to collisional transport. This behaviour is further quantified by showing the dependence on pressure, and the spatial effect over the whole area of the extraction plane.

## 6.2 Experimental set-up

PEGASES, the device used in this study, generates a plasma by inductively coupling RF power by means of an 8-turn antenna (operated at 4 MHz), embedded in ferrite, as shown in figure 6.1 [149]. PEGASES has dimensions of  $135 \times 130 \times 90$  mm (x, y, z) and employs a magnetic field to confine the electrons in the plasma heating region. Used in conjunction with an electronegative gas, this magnetic field also leads to a stratification of the plasma with a downstream region where the electron density is 3 orders of magnitude lower than the positive and negative ion densities, resulting in an ion-ion plasma [150]. As such PEGASES represents a new concept in plasma thruster technology [151].

Using the ion-ion source, a gridded extraction system is then able to successively accelerate positive and negative ions, thus removing the need for a downstream neutraliser [149, 151, 152]. The duty cycle of the square wave voltage applied to the extraction grids can be varied to ensure equal positive and negative ion extraction, thus the thruster does not charge up. The geometry of PEGASES closely resembles the simulation model used in Ref. [142], whilst also demonstrating an attractive negative ion source, and as such is highly suited to this study.

In PEGASES (figure 6.1), the schematic view is from the top thus showing magnetic north with south being on the reverse. There are no external electric fields applied to PEGASES; rather they are all internally generated in the plasma pre-sheath and sheath regions to ensure equality of charged particle fluxes at the boundaries. The electric field as shown, located in the plasma sheaths and pre-sheaths, is directed towards

the wall in the vacuum vessel. It follows that with the addition of a magnetic field in the configuration of PEGASES, there are 2 walls where the fields are perpendicular and thus produce a drift (the electric field in the bulk plasma in the  $x$ -direction is assumed negligible). The drift across the magnetic field will be in the positive  $x$ -direction on the right hand side wall when looking from the RF source (upstream) to the extraction grid (downstream) as shown. One can define a reduced electric field value in the pre sheath as  $E/N \approx 730$  Td and magnetic field of  $B/N \approx 5.55 \times 10^5$  Hx within the magnetic barrier and  $B/N \approx 2.22 \times 10^4$  Hx near the grids in the downstream region (1 Td =  $10^{-21}$  Vm<sup>2</sup>, 1 Hx =  $10^{-27}$  Tm<sup>3</sup>). The system is therefore heavily magnetic field dominated where the cyclotron frequency for electrons is orders of magnitude larger than the collision frequency.

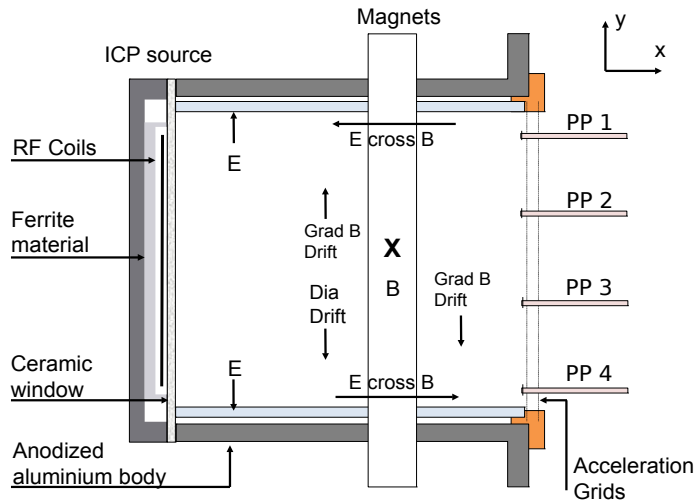


**Figure 6.1:** Schematic of the PEGASES plasma source as viewed from the top. The downstream region is to the right of the magnetic field, the upstream to the left. The magnetic field is into the page and consequent drift directions are illustrated with arrows across the magnet. PP 1 - 4 approximates 4 probe locations of the array. The diamagnetic drift is denoted by “Dia Drift” and the  $\nabla\mathbf{B}$  drift is denoted “Grad B Drift”. Drifts are labelled for negative charges only.

The  $\nabla\mathbf{B}$  drift is present at two locations. In the upstream region it points in the positive  $\hat{y}$  direction (upwards) acting against seeding the right hand side wall responsible for the  $\mathbf{E} \times \mathbf{B}$  drift. However, this drift is orders of magnitude less than the diamagnetic drift thus leading to a net drift towards the transport wall. In the downstream region the  $\nabla\mathbf{B}$  drift points in the negative  $\hat{y}$  direction (downwards). However, the electron population in the downstream region is 3 orders of magnitude smaller than

the upstream region; therefore the flux of electrons from the  $\nabla\mathbf{B}$  drift at this location is also negligible. Because of the geometry of the permanent magnets used, and because the plasma region is contained between the ends of the magnets, the magnetic field is approximately uniform in the  $y$ -direction in the plasma (so that  $B_y = 0$  and  $dB_y/dy = 0$ ), thus there is no  $\nabla\mathbf{B}$  drift in the  $x$ -plane to produce cross field transport.

It is noted that a diamagnetic drift is theoretically present in the plasma sheath and points in the opposite direction to  $\mathbf{E} \times \mathbf{B}$ . As discussed in [153] and [142], the diamagnetic drift is dependent on the gradient of the electron density and temperature. Because it is a fluid drift and thus a result of averaging, it does not necessarily correspond to real particle drifts. The diamagnetic drift is dominant in the upstream region due to the high density of particles and strong temperature gradients. This is not the case in the sheath. Therefore despite there being a fluid drift in the opposite direction to the  $\mathbf{E} \times \mathbf{B}$  drift, it does not correspond to a strong effect and single particle drifts dominate. Therefore the diamagnetic drift in the sheath is not expected to affect transport. Another potential mechanism affecting transport is the formation of double layers. Previous studies of the PEGASES system using Langmuir probes and energy analysers find no evidence for a double layer within the source [154]. Therefore this is also not considered to affect the transport.

PEGASES was operated with an RF power of 200 W, of which 150 W is coupled to the plasma during operation with argon, and 100 W during operation with Ar-SF<sub>6</sub>. The Ar and SF<sub>6</sub> gases are injected along the source axis using 16 holes distributed on both sides of the source. The chamber is pumped by a turbo-molecular pump providing a residual pressure better than  $5 \times 10^{-5}$  Torr. The magnetic field is kept at the same position centred 35 mm from the extraction grid, and separated by 90 mm. Each permanent neodymium magnet has a remnant magnetic field density of about 1.17 Tesla, which produces a peak field of around 250 G at a width of 40 mm in the centre of the separation.

### 6.2.1 Probe design

For this study it is necessary to develop a picture of the plasma dynamics due to electron transport in the whole cross sectional area of the downstream plasma at the extraction point. To achieve this a novel probe system comprised of a 2D array of 16 planar Langmuir probes, each with a radius of 1.8 mm, was designed. One of the acceleration grids (made of a stainless steel alloy) was used to secure the 16 planar probes in an array distributed as shown in figure 6.2, which is then secured in the downstream region and grounded as shown in figure 6.1. The probes are made of M2.5 brass screws which have vacuum safe Teflon insulated wire soldered to the bottom. They are then nested in Teflon tubing for insulation before being fixed in the holes of the grid (figure 6.3). Each probe is biased individually to produce I-V characteristics. The error on the I-V curve acquisition as quoted by the manufacturer is  $\pm 0.5$  Volts and  $\pm 1.5 \times 10^{-6}$  Amps. The error on the probe collecting area is  $\pm 1 \times 10^{-6}$  m<sup>2</sup>.

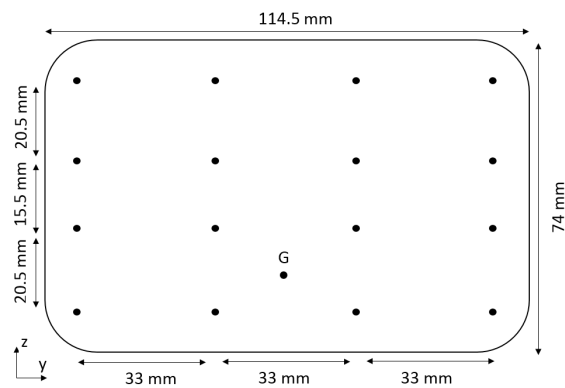


**Figure 6.2:** Diagram of the probe array on the grid. G is the ground connection and each black dot is a planar Langmuir probe as shown in figure 6.3.

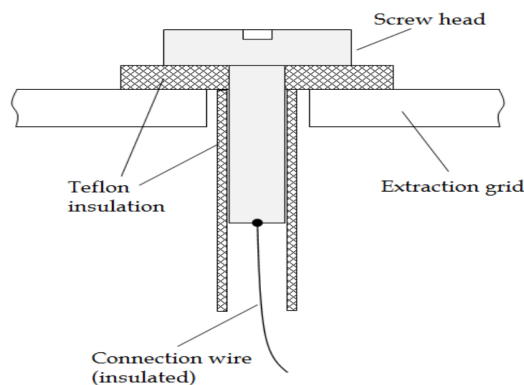


**Figure 6.3:** Diagram of one of the Langmuir probes in the array shown in figure 6.2.

To enable further understanding of the probe measurements a magnetic field map was generated using COMSOL multiphysics modelling software [155]. The magnetic field map (figure 6.4) shows that the field lines are perpendicular to the probes at the top and the bottom of the array ( $z$ -axis) with an x-point present in the centre. This is an ideal configuration as it means that all field lines intersect the probes at right angles and so the Larmour orbit will not inhibit collection of charged particles. Thus all electrons are able to follow along the field lines and be collected. Furthermore we are able to conclude that the magnetic field geometry alone is not expected to pose any asymmetry in the measurements.

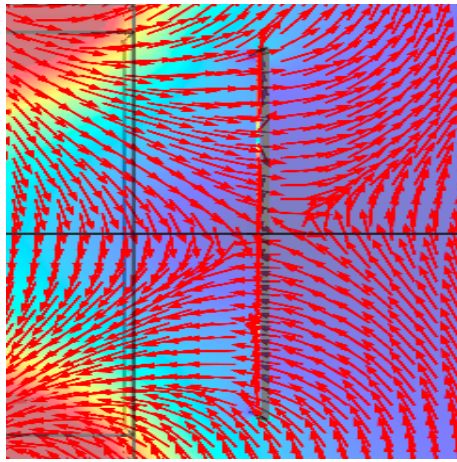
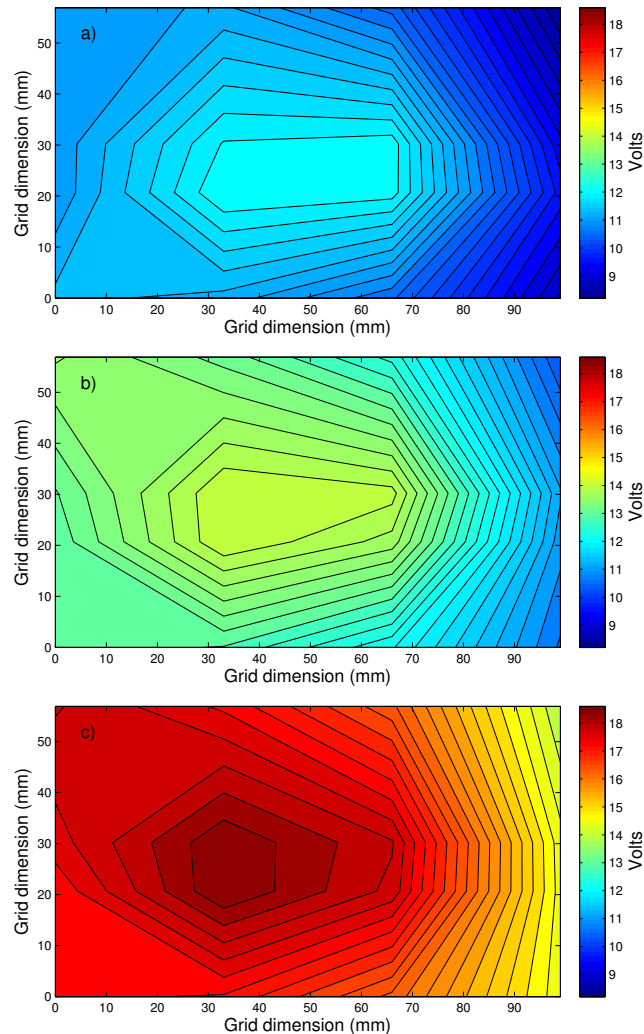


**Figure 6.4:** Magnetic field map as viewed from the  $x$ - $z$  plane in figure 6.1 (vertical  $z$ -axis, horizontal  $y$ -axis). The 2D probe array is the vertical black line in the centre of the image.

## 6.3 Results

Two kinds of plasmas, electropositive Ar, and electronegative Ar-SF<sub>6</sub>, were used to gain experimental data at 3 different pressures. Ar-SF<sub>6</sub> was used with a flow rate ratio of 1:1 SCCM (standard cubic centimetres per minute). Three measurements were taken at the lowest, median, and maximum flow rates (flow rates bounded by the stability of the plasma). These correspond to Ar flow rates of 10, 30, and 50 SCCM, and Ar-SF<sub>6</sub> flow rates of 5, 10, and 15 SCCM. The absolute pressures for these flow rates are between 0.6 to 3 mTorr.

### 6.3.1 Argon



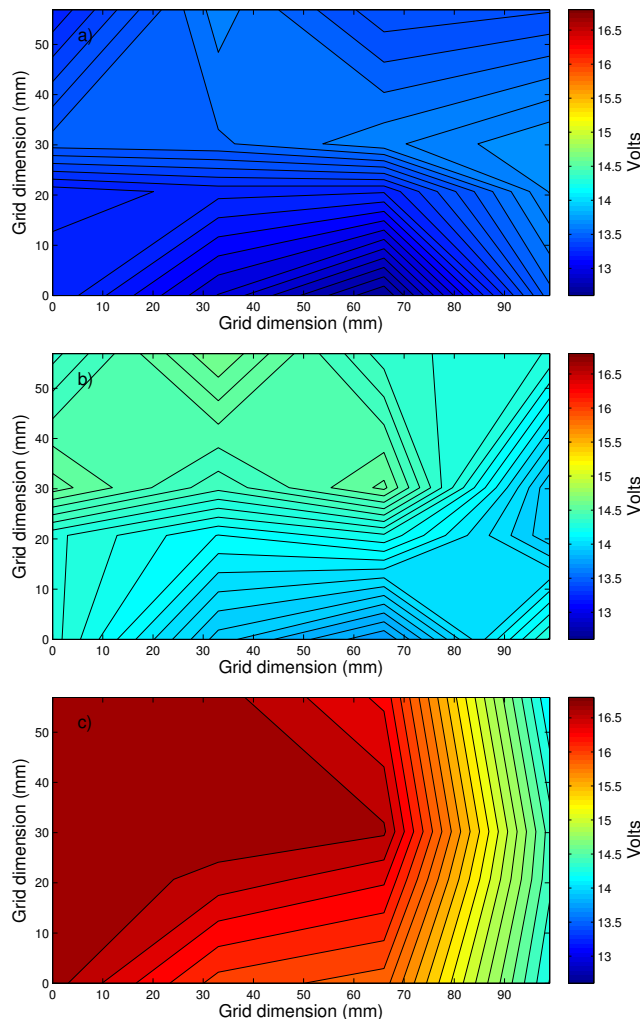
**Figure 6.5:** spatial variation in floating potential over the extraction grid in argon. a) 3.06 mTorr (50 SCCM), b) 1.88 mTorr (30 SCCM) and c) 0.67 mTorr (10 SCCM). The magnetic field direction (taken from figure 6.4) points uniformly directly into the page in the top half of each contour graph and uniformly directly out of the page in the bottom half. The orientation of the contour maps are as though the reader is looking from the upstream ICP source to the probe array downstream (see figure 6.1). This is the same for all subsequent contour maps of the probe array.

Figure 6.5 shows the floating potential spatial distribution in argon for the three flow rates tested. The drop in floating potential on the right side of the probe array is observed due to the electron drift expected to be on the right side chamber wall. This is indicative of a larger quantity of electrons as the probe must float to a lower potential to further repel electrons and hence to ensure equal currents of electrons and ions. The drift is evident at all three pressures though the voltage difference from the centre of the extraction grid to the right wall is similar for all pressures: 6.5(a)  $2 \pm 0.5$ , 6.5(b)

$2.5 \pm 0.5$ , 6.5(c)  $3 \pm 0.5$  V, respectively. The change of pressure manifests as both an increase in the magnitude of the floating potential, and a slight increase in the potential drop from the centre to the edge of the extraction grid.

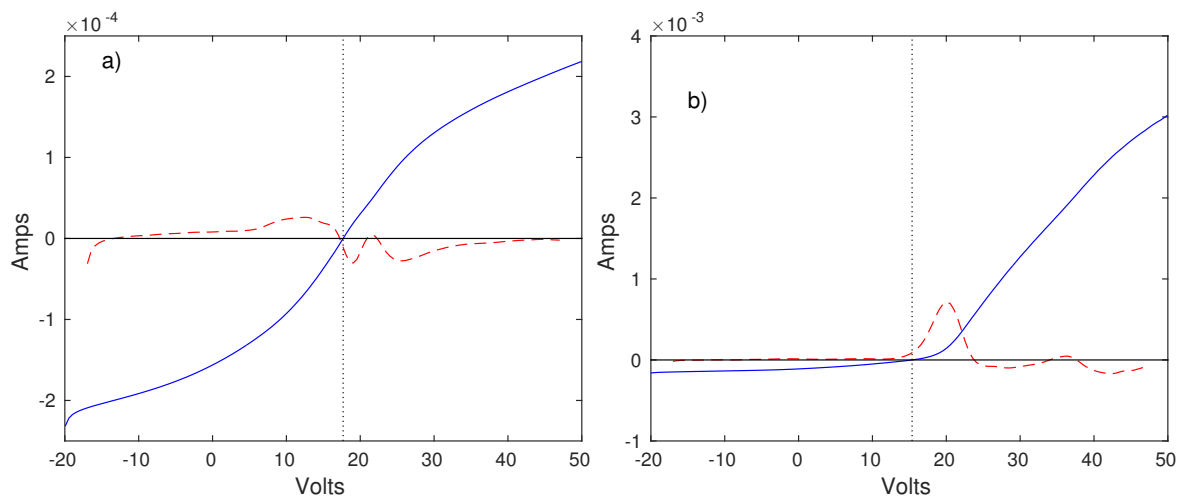
### 6.3.2 Ar-SF<sub>6</sub>

Figure 6.6 shows a map of  $V_f$  in Ar-SF<sub>6</sub> over the three pressures. The lowest pressure shows a sharp reduction of the potential by 3 volts from the centre of the extraction grid to the edge. This is in accordance with the predicted electron drift location of the right wall (looking from the RF power coupling to the extraction grid). However, unlike in argon it is observed that the voltage on the right side remains constant at 14 V within the errors of  $\pm 0.5$  V throughout all pressures. It is the remaining area of the extraction grid that increases in  $V_f$  as one tends to lower pressures.



**Figure 6.6:** spatial variation in floating potential over the extraction grid in Ar-SF<sub>6</sub>. a) 2.54 mTorr (15 SCCM), b) 1.87 mTorr (10 SCCM) and c) 1.10 mTorr (5 SCCM).

Note that the larger two pressures produce a relatively homogeneous potential. This homogeneity is unique to an electronegative plasma and does not occur in electropositive argon (section 6.3.1). Furthermore, the spatial variation of the floating potential is observed to exhibit consistent qualitative trends dependent on pressure. This is distinct from the behaviour of the electropositive argon plasma shown previously in figure 6.5. At higher pressures the increased electron collision frequency most likely leads to increased attachment to neutral  $\text{SF}_6$  molecules, thus creating more negative ions and reducing the electron current (and effect of the  $\mathbf{E} \times \mathbf{B}$  drift) at the grid.



**Figure 6.7:** a) Central extraction grid at co-ordinates (33, 20.5) mm b) the right side wall at co-ordinates (99, 20.5) mm demonstrating electron drift at a pressure of 1.10 mTorr. The red dotted line is the second derivative, black dotted line is the floating potential and the blue dotted line is the Langmuir I-V curve. Note the increase in magnitude of the current from a) to b).

Further inspection of the I-V curves is needed to fully quantify the magnitude of the electron drift. Figure 6.7 shows the I-V curves taken from selected positions of the probe array at co-ordinates (33, 20.5) mm and (99, 20.5) mm (see figures 6.2 and 6.6) at a pressure of 1.10 mTorr. Figure 6.7b) has the observed shape of the 4 probes along the right wall and displays the expected shape of a plasma where the dynamics are governed by positive ions and electrons (i.e. a significantly larger current in the electron portion of the curve). Figure 6.7a) displays a shape symmetric about  $I = 0$  and  $V_f$  (vertical dashed line) and consistent behaviour is observed on the 12 probes across the remaining area of the extraction grid. This is characteristic of an ion-ion plasma [150]. Unlike an electropositive plasma, the dynamics are dominated by the

positive and negative ions. There is a deficiency of electrons due to the attachment to the electronegative neutrals as discussed in section 6.2. The ratio of the positive-to-negative ion mass,  $M(\text{Ion}^+)/M(\text{Ion}^-)$ , is much smaller compared with the ratio of positive ion-to-electron mass,  $M(\text{Ion}^+)/M(e^-)$ , which leads to  $V_f \rightarrow V_p$  (obtained where the second derivative, red dashed line, is equal to zero), and the symmetric shape observed.

The dominant positive ions (as shown by Refs. [145, 156]) in an Ar-SF<sub>6</sub> plasma at a ratio of 50:50 and low pressure are Ar<sup>+</sup> and SF<sub>3</sub><sup>+</sup> with a smaller SF<sub>5</sub><sup>+</sup> contribution. The dominant negative ions (as shown by Refs. [145, 157]) are F<sup>-</sup> and SF<sub>6</sub><sup>-</sup> with a smaller SF<sub>5</sub><sup>-</sup> contribution. The average positive and negative ion mass is therefore approximately equivalent along with their respective temperatures. When the probe reaches the plasma potential, it is expected that no ions are repelled from the probe, and because their densities are equal (to satisfy quasi-neutrality), their collected current contributions would also be equal. Thus one would expect a measured current of zero with negligible electron contribution. The fact that this is not the case in figure 6.7b) indicates that there are still a significant number of electrons present, and their current can thus be estimated as the value observed when the probe is biased to the plasma potential.

It is noted that these assumptions are estimates and that the average mass and temperature are not exactly the same but rather very close. Our method would therefore over estimate or underestimate depending on the exact temperatures and masses. Exact error calculations in whether there was an over or under estimate could only be made if we knew the exact dominances of positive and negative ions and respective temperatures. Though these errors are not expected to be significant. The ion currents for ion-ion are roughly:  $I_+ \approx \sqrt{T_+/M_+}$ , and  $I_- \approx \sqrt{T_-/M_-}$ , thus  $I_-/I_+ \approx \sqrt{T_- M_+/T_+ M_-}$ . Since  $T_- \approx T_+$ , the only way one could explain the large asymmetry in 6.7b) would be if  $M_+/M_- > 100$ , which is clearly not possible. Thus the asymmetry must be due to electrons. This electron current contribution is shown in figures 6.8a) - 6.8c). In order to complete the explanation for the mechanism of the  $\mathbf{E} \times \mathbf{B}$  drift, the polarity of the magnetic field was flipped. The electron current density

map for this configuration, at a pressure of 1.10 mTorr, is shown in 6.9. One can see that the electron flux is switched now to the left wall; the expected wall to produce an  $\mathbf{E} \times \mathbf{B}$  drift with a reversed polarity magnetic field. This confirms the mechanism for the  $\mathbf{E} \times \mathbf{B}$  drift to be the interaction of the external magnetic field and the wall sheath.

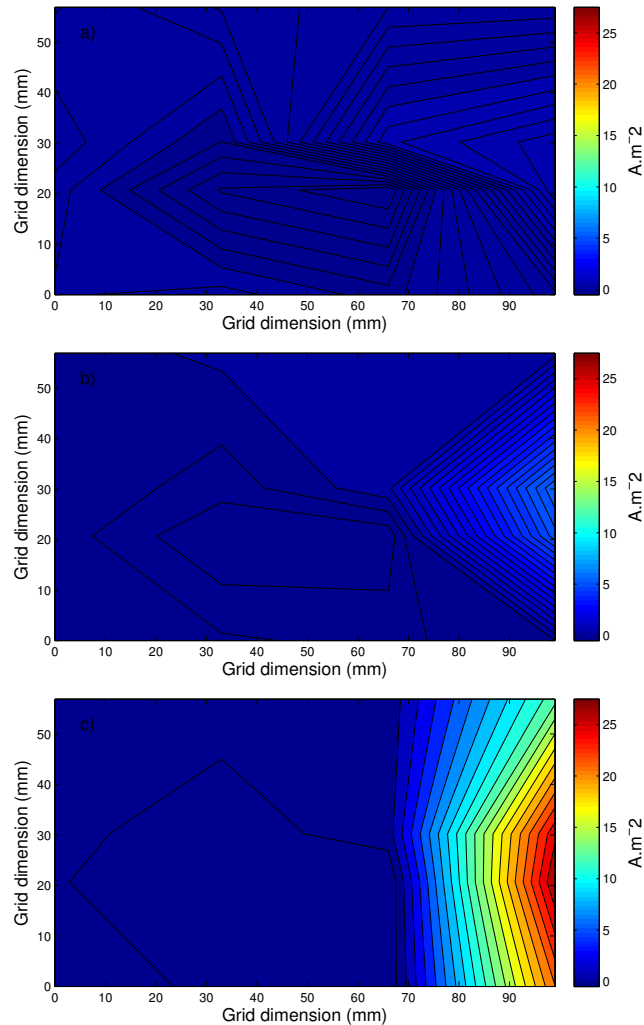


**Figure 6.8:** spatial variation in electron current density over the extraction grid in Ar-SF<sub>6</sub>. From top to bottom: 2.54 mTorr, 1.87 mTorr and 1.10 mTorr.

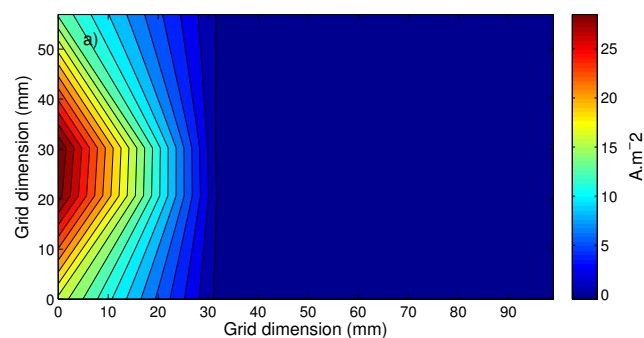


**Figure 6.9:** Electron current density map in Ar-SF<sub>6</sub> at a pressure of 1.10 mTorr with a reversed polarity magnetic field.

Figure 6.8 further demonstrates the homogeneity of the current density at higher pressures and demonstrates the manner in which the drift strength grows. The drift fraction appears to be stronger in the middle of the right wall. This is most likely a consequence of diffusion and losses on the boundaries, which would yield the lowest density at the corners. It is reasonable to take an average over the 4 probes in the vertical  $z$ -axis at each location along the horizontal  $y$ -axis. This illustrates the magnitude of the electron current density at each location in  $y$ . Hence, figure 6.10 can be thought of as a means to observe the extent to which the  $\mathbf{E} \times \mathbf{B}$  drift influences the rest of the extraction grid.

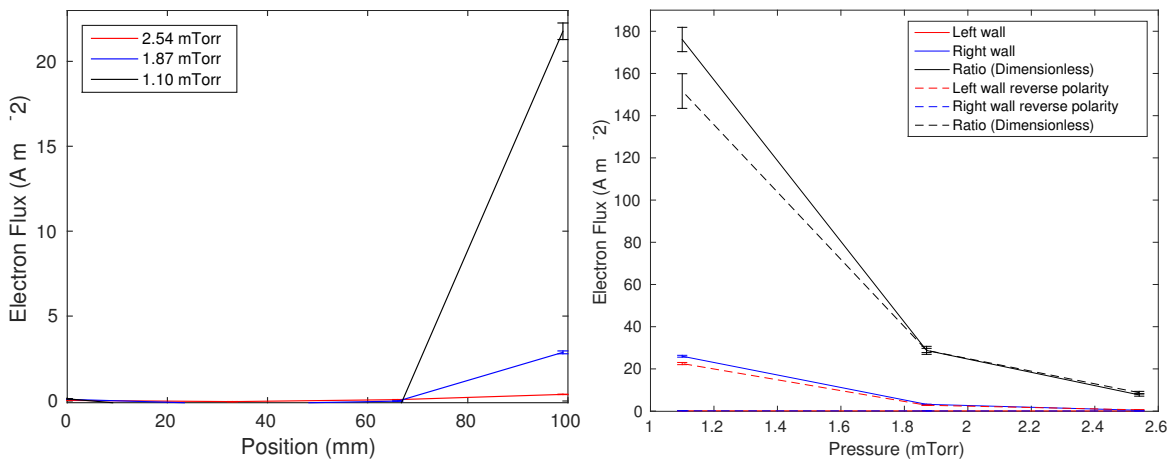


**Figure 6.10:** Left: Dependency of the electron drift with pressure and position across the extraction grid. Right: Variation of the electron drift with pressure. Displaying the electron flux ( $\text{A m}^{-2}$ ) given by the average of the 4 current probes on the right wall (blue) and left wall (red). The dimensionless drift current ratio is in black. Also shown is the reverse polarity magnetic field case.

The drift is confined to the right wall and is only observed on the 4 probes at this wall. Higher spatial resolution in this area is needed to reveal the behaviour of the drift magnitude as a function of position. However from this analysis, one can identify an upper bound on the influence of the drift from the wall to the centre. The next nearest neighbours to the wall probes do not show any electron drift influence. As a linear interpolation is used we can conclude that in the worst case at low pressure the drift has an influence up to 30% of the extraction area from the right wall to the centre. Most likely the drift influence region is much smaller than this and follows some power law rather than the linear interpolation here, but this is consistent with previous observations in the PEGASES system [148]. It is clear that the drift is significantly

reduced at higher pressures. In order to quantify the drift fraction we calculate the ratio of the average current density collected by the 4 left wall probes and the 4 right wall probes.

Figure 6.10 displays the dependency of the drift with pressure increase; also included is the data for the reversed polarity magnetic field. Note that in both field configurations the wall corresponding to the drift in the direction of the extraction grid displays an increase in measured drift electrons with reduction in pressure. This is the right wall (blue line) for the original set-up, and the left wall (red dotted line) for the reversed polarity magnetic field. However the wall with drift direction away from the extraction grid shows a relatively constant measured electron flux at all pressures. This shows that the homogeneity at higher pressure found in figure 6.6 cannot be due to increased collisional transport as this does not become comparable to the  $\mathbf{E} \times \mathbf{B}$  drift. This is observed theoretically by Dujko S *et al.* [140] which found that the collision frequency is expected to have a small effect on transport coefficients and that the strong magnetic field greatly reduces the diffusion transport coefficients in the  $\mathbf{E} \times \mathbf{B}$  direction. Moreover the homogeneity is not observed in argon; therefore this must be due to the nature of the electronegativity of Ar-SF<sub>6</sub> as previously discussed (i.e. the electron attachment rate most likely increases at higher pressures, hence reducing the drift effect). It is found in both cases that the drift fraction is one order of magnitude at 2.54 mTorr and 2 orders of magnitude at 1.10 mTorr. These are the maximum and minimum pressures attainable in PEGASES as discussed in 6.3.

The above results are in agreement with the simulation in Ref. [142], and the experimental work in Refs. [143, 144]. The previous work on the PEGASES thruster by Ref. [145] also revealed this anisotropy. Therefore we confirm the mechanism of the drift to be  $\mathbf{E} \times \mathbf{B}$  and further this research by parametrising the drift fraction and location. For direct comparison with Ref. [142], the magnetic field width here is twice as large with a peak field 5 times as strong. It was found by [142–144] that the scaling of the drift with magnetic field strength is  $I \propto 1/B$  (not  $1/B^2$  as expected from classical diffusion) and the drift fraction reduces monotonically with magnetic barrier width. It follows that the drift fraction here should be more than 5 times less. Indeed

it is found that the drift fraction at comparable pressures is found to be 2 orders of magnitude as opposed to 3 orders of magnitude. Given that the species modelled in Ref. [142] was  $\text{H}_2$  and not  $\text{Ar-SF}_6$ , this is in excellent agreement with the  $1/B$  scaling law [138, 144].

From figure 6.10 it is clear that the reduced asymmetry at high pressure is the most favourable operation for a negative ion source. Although asymmetry is still present with a drift magnitude 1 order of magnitude larger than collisional transport, figure 6.10 (left) suggests that the extent to which this drift influences the extraction area would also be greatly reduced. Thus this could lead to more efficient and uniform negative ion sources.

## 6.4 Conclusions

In this study three key points are addressed as a function of pressure: (a) the drift fraction of electrons as a ratio of the electron flux at the two drift walls, (b) the extent of the drift influence across the area of the extraction grid, (c) the effect electronegativity has on the drift. Experimental observation of the  $\mathbf{E} \times \mathbf{B}$  drift across the area of the extraction grid has verified the mechanism of the drift to be the interaction of the wall sheath and presheath electric fields with the applied magnetic field barrier. A drift fraction of 2 orders of magnitude larger than collisional transport was observed, which is in agreement with the PIC simulations in Ref. [142], and the scaling law found by other experimental studies [143, 144].

Differences between the behaviour of an electronegative and an electropositive plasma with pressure were found. An electronegative plasma produces a relatively homogeneous profile at moderate to high pressures, contrary to electropositive plasmas, where electron drift effects remain significant. As discussed in section 6.3.2, the increase in collision frequency probably reduces the electron density (and hence electron current) due to increased electron-neutral attachment. This electronegative behaviour leads to a reduction in the drift fraction by an order of magnitude and also reduces the area of the extraction grid influenced by the electron drift. For negative ion sources it follows

that the regime of operation providing the least contamination by the drift and least asymmetry would be one with higher pressures, and stronger magnetic fields. Though it is noted that though higher pressures are possible in PEGASES, there exists a limit to the pressure attainable in low temperature electronegative plasmas that has not been investigated here.

The lowest attainable pressure resulted in the highest influence of the drift across the extraction area. This was 30%, though it is noted that this is an upper bound and most likely is less than this. Furthermore this fraction reduces with pressure. Further work will aim to provide higher spatial resolution of the extraction grid at the drift side to further quantify the behaviour of the drift fraction with position.



# Chapter 7

## Conclusions and future work

### 7.1 Summary

The fundamental objective of the Ph.D. has been to solve physics problems. To do so has required the development of EMIT-3D to create a fully parallelised, versatile, full wave code: one which can be applied to a diverse range of problems including the specific case of modelling the SAMI diagnostic in a spherical tokamak geometry. To this end a large portion of the Ph.D. was spent in code development. Following this the main objective shifted to using EMIT-3D to advance the knowledge of the field of microwave interaction with turbulence which was achieved via two distinct but connected projects.

The first project was to uncover the previously unknown fundamental scaling law dependencies of scattering through turbulence. This was achieved via a parameter scan of the plasma turbulence and RF beam parameter space. The work focused solely on O-mode propagation and for that reason the magnetic field for each case was selected to ensure that O-mode was the only solution in the domain. The parameter space included the plasma turbulence variables of correlation length and RMS fluctuation level, the background plasma density, the propagation distance and the beam waist size.

The second project was to directly model the ECRH beam propagating through the edge plasma on DIII-D for specific shots. The DIII-D diagnostics were used to

constrain the characteristics of the modelled plasma turbulence for each shot and the experimental beam parameters were used to initialise the modelled beam. The purpose was to investigate whether the hypotheses made by experimental work that ECRH deposition profile broadening is due to scattering of the ECRH beam in the edge could be shown to be correct through modelling of the experiment. Three distinct operating scenarios, L-Mode, H-Mode and L-Mode negative triangularity were chosen intentionally due to their vastly differing edge turbulence characteristics. The reasoning for this was to increase confidence that the result of the modelling was not case specific and in fact a true prediction which could be repeated.

A third research project, which has not reached its conclusion aims to use EMIT-3D to model SAMI in 3D on MAST to enable the extraction of a rotation velocity from the experimental data. The project required a large amount of code development and benchmarking and has yielded only preliminary results so far. Therefore the decision was taken to present the code development and benchmarking and the preliminary results within chapter 3 on EMIT-3D. The outline of the project plan will be presented in future work.

A large focus of the Fusion Doctoral Training Network (FDTN) is to train Ph.D. students to have a wider range of knowledge of fusion and plasma physics through the taught courses and the collaborative research project. To this end the work from the collaborative research, which falls under the same funding as the rest of this thesis yet does not fall within the scope of the main research, is presented in chapter 6 as an aside. The research area was in the field of experimental, low temperature plasma physics and details work towards the optimisation of a novel plasma thruster for space applications. A Langmuir probe array diagnostic was designed, built, tested and then used to gather information on the plasma at the extraction point which creates the thrust. The purpose was to determine the origin of the asymmetric thrust which had been previously observed and to quantify its characteristics with the view to reducing the overall asymmetry and therefore potentially increasing the efficiency of the device.

## 7.2 Conclusions

This thesis has shown significant development of the original EMIT-3D code. The largest and most important change, which necessitated re-writing of the entire code (now written in C from C++), was to parallelise in three dimensions instead of one. The modification aimed to vastly improve the codes scalability. The performance scaling shows that increasing the number of cores by 2 decreases the run time by approximately the same factor up to a limit where the ratio of ghost cells to computational cells per core is  $> 12\%$ . Furthermore, optimisations of the numerical method have resulted in a 100% speed increase from the previous version. A new method for dealing with the boundary conditions has been implemented and found to result in reflections of wave power of approximately  $10^{-8}$  of the incoming wave. An improvement of 4 orders of magnitude on the previous version. A new soft-source phased array antenna allows for reflectometry simulations to be carried out. The soft source makes the antenna transparent to the reflected waves and phasing the array allows full control of the orientation of the beam in 3D. A range of options are available to include analytic density profiles of any orientation or to read in turbulence simulation data from a NetCDF file. EMIT-3D has the ability to model the SAMI diagnostic on MAST-U or NSTX-U. The view of SAMI is matched as closely as possible to the experiment by implementing a curved inhomogeneous magnetic field profile from EFIT for the specific shot and overlaying the chosen analytical density functions or turbulence data. The density may be moved in time through an interpolation routine to model Doppler reflectometry. The development stage has passed numerous benchmarking and stability tests. The result is a versatile 3D code with the unique ability to model Doppler reflectometry in 3D tokamak geometry on a shot by shot basis.

The first research project found fundamental scaling laws which govern the dependence of scattering on the turbulence characteristics. By changing the ratio between wavelength and correlation length it was found that a peak scattering occurred at a correlation length of  $0.52\lambda_0$ . The peak scattering occurs at  $0.52\lambda_0$  instead of  $1\lambda_0$  because the correlation length is defined as the average distance over which the normalised au-

to correlation falls off to 0.5 which corresponds to an average eddy radius. It was shown that the scattering scales as a power law with fluctuation level as a near quadratic of the form  $\alpha = 1 \times 10^{-3} \sigma^{1.9}$ . Furthermore this is true for the entire range of correlation lengths therefore demonstrating that the dependence of scattering on correlation length is independent of fluctuation level. The largest contribution to the scattering power of the turbulence is the average background plasma density onto which the turbulence is superimposed. Increasing the plasma density by 5 times increases the scattering by 50. However, a parameter scan through this space has not been conducted and a trend has not been defined. One particularly useful result from a modelling view point is the dependence of scattering on the initial beam waist. It was found that the broadening asymptotes to a constant value after the beam waist reaches a value of  $\sim 5$ . This allows a theorist to model an experimental beam which usually has a very large waist with a beam with a much narrower waist and retain the same scattering physics, which significantly reduces computational expense.

The second research project was able to show conclusively that the experimentally measured ECRH deposition profile broadening was due to scattering of the ECRH beam as it propagated through the edge region of the tokamak plasma. The crucial aspect of these simulations is that the simulation parameters are rigid and the simulation plasma domain is initialised by the tokamak diagnostics. Therefore there were no control parameters to change in order to try to match to the experimental result post simulation. The turbulence characteristics were set by the diagnostics on DIII-D for each specific shot and the beam was initialised to the experimental ECRH beam. The predictions of the ECRH broadening by EMIT-3D agree with experiment exceptionally well to within 10% and with small error bars of 20%. Furthermore, because the agreement covers 3 different operating scenarios with different edge turbulence characteristics and absorption locations the confidence in the robustness of results is high. It has therefore been demonstrated that using this method has high confidence in future predictions for beam broadening in any operating scenario in DIII-D.

The collaborative research project provided an answer to the origin of the asym-

metric particle extraction observed in previous work. The asymmetric extraction was due to an  $\mathbf{E} \times \mathbf{B}$  drift of electrons due to the interaction between the plasma wall sheath and the homogeneous magnetic field used for electron cooling and stratification. The drift was found to be 2 orders of magnitude larger than collisional transport and directed towards the extraction plate on one wall and away from the extraction grid on the other. Increasing either the pressure or the magnetic field was found to reduce the fraction of the extraction plate that was contaminated by the drift. Furthermore electronegative plasmas were found to not only reduce the drift fraction by 1 order of magnitude but also reduce the area of the extraction grid contaminated by the drift. This was attributed to an increase in collision frequency which reduces the electron current and leads to an increase in electron-neutral attachment.

## 7.3 Future work

### 7.3.1 Project 1: Prediction of ECCD beam broadening and cross polarisation scattering in ITER

The long term goal of the beam broadening research project is to produce a method which can robustly predict the beam broadening on any tokamak for any operating scenario. In order to achieve this goal, the method will need to be refined in the following way. The method for propagating to the absorption location will need to use a ray tracing code to include the refractive effects of the core plasma and magnetic field. This will reduce the error by 10%. If one is able to do this via attaching a beam tracing code to the end of EMIT-3D a further reduction in the error of 7% will be achieved by removing the need to fit ray lines to the beam envelope. There will still be the inherent uncertainties from the diagnostics which affect the prediction and the discrepancy in the position of the launcher and the diagnostic channels, though it is unclear how this can be resolved. This can only be improved by improving the robustness of global turbulence models to predict the turbulence at different poloidal angles. In addition, the next project should be undertaken as a collaboration between different tokamaks to demonstrate if the method will work across a large range of fusion plasmas. This

should also include a collaboration with beam tracing codes that include a statistical model of turbulence, on a direct comparison basis, to reveal whether the beam tracing codes can predict the entire beam broadening or not and therefore whether they can be used in these calculations. Finally, pending the results of this research the next project should look to directly predict the beam broadening that could be expected on ITER.

### **7.3.2 Project 2: 3D Doppler reflectometry simulations for SAMI**

Further simulations will be conducted to better understand the results of the broad-beam, slab turbulence, Doppler reflectometry simulations. This will include using an analytic description of the turbulence with two and then three discrete values of corrugation wavelengths superimposed on top of each other. These will be used to confirm the current explanation for the under-prediction of the plasma velocity. Simulations of SAMI on MAST will then be carried out with the modelled magnetic field provided by EFIT, the background density profile provided by Thomson scattering and the launch antenna matched to experiment. The variable will be the analytical turbulence that will be superimposed on top of the background density profile which provides the back scatter. By scanning through the turbulence characteristics for correlation length and fluctuation level the experimental data which includes the combination of all these effects may be de-constructed and a rotation velocity found.

### **7.3.3 Project 3: Inclusion of an option to turn on background current density and magnetic shear**

The physics of O-X mode conversion in the presence of strong magnetic shear is not well understood. The O-X-B mode conversion is a commonly used technique to create EBW's in an over dense spherical tokamak which can propagate to the core region to heat the plasma. Moreover, the reverse process may be used to provide a wealth of information from the core plasma through the use of passive diagnostics. In a spherical tokamak there exists large magnetic shear in the edge region where the O mode cut-off

surface and therefore the conversion surface is located for the frequencies used in O-X-B mode conversion. The wave group velocity decreases rapidly near a cut-off and will become comparable to the electron fluid flow velocity (which carries the current) over a relatively large distance if the background current density is also large. With this in mind it is necessary to include terms which involve the background current density or the electron fluid flow velocity in the plasma response. In chapter 2 section 2.2.2.1, the derivation of the plasma response was shown and explanations given for terms that were negligible. By including magnetic shear, three more terms are now present in the plasma response equation and one more term in the current density substitution which results in a vastly more complicated expression, the derivation of which is shown in Appendix 1. The next step will be to find a discretised update equation for  $\mathbf{J}_1$  which can be included as an option in EMIT-3D. It is necessary for this to be included as an option so then EMIT-3D does not incur unnecessary extra computational expense (caused by the extra terms) when magnetic shear is not turned on or if the simulation parameters are away from a cut-off.



# Appendix 1 - Derivation of current density evolution equation with the inclusion of magnetic shear

To begin, one starts with the equations for the current density and the force balance equation found in chapter 2 before any assumptions have been made regarding the background current density.

$$\begin{aligned}
 \mathbf{J}_0 &= -en_0\mathbf{v}_0 \\
 \mathbf{J}_1 &= -e(n_0\mathbf{v}_1 + n_1\mathbf{v}_0) \\
 \frac{\partial\mathbf{J}_1}{\partial t} &= -e\left(n_0\frac{\partial\mathbf{v}_1}{\partial t} + \frac{\partial n_1}{\partial t}\mathbf{v}_0\right) \\
 \frac{\partial\mathbf{v}_1}{\partial t} &= -\frac{e}{m_e}(\mathbf{E}_1 + \mathbf{v}_1 \times \mathbf{B}_0 + \mathbf{v}_0 \times \mathbf{B}_1) - (\mathbf{v}_1 \cdot \nabla)\mathbf{v}_0 - (\mathbf{v}_0 \cdot \nabla)\mathbf{v}_1
 \end{aligned} \tag{1}$$

By assuming that the background current density is slowly varying on the length scale of the wave we can neglect the term  $(\mathbf{v}_1 \cdot \nabla)\mathbf{v}_0$  which provides a small simplification. The update equation for  $\mathbf{J}_1$  becomes:

$$\frac{\partial\mathbf{J}_1}{\partial t} = \frac{n_0e^2}{m_e}(\mathbf{E}_1 + \mathbf{v}_1 \times \mathbf{B}_0 + \mathbf{v}_0 \times \mathbf{B}_1) + en_0(\mathbf{v}_0 \cdot \nabla)\mathbf{v}_1 - e\mathbf{v}_0\frac{\partial n_1}{\partial t} \tag{2}$$

By applying a linear expansion to the continuity equation we arrive at the fol-

lowing:

$$-e \left( \frac{\partial n_0}{\partial t} + \frac{\partial n_1}{\partial t} \right) = \nabla \cdot \mathbf{J}_0 + \nabla \cdot \mathbf{J}_1 \quad (3)$$

where  $\nabla \cdot \mathbf{J}_0 = 0$  and  $\mathbf{J}_0$  does not change on the time scale of the wave and so the cancel to zero notation has been used. Using this equation one can substitute in for  $\mathbf{J}_1$ :

$$\frac{\partial n_1}{\partial t} = \nabla \cdot (n_0 \mathbf{v}_1 + n_1 \mathbf{v}_0) \quad (4)$$

The full expression is obtained using the vector calculus expression  $\nabla \cdot (\psi \mathbf{A}) = \psi(\nabla \cdot \mathbf{A}) + \mathbf{A} \cdot (\nabla \psi)$ .

$$\frac{\partial n_1}{\partial t} = n_0(\nabla \cdot \mathbf{v}_1) + \mathbf{v}_1 \cdot (\nabla n_0) + \cancel{n_1(\nabla \cdot \mathbf{v}_0)} + \mathbf{v}_0 \cdot (\nabla n_1) \quad (5)$$

where the cancel to zero notation has again been used for the previously stated assumption that the background current density and therefore  $\mathbf{v}_0$  is slowly varying on the length scale of the wave. By substituting in the equation for the change in perturbed density into the update equation for  $\mathbf{J}_1$  and collecting terms for  $\mathbf{J}_0$  one finds:

$$\frac{\partial \mathbf{J}_1}{\partial t} = \frac{n_0 e^2}{m_e} (\mathbf{E}_1 + \mathbf{v}_1 \times \mathbf{B}_0 + \mathbf{v}_0 \times \mathbf{B}_1) - (\mathbf{J}_0 \cdot \nabla) \mathbf{v}_1 + \mathbf{J}_0 (\nabla \cdot \mathbf{v}_1) - e n_0 \mathbf{v}_1 \cdot (\nabla n_0) + \mathbf{J}_0 \cdot (\nabla n_1) \quad (6)$$

It is noted that we can substitute in for  $\nabla \times (\mathbf{J}_0 \times \mathbf{v}_1) = -(\mathbf{J}_0 \cdot \nabla) \mathbf{v}_1 + \mathbf{J}_0 (\nabla \cdot \mathbf{v}_1)$

due to zero divergence of  $\mathbf{J}_0$  and the assumption it is slowly spatially varying.

$$\frac{\partial \mathbf{J}_1}{\partial t} = \frac{n_0 e^2}{m_e} (\mathbf{E}_1 + \mathbf{v}_1 \times \mathbf{B}_0 + \mathbf{v}_0 \times \mathbf{B}_1) + \nabla \times (\mathbf{J}_0 \times \mathbf{v}_1) - en_0 \mathbf{v}_1 \cdot (\nabla n_0) + \mathbf{J}_0 \cdot (\nabla n_1) \quad (7)$$



# Bibliography

- [1] Statistical Office of the European Union (Eurostat). Overview of the electricity production and use in europe. 2013.
- [2] International Energy Agency. Key world energy statistics. 2016.
- [3] Shahriar Shafiee and Erkan Topal. When will fossil fuel reserves be diminished? *Energy Policy*, 37(1):181 – 189, 2009.
- [4] S.H. Mohr, J. Wang, G. Ellem, J. Ward, and D. Giurco. Projection of world fossil fuels by country. *Fuel*, 141(Supplement C):120 – 135, 2015.
- [5] Iñigo Capellán-Pérez, Margarita Mediavilla, Carlos de Castro, Óscar Carpintero, and Luis Javier Miguel. Fossil fuel depletion and socio-economic scenarios: An integrated approach. *Energy*, 77(Supplement C):641 – 666, 2014.
- [6] Raquel A Silva, J Jason West, Yuqiang Zhang, Susan C Anenberg, Jean-François Lamarque, Drew T Shindell, William J Collins, Stig Dalsoren, Greg Faluvegi, Gerd Folberth, Larry W Horowitz, Tatsuya Nagashima, Vaishali Naik, Steven Rumbold, Ragnhild Skeie, Kengo Sudo, Toshihiko Takemura, Daniel Bergmann, Philip Cameron-Smith, Irene Cionni, Ruth M Doherty, Veronika Eyring, Beatrice Josse, I A MacKenzie, David Plummer, Mattia Righi, David S Stevenson, Sarah Strode, Sophie Szopa, and Guang Zeng. Global premature mortality due to anthropogenic outdoor air pollution and the contribution of past climate change. *Environmental Research Letters*, 8(3):034005, 2013.
- [7] Jos Lelieveld, JS Evans, M Fnais, Despina Giannadaki, and A Pozzer. The contribution of outdoor air pollution sources to premature mortality on a global scale. *Nature*, 525(7569):367–371, 2015.

- [8] Rasmus E Benestad, Dana Nuccitelli, Stephan Lewandowsky, Katharine Hayhoe, Hans Olav Hygen, Rob van Dorland, and John Cook. Learning from mistakes in climate research. *Theoretical and Applied Climatology*, 126(3-4):699–703, 2016.
- [9] European Commission. Climate change. 2015.
- [10] Ove Hoegh-Guldberg. Climate change, coral bleaching and the future of the world’s coral reefs. *Marine and Freshwater Research*, 50(8):839–866, 1999.
- [11] Andrew C Baker, Peter W Glynn, and Bernhard Riegl. Climate change and coral reef bleaching: An ecological assessment of long-term impacts, recovery trends and future outlook. *Estuarine, coastal and shelf science*, 80(4):435–471, 2008.
- [12] T. P. Hughes, A. H. Baird, D. R. Bellwood, M. Card, S. R. Connolly, C. Folke, R. Grosberg, O. Hoegh-Guldberg, J. B. C. Jackson, J. Kleypas, J. M. Lough, P. Marshall, M. Nyström, S. R. Palumbi, J. M. Pandolfi, B. Rosen, and J. Roughgarden. Climate change, human impacts, and the resilience of coral reefs. *Science*, 301(5635):929–933, 2003.
- [13] Wolfram Schlenker and Michael J Roberts. Nonlinear temperature effects indicate severe damages to us crop yields under climate change. *Proceedings of the National Academy of sciences*, 106(37):15594–15598, 2009.
- [14] Stefan Rahmstorf. A semi-empirical approach to projecting future sea-level rise. *Science*, 315(5810):368–370, 2007.
- [15] James Hansen, Makiko Sato, Pushker Kharecha, Karina Von Schuckmann, David J Beerling, Junji Cao, Shaun Marcott, Valerie Masson-Delmotte, Michael J Prather, Eelco J Rohling, et al. Young people’s burden: Requirement of negative co2 emissions. *arXiv preprint arXiv:1609.05878*, 2016.
- [16] RDE Atkinson and FG Houtermans. Transmutation of the lighter elements in stars. *Nature*, 123(3102):567–568, 1929.
- [17] ML Oliphant, ES Shire, and BM Crowther. Disintegration of the separated isotopes of lithium by protons and by heavy hydrogen’. *Nature*, 133:377, 1934.

- [18] YKM Peng. Spherical torus, compact fusion at low field. Technical report, Oak Ridge National Lab., TN (USA), 1985.
- [19] W Dorland, F Jenko, M Kotschenreuther, and BN Rogers. Electron temperature gradient turbulence. *Physical Review Letters*, 85(26):5579, 2000.
- [20] N Joiner, D Applegate, S C Cowley, W Dorland, and C M Roach. Electron temperature gradient driven transport in a mast h-mode plasma. *Plasma Physics and Controlled Fusion*, 48(5):685, 2006.
- [21] CC Hegna and JD Callen. On the stabilization of neoclassical magnetohydrodynamic tearing modes using localized current drive or heating. *Physics of Plasmas*, 4(8):2940–2946, 1997.
- [22] RJ Buttery, S Günter, G Giruzzi, TC Hender, D Howell, G Huysmans, RJ La Haye, M Maraschek, H Reimerdes, O Sauter, et al. Neoclassical tearing modes. *Plasma Physics and Controlled Fusion*, 42(12B):B61, 2000.
- [23] H Van Den Brand, MR de Baar, NJ Lopes Cardozo, and E Westerhof. Integrated modelling of island growth, stabilization and mode locking: consequences for NTM control on ITER. *Plasma Physics and Controlled Fusion*, 54(9):094003, 2012.
- [24] H Zohm, R Heidinger, M Henderson, E Poli, G Ramponi, G Saibene, and AGA Verhoeven. Comparison of the performance of different options for the ITER ECRH Upper Launcher. In *Journal of Physics: Conference Series*, volume 25, page 234. IOP Publishing, 2005.
- [25] F Clairet, C Bottereau, JM Chareau, M Paume, and R Sabot. Edge density profile measurements by X-mode reflectometry on Tore Supra. *Plasma physics and controlled fusion*, 43(4):429, 2001.
- [26] KW Kim, EJ Doyle, TL Rhodes, WA Peebles, CL Rettig, and NC Luhmann, Jr. Development of a fast solid-state high-resolution density profile reflectometer system on the DIII-D tokamak. *Review of scientific instruments*, 68(1):466–469, 1997.

- [27] SB Zhang, Xiang Gao, BL Ling, YM Wang, Tao Zhang, Xiang Han, Zixi Liu, Jingliang Bu, Jiangang Li, et al. Density profile and fluctuation measurements by microwave reflectometry on EAST. *Plasma Science and Technology*, 16(4):311–315, 2014.
- [28] DE Aguiam, A Silva, V Bobkov, PJ Carvalho, PF Carvalho, R Cavazzana, GD Conway, O D’Arcangelo, L Fattorini, H Faugel, et al. Implementation of the new multichannel X-mode edge density profile reflectometer for the ICRF antenna on ASDEX Upgrade. *Review of Scientific Instruments*, 87(11):11E722, 2016.
- [29] A Silva, L Cupido, M Manso, F Serra, I Nunes, J Santos, P Varela, S Vergamota, L Meneses, V Grossman, et al. Microwave reflectometry diagnostic for density profile and fluctuation measurements on ASDEX Upgrade. *Review of scientific instruments*, 70(1):1072–1075, 1999.
- [30] W Lee, J Leem, JA Lee, YB Nam, M Kim, GS Yun, Hyeon Keo Park, YG Kim, H Park, KW Kim, et al. Microwave imaging reflectometry for density fluctuation measurement on KSTAR. *Nuclear Fusion*, 54(2):023012, 2014.
- [31] E Mazzucato, T Munsat, H Park, BH Deng, CW Domier, NC Luhmann Jr, AJH Donné, and MJ van de Pol. Fluctuation measurements in tokamaks with microwave imaging reflectometry. *Physics of Plasmas*, 9(5):1955–1961, 2002.
- [32] J Schirmer, GD Conway, E Holzhauser, W Suttrop, H Zohm, et al. Radial correlation length measurements on ASDEX upgrade using correlation Doppler reflectometry. *Plasma Physics and Controlled Fusion*, 49(7):1019, 2007.
- [33] C Laviron, A J H Donné, M E Manso, and J Sanchez. Reflectometry techniques for density profile measurements on fusion plasmas. *Plasma Physics and Controlled Fusion*, 38(7):905, 1996.
- [34] E Mazzucato. Microwave reflectometry for magnetically confined plasmas. *Review of Scientific Instruments*, 69(6):2201–2217, 1998.

- [35] M Hirsch, E Holzhauer, J Baldzuhn, B Kurzan, and B Scott. Doppler reflectometry for the investigation of propagating density perturbations. *Plasma physics and controlled fusion*, 43(12):1641, 2001.
- [36] K. Hanada, H. Zushi, H. Idei, K. Nakamura, M. Ishiguro, S. Tashima, E. I. Kalinikova, M. Sakamoto, M. Hasegawa, A. Fujisawa, A. Higashijima, S. Kawasaki, H. Nakashima, H. Liu, O. Mitarai, T. Maekawa, A. Fukuyama, Y. Takase, and J. Qian. Non-inductive start up of QUEST plasma by RF power. *Plasma Science and Technology*, 13(3):307, 2011.
- [37] R. Raman, T.R. Jarboe, D. Mueller, M.J. Schaffer, R. Maqueda, B.A. Nelson, S.A. Sabbagh, M.G. Bell, R. Ewig, E.D. Fredrickson, D.A. Gates, J.C. Hosea, S.C. Jardin, H. Ji, R. Kaita, S.M. Kaye, H.W. Kugel, L.L. Lao, R. Maingi, J. Menard, M. Ono, D. Orvis, F. Paoletti, S.F. Paul, Y.-K.M. Peng, C.H. Skinner, J.B. Wilgen, S.J. Zweben, and NSTX Research Team. Non-inductive current generation in NSTX using coaxial helicity injection. *Nuclear Fusion*, 41(8):1081, 2001.
- [38] A. Ejiri, Y. Takase, T. Oosako, T. Yamaguchi, Y. Adachi, O. Watanabe, Y. Nagashima, B.I. An, H. Kobayashi, H. Kurashina, H. Hayashi, H. Matsuzawa, K. Yamada, H. Tojo, T. Masuda, M. Sasaki, R. Kumazawa, H. Kasahara, and F. Shimpo. Non-inductive plasma current start-up by EC and RF power in the TST-2 spherical tokamak. *Nuclear Fusion*, 49(6):065010, 2009.
- [39] V.F. Shevchenko, M.R. O'Brien, D. Taylor, A.N. Saveliev, and MAST team. Electron Bernstein wave assisted plasma current start-up in MAST. *Nuclear Fusion*, 50(2):022004, 2010.
- [40] du Toit, E.J., O'Brien, M.R., and Vann, R.G.L. A kinetic study of microwave start-up of tokamak plasmas. *EPJ Web Conf.*, 147:01002, 2017.
- [41] V Erckmann and U Gasparino. Electron cyclotron resonance heating and current drive in toroidal fusion plasmas. *Plasma Physics and Controlled Fusion*, 36(12):1869, 1994.

- [42] C. D. Warrick, R. J. Buttery, G. Cunningham, S. J. Fielding, T. C. Hender, B. Lloyd, A. W. Morris, M. R. O'Brien, T. Pinfeld, K. Stammers, M. Valovic, M. Walsh, H. R. Wilson, COMPASS-D, and RF teams. Complete stabilization of neoclassical tearing modes with lower hybrid current drive on COMPASS-D. *Phys. Rev. Lett.*, 85:574–577, Jul 2000.
- [43] A Becoulet. Heating and current drive regimes in the ion cyclotron range of frequency. *Plasma Physics and Controlled Fusion*, 38(12A):A1, 1996.
- [44] G Gantenbein, H Zohm, G Giruzzi, S Günter, F Leuterer, M Maraschek, J Meskat, Q Yu, ASDEX Upgrade Team, et al. Complete suppression of neoclassical tearing modes with current drive at the electron-cyclotron-resonance frequency in ASDEX Upgrade tokamak. *Physical Review Letters*, 85(6):1242, 2000.
- [45] H. Zohm, G. Gantenbein, F. Leuterer, A. Manini, M. Maraschek, Q. Yu, and the ASDEX Upgrade Team. Control of MHD instabilities by ECCD: ASDEX Upgrade results and implications for ITER. *Nuclear Fusion*, 47(3):228, 2007.
- [46] CC Petty, RJ La Haye, TC Luce, DA Humphreys, AW Hyatt, J Lohr, R Prater, EJ Strait, and MR Wade. Complete suppression of the  $m=2/n=1$  neoclassical tearing mode using electron cyclotron current drive in DIII-D. *Nuclear Fusion*, 44(2):243, 2004.
- [47] RJ La Haye, S Günter, DA Humphreys, J Lohr, TC Luce, ME Maraschek, CC Petty, R Prater, JT Scoville, and EJ Strait. Control of neoclassical tearing modes in DIII-D. *Physics of Plasmas*, 9(5):2051–2060, 2002.
- [48] A Isayama, Y Kamada, N Hayashi, T Suzuki, T Oikawa, T Fujita, T Fukuda, S Ide, H Takenaga, K Ushigusa, et al. Achievement of high fusion triple product, steady-state sustainment and real-time NTM stabilization in high- $\beta_p$  ELMy H-mode discharges in JT-60U. *Nuclear Fusion*, 43(10):1272, 2003.

- [49] DA Humphreys, JR Ferron, RJ La Haye, TC Luce, CC Petty, R Prater, and AS Welander. Active control for stabilization of neoclassical tearing modes. *Physics of Plasmas*, 13(5):056113, 2006.
- [50] SJ Freethy. *Synthetic aperture imaging of B-X-O mode conversion*. PhD thesis, 2012.
- [51] V F Shevchenko, R G L Vann, S J Freethy, and B K Huang. Synthetic aperture microwave imaging with active probing for fusion plasma diagnostics. *Journal of Instrumentation*, 7(10):P10016, 2012.
- [52] Roderick GL Vann, KJ Brunner, R Ellis, Gary Taylor, and David Allden Thomas. Preliminary measurements of the edge magnetic field pitch from 2-D Doppler backscattering in MAST and NSTX-U. *Review of Scientific Instruments*, 87(11):11D902, 2016.
- [53] S. J. Zweben, J. A. Boedo, O. Grulke, C. Hidalgo, B. LaBombard, R. J. Maqueda, P. Scarin, and J. L. Terry. Edge turbulence measurements in toroidal fusion devices. *Plasma Physics and Controlled Fusion*, 49(7):S1, 2007.
- [54] C. M. Surko and R. E. Slusher. Waves and turbulence in a tokamak fusion plasma. *Science*, 221(4613):817–822, 1983.
- [55] M Hirsch and E Holzhauser. Doppler reflectometry with optimized temporal resolution for the measurement of turbulence and its propagation velocity. *Plasma physics and controlled fusion*, 46(4):593, 2004.
- [56] G D Conway, J Schirmer, S Klenge, W Suttrop, E Holzhauser, and the ASDEX Upgrade Team. Plasma rotation profile measurements using Doppler reflectometry. *Plasma Physics and Controlled Fusion*, 46(6):951, 2004.
- [57] P Hennequin, C Honoré, A Truc, A Quéméneur, C Fenzi-Bonizec, C Bourdelle, X Garbet, GT Hoang, et al. Fluctuation spectra and velocity profile from Doppler backscattering on Tore Supra. *Nuclear fusion*, 46(9):S771, 2006.

- [58] T Estrada, T Happel, L Eliseev, D López-Bruna, E Ascasíbar, E Blanco, L Cupido, JM Fontdecaba, C Hidalgo, R Jiménez-Gómez, et al. Sheared flows and transition to improved confinement regime in the TJ-II stellarator. *Plasma Physics and Controlled Fusion*, 51(12):124015, 2009.
- [59] JC Hillesheim, E Delabie, H Meyer, CF Maggi, L Meneses, E Poli, JET Contributors, EUROfusion Consortium, et al. Stationary zonal flows during the formation of the edge transport barrier in the JET tokamak. *Physical review letters*, 116(6):065002, 2016.
- [60] G D Conway, B Scott, J Schirmer, M Reich, A Kendl, and the ASDEX Upgrade Team. Direct measurement of zonal flows and geodesic acoustic mode oscillations in ASDEX Upgrade using doppler reflectometry. *Plasma Physics and Controlled Fusion*, 47(8):1165, 2005.
- [61] DA Thomas, KJ Brunner, SJ Freethy, BK Huang, VF Shevchenko, and RGL Vann. 2D Doppler backscattering using synthetic aperture microwave imaging of MAST edge plasmas. *Nuclear fusion*, 56(2):026013, 2016.
- [62] GD Conway, C Angioni, F Ryter, P Sauter, J Vicente, and ASDEX Upgrade Team. Mean and oscillating plasma flows and turbulence interactions across the l-H confinement transition. *Physical review letters*, 106, 2011.
- [63] J W Connor. Edge-localized modes - physics and theory. *Plasma Physics and Controlled Fusion*, 40:531–542, 1998.
- [64] Janardhan Manickam. The role of edge current density on kink mode stability and its implication for magnetohydrodynamic activity associated with edge localized modes. *Physics of Fluids B: Plasma Physics*, 4(7):1901–1908, 1992.
- [65] PB Snyder, HR Wilson, JR Ferron, LL Lao, AW Leonard, TH Osborne, AD Turnbull, D Mossessian, M Murakami, and XQ Xu. Edge localized modes and the pedestal: A model based on coupled peeling-ballooning modes. *Physics of Plasmas*, 9(5):2037–2043, 2002.

- [66] HR Wilson, SC Cowley, A Kirk, and PB Snyder. Plasma phys. control. fusion 48. A71, 2006.
- [67] Dennis H Goldstein. *Polarized light*. CRC press, 2016.
- [68] F Ayres. Theory and problems of matrices, ser. schaum's outline series in mathematics, 1962.
- [69] Thomas H Stix. *Waves in plasmas*. Springer Science & Business Media, 1992.
- [70] R. Fitzpatrick. *The Physics of Plasmas*. Lulu, 2008.
- [71] FR Hansen, Jens-Peter Lynov, C Maroli, and V Petrillo. Full-wave calculations of the ox mode conversion process. *Journal of plasma physics*, 39(2):319–337, 1988.
- [72] E Mjølhus. Linear conversion in a magnetized plasma with density gradient parallel to the magnetic field. *Journal of plasma physics*, 30(2):179–192, 1983.
- [73] R Prater, D Farina, Yu Gribov, RW Harvey, AK Ram, Y-R Lin-Liu, E Poli, AP Smirnov, F Volpe, E Westerhof, et al. Benchmarking of codes for electron cyclotron heating and electron cyclotron current drive under ITER conditions. *Nuclear Fusion*, 48(3):035006, 2008.
- [74] Christos Tsironis, Arthur G Peeters, Heinz Isliker, Dafni Strintzi, Ioanna Chatziantonaki, and Loukas Vlahos. Electron-cyclotron wave scattering by edge density fluctuations in ITER. *Physics of Plasmas*, 16(11):112510, 2009.
- [75] N Bertelli, AA Balakin, E Westerhof, and MN Buyanova. ECCD calculations in iter by means of the quasi-optical code. *Nuclear Fusion*, 50(11):115008, 2010.
- [76] EV Sysoeva, F da Silva, EZ Gusakov, Stéphane Heuraux, and A Yu Popov. Electron cyclotron resonance heating beam broadening in the edge turbulent plasma of fusion machines. *Nuclear Fusion*, 55(3):033016, 2015.
- [77] Yves Peysson, Joan Decker, Lorenzo Morini, and S Coda. RF current drive and plasma fluctuations. *Plasma Physics and Controlled Fusion*, 53(12):124028, 2011.

- [78] Y Peysson, Joan Decker, and Lorenzo Morini. A versatile ray-tracing code for studying RF wave propagation in toroidal magnetized plasmas. *Plasma Physics and Controlled Fusion*, 54(4):045003, 2012.
- [79] TRN Williams. Full-wave simulation of high-frequency electromagnetic propagation through inhomogeneous plasma. *Ph.D. Thesis, University of York*, 2014.
- [80] Kane Yee. Numerical solution of initial boundary value problems involving Maxwell's equations in isotropic media. *IEEE Transactions on antennas and propagation*, 14(3):302–307, 1966.
- [81] Allen Taflove and Susan C Hagness. *Computational electrodynamics: the finite-difference time-domain method*. Artech house, 2005.
- [82] Esler. KP. *Einspline B-spline library version 0.9.2*, 2013.
- [83] A. Hewish. The diffraction of radio waves in passing through a phase-changing ionosphere. *Proceedings of the Royal Society of London A: Mathematical, Physical and Engineering Sciences*, 209(1096):81–96, 1951.
- [84] W. Horton. Nonlinear drift waves and transport in magnetized plasma. *Physics Reports*, 192(1):1 – 177, 1990.
- [85] a. J. Wootton, B. a. Carreras, H. Matsumoto, K. McGuire, W. a. Peebles, Ch. P. Ritz, P. W. Terry, and S. J. Zweben. Fluctuations and anomalous transport in tokamaks. *Physics of Fluids B: Plasma Physics*, 2(1990):2879, 1990.
- [86] B. D. Dudson, M. V. Umansky, X. Q. Xu, P. B. Snyder, and H. R. Wilson. BOUT++: A framework for parallel plasma fluid simulations. *Computer Physics Communications*, 180(9):1467–1480, September 2009.
- [87] J. Leddy, A. Koehn, M. B. Thomas, and R. G. L. Vann. Plasma density turbulence obtained from a Hasegawa-Wakatani drift-wave turbulence model within the BOUT++ framework, 2016.
- [88] Masahiro Wakatani and Akira Hasegawa. A collisional drift wave description of plasma edge turbulence. *Physics of Fluids*, 27(3):611, 1984.

- [89] B. D. Scott, H. Biglari, P. W. Terry, and P. H. Diamond. Self organization in sheared drift wave turbulence. *Physics of Fluids B: Plasma Physics*, 3(1):51–67, 1991.
- [90] A. E. Koniges, J. A. Crotinger, and P. H. Diamond. Structure formation and transport in dissipative drift wave turbulence. *Physics of Fluids B: Plasma Physics*, 4(9):2785–2793, 1992.
- [91] S. J. Camargo, D. Biskamp, and B. D. Scott. Resistive drift-wave turbulence 85748. *Physics of Plasmas*, 2(1):48–62, 1995.
- [92] D E Evans, M von Hellermann, and E Holzhauer. Fourier optics approach to far forward scattering and related refractive index phenomena in laboratory plasmas. *Plasma Physics*, 24(7):819, 1982.
- [93] Heinrich Peter Laqua. Electron Bernstein wave heating and diagnostic. *Plasma Physics and Controlled Fusion*, 49(4):R1, 2007.
- [94] B D Dudson, N Ben Ayed, A Kirk, H R Wilson, G Counsell, X Xu, M Umansky, P B Snyder, B Lloyd, and the MAST team. Experiments and simulation of edge turbulence and filaments in MAST. *Plasma Physics and Controlled Fusion*, 50(12):124012, 2008.
- [95] N Ben Ayed, A Kirk, B Dudson, S Tallents, R G L Vann, H R Wilson, and the MAST team. Inter-ELM filaments and turbulent transport in the Mega-Amp Spherical Tokamak. *Plasma Physics and Controlled Fusion*, 51(3):035016, 2009.
- [96] G Fuchert, G Birkenmeier, D Carralero, T Lunt, P Manz, H W Müller, B Nold, M Ramisch, V Rohde, and U Stroth. Blob properties in L- and H-mode from gas-puff imaging in ASDEX upgrade. *Plasma Physics and Controlled Fusion*, 56(12):125001, 2014.
- [97] J Stober, O Gruber, A Kallenbach, V Mertens, F Ryter, A Stäbler, W Sutrop, W Treutterer, and the ASDEX Upgrade Team. Effects of triangularity on confinement, density limit and profile stiffness of H-modes on ASDEX upgrade. *Plasma Physics and Controlled Fusion*, 42(5A):A211, 2000.

- [98] MA Henderson, R Heidinger, D Strauss, R Bertizzolo, A Bruschi, R Chavan, E Ciattaglia, S Cirant, A Collazos, I Danilov, et al. Overview of the ITER EC upper launcher. *Nuclear fusion*, 48(5):054013, 2008.
- [99] KK Kirov, F Leuterer, GV Pereverzev, F Rytter, W Suttrop, et al. ECRH power deposition studies in ASDEX Upgrade. *Plasma physics and controlled fusion*, 44(12):2583, 2002.
- [100] CC Petty, R Prater, J Lohr, TC Luce, WR Fox, RW Harvey, JE Kinsey, LL Lao, and MA Makowski. Detailed measurements of the electron cyclotron current drive efficiency on DIII-D. *Nuclear fusion*, 42(12):1366, 2002.
- [101] Brookman, M. W., Austin, M. E., Gentle, K. W., Petty, C. C., Ernst, D. E., Peysson, Y., Decker, J., and Barada, K. Experimental measurement of ech deposition broadening: Beyond anomalous transport. *EPJ Web Conf.*, 147:03001, 2017.
- [102] MW Brookman, MB Thomas, ME Austin, K Barada, M Cenghar, RJ La Haye, JB Leddy, TC Luce, CC Petty, T rhodes, and RGL Vann. Resolving broadening of ECRH deposition due to edge turbulence in DIII-D by the heat flux measurements. *Submitted to Nuclear fusion*, 2017.
- [103] J Decker, Y Peysson, and S Coda. Effect of density fluctuations on eccd in iter and tcv. In *EPJ Web of Conferences*, volume 32, page 01016. EDP Sciences, 2012.
- [104] RJ La Haye, J Lohr, TC Luce, CC Petty, R Prater, EJ Strait, DP Brennan, JR Ferron, DA Humphreys, LL Lao, and ML Walker. Suppression of neoclassical tearing modes in the presence of sawteeth instabilities by radially localized off-axis electron cyclotron current drive in the DIII-D tokamak. *EPS Conference Proceedings*, 25A:1357–1360, 2001.
- [105] E Poli, C Angioni, FJ Casson, D Farina, L Figini, TP Goodman, O Maj, O Sauter, H Weber, H Zohm, et al. On recent results in the modelling of neoclassical-tearing-mode stabilization via electron cyclotron current drive and

- their impact on the design of the upper ec launcher for iter. *Nuclear Fusion*, 55(1):013023, 2015.
- [106] N Bertelli and E Westerhof. Consequences of finite transport on the effectiveness of ECCD for neoclassical tearing mode stabilization in ITER. *Nuclear Fusion*, 49(9):095018, 2009.
- [107] P Nikkola, O Sauter, R Behn, S Coda, I Condrea, TP Goodman, MA Henderson, RW Harvey, et al. Modelling of the electron cyclotron current drive experiments in the TCV tokamak. *Nuclear fusion*, 43(11):1343, 2003.
- [108] J Decker, Yves Peysson, J-F Artaud, V Basiuk, Stefano Coda, A Ekedahl, Silvano Gnesin, M Goniche, D Mazon, and PK Sharma. Bremsstrahlung emission modelling and application to fast electron physics. In *AIP Conference Proceedings*, volume 1406, pages 447–450. AIP, 2011.
- [109] AG Peeters, Y Camenen, F James Casson, WA Hornsby, AP Snodin, D Strintzi, and Gabor Szepesi. The nonlinear gyro-kinetic flux tube code GKW. *Computer Physics Communications*, 180(12):2650–2672, 2009.
- [110] FJ Casson, E Poli, C Angioni, R Buchholz, and AG Peeters. Effect of turbulence on electron cyclotron current drive and heating in ITER. *Nuclear Fusion*, 55(1):012002, 2015.
- [111] Alf Köhn, Eberhard Holzhauser, Jarrod Leddy, Matthew B Thomas, and Roddy GL Vann. Influence of plasma turbulence on microwave propagation. *Plasma Physics and Controlled Fusion*, 58(10):105008, 2016.
- [112] Benjamin Daniel Dudson and Jarrod Leddy. Hermes: Global plasma edge fluid turbulence simulations. *Plasma Physics and Controlled Fusion*, 59(5):054010, 2017.
- [113] P.C. Strangeby. *The Plasma Boundary of Magnetic Fusion Devices*. CRC Press, 2000.

- [114] TN Carlstrom, GL Campbell, JC DeBoo, R Evanko, J Evans, CM Greenfield, J Haskovec, CL Hsieh, E McKee, RT Snider, et al. Design and operation of the multipulse Thomson scattering diagnostic on DIII-D. *Review of scientific instruments*, 63(10):4901–4906, 1992.
- [115] GR McKee, RJ Fonck, DK Gupta, DJ Schlossberg, MW Shafer, C Holland, and G Tynan. *Rev. sci. instrum.* 1999.
- [116] P Devynck, G Bonhomme, E Martines, J Stöckel, G Van Oost, I Voitsekhovitch, J Adámek, A Azeroual, F Doveil, I Duran, et al. Spatially resolved characterization of electrostatic fluctuations in the scrape-off layer of the CASTOR tokamak. *Plasma physics and controlled fusion*, 47(2):269, 2005.
- [117] O Grulke, JL Terry, B LaBombard, and SJ Zweben. Radially propagating fluctuation structures in the scrape-off layer of Alcator C-Mod. *Physics of Plasmas*, 13(1):012306, 2006.
- [118] M Jakubowski, RJ Fonck, and GR McKee. Observation of coherent sheared turbulence flows in the DIII-D tokamak. *Physical review letters*, 89(26):265003, 2002.
- [119] GR McKee, CC Petty, RE Waltz, C Fenzi, RJ Fonck, JE Kinsey, TC Luce, KH Burrell, DR Baker, EJ Doyle, et al. Non-dimensional scaling of turbulence characteristics and turbulent diffusivity. *Nuclear Fusion*, 41(9):1235, 2001.
- [120] George R McKEE, Raymond J Fonck, Deepak K Gupta, David J Schlossberg, Morgan W Shafer, Réjean L Boivin, and Wayne Solomon. Plasma turbulence imaging via beam emission spectroscopy in the core of the DIII-D tokamak. *Plasma and Fusion Research*, 2:S1025–S1025, 2007.
- [121] Morgan W Shafer, RJ Fonck, GR McKee, Chris Holland, AE White, and DJ Schlossberg. 2D properties of core turbulence on DIII-D and comparison to gyrokinetic simulations. *Physics of Plasmas*, 19(3):032504, 2012.
- [122] Alessandro Marinoni, Stephan Brunner, Yann Camenen, Stefano Coda, JP Graves, Xavier Lapillonne, Antoine Pochelon, Olivier Sauter, and Laurent Vil-

- lard. The effect of plasma triangularity on turbulent transport: modeling TCV experiments by linear and non-linear gyrokinetic simulations. *Plasma Physics and Controlled Fusion*, 51(5):055016, 2009.
- [123] BI Cohen, MV Umansky, WM Nevins, MA Makowski, JA Boedo, DL Rudakov, GR McKee, Z Yan, and RJ Groebner. Simulations of drift resistive ballooning l-mode turbulence in the edge plasma of the DIII-D tokamak. *Physics of Plasmas*, 20(5):055906, 2013.
- [124] Köhn, Alf, Holzhauser, Eberhard, Leddy, Jarrod, Thomas, Matthew B., and Vann, Roddy G. L. Perturbing microwave beams by plasma density fluctuations. *EPJ Web Conf.*, 147:01001, 2017.
- [125] Qudsia Quraishi, Scott Robertson, and Bob Walch. Electron diffusion in the annular penning trap. *Physics of Plasmas*, 9(8):3264–3271, 2002.
- [126] C. L. Ellison, Y. Raitses, and N. J. Fisch. Cross-field electron transport induced by a rotating spoke in a cylindrical hall thruster. *Physics of Plasmas*, 19(1):013503, 2012.
- [127] M. Keidar and I. I. Beilis. Electron transport phenomena in plasma devices with  $E \times B$  drift. *IEEE Transactions on Plasma Science*, 34(3):804–814, June 2006.
- [128] P.J Kelly and R.D Arnell. Magnetron sputtering: a review of recent developments and applications. *Vacuum*, 56(3):159 – 172, 2000.
- [129] D. P. Moehs, J. Peters, and J. Sherman. Negative hydrogen ion sources for accelerators. *IEEE Transactions on Plasma Science*, 33(6):1786–1798, Dec 2005.
- [130] W. Kraus, M. Berger, U. Fantz, P. Franzen, M. Fröschle, B. Heinemann, R. Riedl, E. Speth, A. Stäbler, and D. Wunderlich. Long pulse H-beam extraction with a RF driven ion source with low fraction of co-extracted electrons. *AIP Conference Proceedings*, 1097(1):275–281, 2009.
- [131] P. Franzen, H.D. Falter, U. Fantz, W. Kraus, M. Berger, S. Christ-Koch, M. Fröschle, R. Gutser, B. Heinemann, S. Hilbert, S. Leyer, C. Martens, P. Mc-

- Neely, R. Riedl, E. Speth, and D. Wunderlich. Progress of the development of the IPP RF negative ion source for the ITER neutral beam system. *Nuclear Fusion*, 47(4):264, 2007.
- [132] R.S. Hemsworth. Long pulse neutral beam injection. *Nuclear Fusion*, 43(9):851, 2003.
- [133] U Fantz, L Schiesko, and D Wunderlich. Plasma expansion across a transverse magnetic field in a negative hydrogen ion source for fusion. *Plasma Sources Science and Technology*, 23(4):044002, 2014.
- [134] M Cavenago, P Veltri, V Antoni, and G Serianni. Multigrid negative ion source test and modeling. 2008.
- [135] Robert L Merlino. Understanding Langmuir probe current-voltage characteristics. *American Journal of Physics*, 75(12):1078–1085, 2007.
- [136] V. I. Demidov, S. V. Ratynskaia, and K. Rypdal. Electric probes for plasmas: The link between theory and instrument. *Review of Scientific Instruments*, 73(10):3409–3439, 2002.
- [137] H. J. van der Meiden, R. S. Al, C. J. Barth, A. J. H. Donné, R. Engeln, W. J. Goedheer, B. de Groot, A. W. Kleyn, W. R. Koppers, N. J. Lopes Cardozo, M. J. van de Pol, P. R. Prins, D. C. Schram, A. E. Shumack, P. H. M. Smeets, W. A. J. Vijvers, J. Westerhout, G. M. Wright, and G. J. van Rooij. High sensitivity imaging thomson scattering for low temperature plasma. *Review of Scientific Instruments*, 79(1):013505, 2008.
- [138] D Levko, L Garrigues, and G J M Hagelaar. Chemical composition of SF6 low-pressure plasma in magnetic field. *Journal of Physics D: Applied Physics*, 47(4):045205, 2014.
- [139] D. Levko, L. Garrigues, and G. J. M. Hagelaar. Transport of low pressure electronegative SF6 plasma through a localized magnetic filter. *Physics of Plasmas*, 21(8):083505, 2014.

- [140] S Dujko, Z M Raspopović, and Z Lj Petrović. Monte Carlo studies of electron transport in crossed electric and magnetic fields in CF 4. *Journal of Physics D: Applied Physics*, 38(16):2952, 2005.
- [141] S Dujko, R D White, K F Ness, Z Lj Petrović, and R E Robson. Non-conservative electron transport in CF 4 in electric and magnetic fields crossed at arbitrary angles. *Journal of Physics D: Applied Physics*, 39(22):4788, 2006.
- [142] St Kolev, G J M Hagelaar, G Fubiani, and J-P Boeuf. Physics of a magnetic barrier in low-temperature bounded plasmas: insight from particle-in-cell simulations. *Plasma Sources Science and Technology*, 21(2):025002, 2012.
- [143] R. Baude, F. Gaboriau, and G. J. M. Hagelaar. Wall current probe: A non-invasive in situ plasma diagnostic for space and time resolved current density distribution measurement. *Review of Scientific Instruments*, 84(8):083502, 2013.
- [144] F. Gaboriau, R. Baude, and G. J. M. Hagelaar. Experimental evidence of the increased transport due to the wall bounded magnetic drift in low temperature plasma. *Applied Physics Letters*, 104(21):214107, 2014.
- [145] D. Renaud, D. Gerst, S. Mazouffre, and A. Aanesland.  $E \times B$  probe measurements in molecular and electronegative plasmas. *Review of Scientific Instruments*, 86(12):123507, 2015.
- [146] A Aanesland, J Bredin, and P Chabert. A review on ion-ion plasmas created in weakly magnetized electronegative plasmas. *Plasma Sources Science and Technology*, 23(4):044003, 2014.
- [147] L Schiesko, P McNeely, P Franzen, U Fantz, and the NNBI Team. Magnetic field dependence of the plasma properties in a negative hydrogen ion source for fusion. *Plasma Physics and Controlled Fusion*, 54(10):105002, 2012.
- [148] T Lafleur, D Rafalskyi, and A Aanesland. Alternate extraction and acceleration of positive and negative ions from a gridded plasma source. *Plasma Sources Science and Technology*, 24(1):015005, 2015.

- [149] A Aanesland, A Meige, and P Chabert. Electric propulsion using ion-ion plasmas. *Journal of Physics: Conference Series*, 162(1):012009, 2009.
- [150] Jerome Bredin, Pascal Chabert, and Ane Aanesland. Langmuir probe analysis of highly electronegative plasmas. *Applied Physics Letters*, 102(15):154107, 2013.
- [151] A. Aanesland, D. Rafalskyi, J. Bredin, P. Grondein, N. Oudini, P. Chabert, D. Levko, L. Garrigues, and G. Hagelaar. The pegases gridded ion-ion thruster performance and predictions. *IEEE Transactions on Plasma Science*, 43(1):321–326, Jan 2015.
- [152] Jerome Bredin, Pascal Chabert, and Ane Aanesland. Langmuir probe analysis in electronegative plasmas. *Physics of Plasmas*, 21(12):123502, 2014.
- [153] Francis Chen. *Introduction to Plasma Physics and Controlled Fusion*, volume 1. 2nd edition, 1974.
- [154] T. Laffleur and A. Aanesland. Ambipolar and non-ambipolar diffusion in an RF plasma source containing a magnetic filter. *Physics of Plasmas*, 21(6):063510, 2014.
- [155] Comsol. *Multiphysics Reference Guide for COMSOL 4.2*, 2011.
- [156] Shinya Sasaki, Itsuo Ishikawa, Kazuy Nagaseki, Yukinori Saito, and Shinji Suganomata. Positive and negative ions in RF plasmas of SF<sub>6</sub>/N<sub>2</sub> and SF<sub>6</sub>/ar mixtures in a planar diode. *Japanese Journal of Applied Physics*, 36(2R):847, 1997.
- [157] Kazunori Koga, Hiroshi Naitou, and Yoshinobu Kawai. Characteristics of asymmetric ion sheath in a negative ion plasma. *Frontiers in Dusty Plasmas*, 1, 2000.